

Novel Anode Materials For Solid Oxide Fuel Cells

Dissertation committee

Promotor:

Prof. dr. ir. D.N. Reinhoudt, University of Twente

Co-promotor:

Prof. dr. J. Schoonman, TU Delft

Members:

Prof. dr. ir. J.H.A. de Smit, University of Twente

Dr. B.A. Boukamp, University of Twente

Dr. H.J.M. Bouwmeester, University of Twente

Dr. F. Tietz, Forschungszentrum Jülich, Germany

Prof. dr. P.H.L. Notten, Philips Research Laboratories Eindhoven

Prof. dr. ir. B. Poelsema, University of Twente

Prof. dr. ing. M. Mulder, University of Twente

Part of the investigations described in this thesis were financially supported by the European Commission in the framework of the TMR network programme “Synthesis, preparation and fabrication of alternative anodes for direct methane oxidation in SOFC”.



Twente University **Press**

Publisher:

Twente University Press, P.O. Box 217, 7500 AE Enschede, the Netherlands,
www.tup.utwente.nl

Cover design: Jo Molenaar, [deel 4] ontwerpers, Enschede

Print: Océ Facility Services, Enschede

© M.M. González Cuenca, Enschede, 2002

No part of this work may be reproduced by print, photocopy or any other means without the permission in writing from the publisher.

ISBN 9036517907

NOVEL ANODE MATERIALS
FOR SOLID OXIDE FUEL CELLS

DISSERTATION

to obtain
the doctor's degree at the University of Twente,
on the authority of the rector magnificus,
prof. dr. F.A. van Vught,
on account of the decision of the graduation committee,
to be publicly defended
on Friday 30 August 2002 at 13.15

by

María Mercedes González Cuenca

born on 24 February 1972
in Santander, Spain

This dissertation has been approved by the promotor

prof. dr. ir. D.N. Reinhoudt

prof. dr. J. Schoonman

and assistant promotor

dr. B.A. Boukamp

A mis padres

Table of contents

Chapter 1	Introduction to fuel cells	5
Chapter 2	The effect of the presence of fine YSZ particles on the performance of porous nickel electrodes	21
Chapter 3	Mechanistic modelling of the H ₂ oxidation reaction on Ni/YSZ anodes	35
Chapter 4	Chromite-titanate perovskites for application as anodes in solid oxide fuel cells	51
Chapter 5	Hydrogen oxidation on Ni/Y ₂ O ₃ -ZrO ₂ -TiO ₂ cermet anodes	75
Appendix A	Percolation and conduction in disordered media	99
Appendix B	Modelling constant voltage electrophoretic deposition from a stirred suspension	125
	Summary/Samenvatting	141
	Acknowledgement	149
	Curriculum vitae	151

1

Introduction to Fuel Cells

In this chapter a general introduction is given on fuel cells, especially solid oxide fuel cells (SOFC). The principles and materials employed for SOFC are described. Emphasis is on the anode, particularly its chemistry, research and developmental aspects. At the end of the chapter the scope of this thesis is presented.

1.1 The fuel cell

1.1.1 Introduction

Production and distribution of energy affects all sectors of the global economy. The increasing industrialisation of the world requires sustainable, highly efficient energy production. Without a major technology advance, energy production will impact the quality of life on earth. For this reason, the application of the fuel cell technologies may be one of the most important technological advancement of the next decades.

A fuel cell operating as a sort of continuously replenished battery provides an alternative, whereby electrical energy can be made available with small losses. If the fuel is clean, the effluents are in principle only water, heat and CO₂. Fuel cell plants can be modular in design, and the energy production can be adjusted to meet the actual demand, which is a convenient feature for a power source in a technological society [1].

1.1.2 Definition of a fuel cell

A most general and simple definition of a fuel cell is: ‘an electrochemical device that directly converts chemical energy, from a reaction between a fuel and an oxidant, into electrical energy’. They offer a clean, pollution free technology to electrochemically generate electricity at high efficiencies. The basic elements of a typical fuel cell, as depicted in Figure 1.1, consist of an electrolyte in intimate contact with a porous anode (negative electrode) and a porous cathode (positive electrode). The fuel and oxidant gases flow along the surface of the anode and cathode, respectively, and they react electrochemically in the three-phase-boundary region established at the gas – electrolyte - electrode interface. A fuel cell can theoretically produce electrical energy for as long as fuel and oxidant are fed to the porous electrodes, but the degradation or malfunction of some of its components limits the practical life span of al fuel cell.

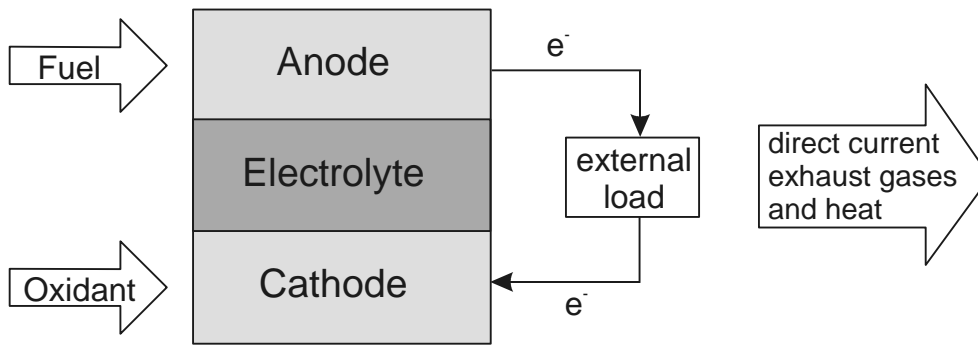


Figure 1.1: Schematic representation of a planar fuel cell.

Different fuels can be used, such as hydrogen, ethanol, methanol, or gaseous fossils fuels like natural gas. Solid or liquid fossil fuels need to be gasified first before they can be used as fuel. Oxygen or air can be used as oxidant [2].

1.1.3 History

The history of the fuel cell dates back to 1839 when Sir William Grove [3] first described its principle and demonstrated a fuel cell at room temperature using a liquid electrolyte. In 1899, Nernst discovered the solid oxide electrolyte when using stabilised zirconia in making filaments for electric glowers. In the middle of the 20th century the development accelerated. Several types of fuel cells were developed in the race for conquering the space. In the eighties focus on pollution and the demand for higher efficiency in the exploitation of fossil resources initiated a new wave of fuel cell developments. At present several types of fuel cells are approaching the consumer market within a limited number of years [1]. The primary challenges are cost and durability, to be solved by materials selection and design engineering [2].

1.1.4 Types of fuel cells

Today five types of fuel cells are commonly known, all named after the employed electrolyte material:

- the solid polymer proton conductor fuel cell (SPFC),
- the alkaline fuel cell (AFC),
- the phosphoric acid fuel cell (PAFC),
- the molten carbonate fuel cell (MCFC),
- the solid oxide fuel cell (SOFC).

Each type of fuel cell has certain characteristics, some of which are listed in Table 1.1. Among these are operation temperature, electric efficiency and demands for fuel composition defining the prospects of each type.

	AFC ^a	AFC ^b	SPFC	PAFC	MCFC	SOFC
Anode	80%Pt-20%Pd	Ni	Pt black or Pt/C	Pt/C	Ni-10%Cr	Ni-YSZ cermet
Cathode	90%Au-10%Pt	Li-doped NiO	Pt black or Pt/C	Pt/C	Li-doped NiO	Sr-doped LaMnO ₃
Electrolyte	35-45% KOH	85% KOH	Nafion ^c	H ₃ PO ₄	62%Li ₂ C O ₃ + 38% K ₂ CO ₃	Ytria-stabilised ZrO ₂
Fuel	Highly pure H ₂	Highly pure H ₂	Pure H ₂	CO-free H ₂	H ₂ , CH ₄ , CO	H ₂ , CH ₄ , CO
Charge Carrier	OH ⁻	OH ⁻	H ⁺	H ⁺	CO ₃ ²⁻	O ²⁻
Operation Temperature	80-90°C	260°C	80-260°C	200°C	650°C	800-100°C
Electrical Efficiency ^d	40%	40%	40%	40%	60%	60%

Table 1.1: The most important characteristics for six common types of fuel cells ^a space shuttle Orbiter, ^b Apollo program, ^c fluorinated sulfonic acid, registered trademark of E.I. Du Pont de Nemours & Company, Inc. [4], ^d compared with higher heating value for methane [1]

Low temperature fuel cells (AFC, SPFC and PAFC) have a potential for propulsion of cars, where a short heating time is needed and the efficiency has to be compared with that of a combustion engine (~20%) given by the limitations of the Carnot cycle. A type of SPFC, the so-called direct methanol fuel cells are relatively early in their development phase and they are being considered mainly for portable and automotive purposes. In miniature applications such as cellular phones, laptops and digital cameras, methanol is reformed to hydrogen in the fuel cell itself (reformation

reaction). For applications that require higher power output, such as cars, methanol can be reformed in a device that is located outside the fuel cell. This reformation can be accomplished through steam reforming or partial oxidation [5]. In late April 1999 R. Hockaday gave a presentation in Maryland U.S. about the progress of Manhattan Scientifics' patented Micro-Fuel CellTM technology in the field of portable electronic market, in particular cellular phones. Micro-fuel cells are smaller, lighter, cleaner, simpler and less expensive than lithium ion batteries [6].

The Industrial Technology Research Institute in Taiwan in collaboration with other organisations such as Du Pont U.S. and Case Western Reserve University in U.S. is currently developing a program in which they integrate nanotechnology to develop miniature fuel cells suitable to fit in small electronic equipment [7].

Daimler Chrysler AG plans to market a fuel cell-powered bus by the end of this year and some passenger cars by 2004. Ford Motor Co. also plans a 'limited built' of fuel cell vehicles by the same year. The Bush administration announced recently a new pact with the major automakers that focuses on accelerating the development of non-polluting vehicles powered by hydrogen fuel cells. The new program, called Freedom Cooperative Automotive Research, will also focus on developing a hydrogen-refuelling infrastructure [8].

High-temperature fuel cells (MCFC and SOFC) are suitable for continuous power/heat production, where the cell temperature can be maintained. In general the high temperature fuel cells exhibit higher efficiency and are less sensitive to fuel composition than low temperature fuel cells. At higher temperatures natural gas can be applied directly as a fuel. In some cases this will, however, require some level of catalysed reforming, where higher hydrocarbons are decomposed and part of the CH₄ is converted into H₂, CO and CO₂.

An unfortunate property of the MCFC is that the presence of molten alkaline salt poses considerable problems with corrosion and creep (transport by wetting metallic surfaces), and the risk of contaminating an internal reforming catalyst.

This thesis deals with SOFC which is at the forefront of the environmentally friendly technologies developing improved energy systems for this century. The advantages of SOFC with respect to other fuel cells are many,

- they present high efficiency with hydrocarbon fuels (~50% using natural gas). They can also achieve this performance with other hydrocarbon fuels such as liquefied petroleum gas, diesel and biogas. As a result of their high operating temperatures, SOFCs can be effectively combined with other new energy technologies such as microturbines to enable the development of electricity generation products with ~60% efficiency. Efficiencies of this level have not been obtained by any other combination of technologies [9],
- SOFCs are made from commonly available ceramic materials which not have moving parts or corrosive liquid electrolytes. Therefore they lead to highly reliable electricity generation systems which require low maintenance,
- the manufacturing process for SOFCs is based on well-known equipment that is widely available and well proven in the manufacture of electronic ceramic components. SOFCs do not require expensive catalysts for their operation, and they can operate directly on methane or natural gas, which avoids expensive and difficult fuel reforming to generate pure hydrogen,
- SOFCs show low air and noise emissions, which allows for flexibility in siting. The high operating temperature results in high-grade exhaust heat which provides a wider range of cogeneration options.

Leading companies in SOFC commercialisation are Siemens-Westinghouse (Germany / USA), Sulzer (Switzerland), Global Thermoelectric (Canada), Ceramic Fuel Cells Ltd. (Australia) and Mitsubishi Heavy Industries (Japan).

In the Netherlands the first 100 kWe SOFC field unit (Westinghouse SOFC technology) was put into operation at the end of 1997 as a demonstration project where 6 Danish Production Companies named ELSAM and a Consortium of 5 Dutch Energy Distribution Companies, EnergieNed and the Dutch Subsidiser NOVEM co-operated [10].

1.2 The solid oxide fuel cell

As said in the previous section high temperature solid oxide fuel cells (SOFCs) provide many advantages over traditional energy conversion systems including high efficiency, reliability, modularity, fuel adaptability, and very low levels of NO_x and SO_x emissions. Furthermore, because of their high temperature of operation ($\sim 1000^\circ\text{C}$), natural gas can be reformed within the cell stack eliminating the need of an expensive, external reformer [10]. This section briefly reviews materials currently used for the different cell components, and discusses the materials that are under investigation to reduce the cell cost. Emphasis is on the anode, its chemistry, research and development aspects. For details of SOFC materials and technology the reader is referred to several extensive reviews on solid oxide fuel cells [2, 9-12].

1.2.1 Principle of operation

The operating principle of the solid oxide fuel cell is illustrated in Figure 1.2. A SOFC essentially consists of two porous electrodes separated by a dense oxygen ion-conducting electrolyte. Oxidant is reduced at the cathode side and fuel is oxidised at the anode. The difference in oxygen activity of the two gases at the electrodes provides a driving force for motion of the oxide ions in the electrolyte. Oxide ions formed by dissociation of oxygen at the cathode under electron consumption migrate through the electrolyte to the anode where they react with hydrogen to form water and

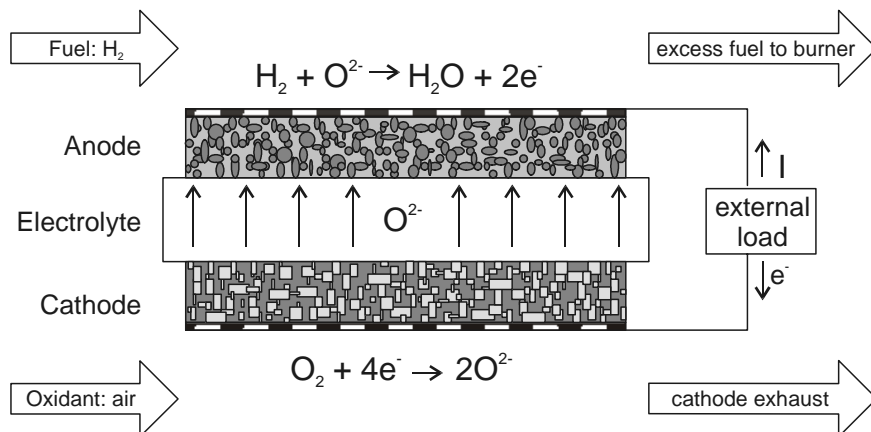


Figure 1.2: A Solid Oxide Fuel Cell.

release electrons.

The electrochemical reactions occur in the electrodes within a distance of less than 10-20 μm from the electrolyte surface [13,14]. This zone is referred to as the functional layer. The part of the electrode exceeding this thickness is primarily a current collector structure, which must be porous to allow gas access to the functional layer. The electrolyte has to be gas impermeable to avoid direct mixing and combustion of the gases. The electrolyte is ceramic, and the electrodes are also based on ceramic materials. Under cell operating conditions the cell produces current as long as the reactants are provided to the electrodes. An open circuit voltage of about 1 volt is attained when the cell is not loaded, defined by the Nernst potential of the different activity of oxygen on the electrodes, which is given by the expression [11]:

$$E = \frac{RT}{4F} \ln \left(\frac{P_{\text{O}_2} (\text{cathode})}{P_{\text{O}_2} (\text{anode})} \right) \quad (1.1)$$

Therefore the cells must be connected in series in a stack to reach higher voltages necessary for most practical purposes. A stack can in principle comprise any number of cells depending on the desired power, and a fuel cell plant can be designed in modules of stacks in series and parallel connections.

1.2.2 Materials for SOFC

The basic components of a ceramic fuel cell stack are the electrolyte, the anode, the cathode and the interconnect. The materials for different cell components have been selected based on the following criteria:

- suitable electrical conducting properties required of different cell components to perform their intended cell functions,
- adequate chemical and structural stability at high temperatures during cell operation as well as during cell fabrication,
- minimal reactivity and interdiffusion among different cell components,
- matching thermal expansion among different cell components.

In addition to the above materials selection criteria, the fabrication processes have been chosen in such a way that every sequential component fabrication process does not affect those components already fabricated and to minimise the cell fabrication cost. The materials used for different cell components are discussed below.

1.2.2.1 Cathode (air electrode)

The air electrode operates in an oxidising environment of air or oxygen at ~1000°C and participates in the oxygen reduction reaction,



i.e., oxygen in the gas phase is reduced to oxygen ions, consuming two electrons in the process. The air electrode in solid oxide fuel cells has to meet the following requirements:

- high electronic conductivity,
- chemical and dimensional stability in environments encountered during cell operation and cell fabrication,
- thermal expansion match with other cell components,
- compatibility and minimum reactivity with the electrolyte and the interconnection with which the air electrode comes into contact,
- sufficient porosity to facilitate transport of molecular oxygen from the gas phase to the air electrode/electrolyte interface.

To satisfy these requirements, lanthanum manganite, suitably doped with alkaline earth elements, is used. The electronic conductivity of lanthanum manganite is due to hopping of an electron hole between +3 and +4 valence states of Mn. This conductivity is enhanced by doping with a divalent ion such as calcium or strontium. The defect chemistry, electrical conduction and cathodic polarisation behaviour of doped lanthanum manganites have been studied in detail [15,16], and alkaline earth doped lanthanum manganite has been found to satisfy all the requirements to be an effective air electrode. Furthermore, the reactivity and interdiffusion studies between

doped lanthanum manganite and yttria stabilised zirconia electrolyte have shown minimal interactions between these two materials at 1000°C [17,18].

1.2.2.2 Electrolyte

Solid oxide fuel cells are based on the concept of an oxygen ion-conducting electrolyte through which the oxide ions (O^{2-}) migrate from the air electrode (cathode) side to the fuel electrode (anode) side where they react with the fuel (H_2 , CO , etc.) to generate an electrical voltage. Oxide materials with fluorite crystal structure such as yttria stabilised zirconia (YSZ), rare earth doped ceria and rare earth doped bismuth oxide have been widely investigated as electrolytes for fuel cells [19,20]. Of these materials, YSZ has been most successfully employed. The Y_2O_3 serves dual roles: it stabilises the high temperature cubic phase in zirconia and also generates oxygen vacancies through the following defect reaction written in the Kroger-Vink notation:



The high oxide ion conductivity in YSZ is attributed to these oxygen vacancies.

For optimum cell performance, the YSZ electrolyte must be free of porosity to avoid gas permeation from one side to the other. It should also be uniformly thin to minimise ohmic loss, and it should have high oxygen ion conductivity with transport number for oxygen ions close to unit and a transport number for electrons as close to zero as possible.

This thesis deals with planar SOFCs with an electrolyte consisting of $(Y_2O_3)_{0.08}-(ZrO_2)_{0.92}$. This composition is the most commonly used for the electrolyte in SOFCs because the material possesses an adequate level of oxygen ion conductivity and exhibits desirable stability in oxidising and reducing atmospheres.

1.2.2.3 Interconnect

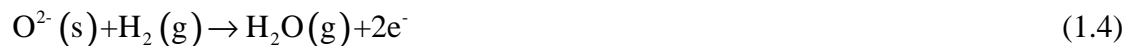
Interconnection serves as the electric contact to the air electrode and also protects the air electrode material from the reducing environment of the fuel on the fuel electrode side. The requirements of the interconnection are most severe of all cell components and include the following:

- nearly 100% electronic conductivity,
- stability in both oxidising and reducing atmospheres at the cell operating temperature since it is exposed to air (or oxygen) on one side and fuel on the other side,
- low permeability for oxygen and hydrogen to minimise direct combination of oxidant and fuel during cell operation
- a thermal expansion close to that of the air electrode and electrolyte,
- non-reactivity with the air electrode and the electric contact material (e.g. nickel).

To satisfy these requirements, doped lanthanum chromite is used as the interconnection material. Lanthanum chromite is a p-type conductor; its conductivity is due to small polaron hopping from room temperature to 1400°C at oxygen pressures as low as 10^{-18} atm. The conductivity is enhanced as lower valence ions (e.g., Ca, Mg, Sr, etc) are substituted on either the La^{3+} or the Cr^{3+} sites.

1.2.2.4 Anode (fuel electrode)

The anode is the part of the SOFC that has main focus in this thesis. The fuel electrode must be stable in the reducing environment of the fuel, should be electronically conducting, and must have sufficient porosity to allow the transport of the products of fuel oxidation away from the electrolyte/fuel electrode interface. In this region the fuel oxidation reaction takes place:



The reducing conditions present on the fuel side of a SOFC permit the use of a metal such as nickel as the fuel electrode. This is primarily due to the excellent catalytic properties of nickel for breaking hydrogen bonds, the low reactivity with other components and fairly low cost [27]. However there exist several problems when nickel is used as anode material; for instance that the thermal expansion of nickel is considerably larger than that of YSZ. Furthermore, nickel can sinter at the cell operating temperature, resulting in a decrease in the fuel electrode porosity. These

problems are minimised by forming a matrix of YSZ around the nickel particles. The YSZ matrix prevents sintering of the nickel particles and decreases the thermal expansion coefficient of the fuel electrode, bringing it closer to that of the electrolyte.

Another drawback of nickel is its reactivity at elevated temperature under high partial pressures of water, such as in partially spent fuel gas. Volatile $\text{Ni}(\text{OH})_2$ is formed and it exerts a partial pressure of about 10^{-6} atm at 950°C [21]. This is not itself critical but due to the rapid passage of fuel gas, the formed $\text{Ni}(\text{OH})_2$ is swept away, diminishing the long term stability of the anode.

Nickel is also an excellent catalyst for cracking of hydrocarbons under deposition of carbon. The carbon formation can cause clogging of gas channels, physical disintegration of the nickel structure and fragmentation of the porous anode. Therefore nickel-based anodes are not suitable for direct operation in dry natural gas without modifications of the catalytic properties.

But despite the undesired properties of nickel in a SOFC nickel-based cermet with the electrolyte YSZ is the most widespread used anode at present [2, 9, 23-27].

1.2.3 *Alternative anode materials*

Based on these drawbacks presented by the state-of-the-art SOFC anode, the Training and Mobility of Researchers (TMR) Network Programme was created by the European Commission in 1997 to address the optimisation of the anode. The ultimate objective of this project was to investigate alternative solid oxide fuel cell anodes capable of efficient operation under methane and hydrogen and which avoid the problems that the Ni based cermet anode presents.

During the past few years a lot of work has been done to investigate alternative anode materials, especially the mixed conducting ceramics like ceria, e.g. doped with gadolinium (GDC). As CeO_2 exhibits both ionic and some electronic conduction under reduction conditions, this material can be used for anodes without forming a composite [22]. Nevertheless this material presents a drawback, which is a redox change in volume for ceria as a consequence of part of the present Ce^{4+} being reduced

to Ce^{3+} under release of oxygen from the lattice. By partially doping with 10 mol% Gd this redox change in volume for ceria is reduced but not eliminated [23].

In recent reports where SOFCs directly utilised hydrocarbon fuels, alternative anode cermet compositions were used, namely, Ni-ceria [28, 29], or Cu-ceria [30, 31, 32]. But it was found that they have considerable limitations. Ni-ceria is not well suited for use with hydrocarbon fuels because the high Ni content (~50 vol%) promotes coking. Thus Ni-ceria was successfully used only with methane and at relatively low temperatures (~500°C). Cu-ceria is better suited for hydrocarbons because Cu does not promote coking. However Cu is not as good electrocatalyst as Ni. Furthermore, Cu has a relatively low melting point, and is thus not compatible with many standard high temperature SOFC fabrication techniques. Liu et al. [34] reported this year a composition consisting of a mixture of $\text{La}_{0.8}\text{Sr}_{0.2}\text{Cr}_{0.8}\text{Mn}_{0.2}\text{O}_{3-\delta}$, which is an electronic conductor, $\text{Ce}_{0.9}\text{Gd}_{0.1}\text{O}_{1.95}$ which is an ionically conducting oxide, and ~4wt% Ni. In this anode composition, the metallic component is mostly replaced by an electronically conducting ceramic that does not promote coking. With an oxide taking the role of electronic conductor, the amount of metal catalyst can be reduced low enough to eliminate coking. This composition shows performances comparable to Ni-GDC with hydrogen and methane, and can be also used with propane and butane, contrarily to Ni-GDC [34].

Ti-doped YSZ has also been extensively studied as anode material for SOFC [35-41]. In combination with nickel this material shows improved anode behaviour with respect to the thermal expansion coefficient and a better electrical conductivity than that of the YSZ, as well as a lower degradation rate at 1000°C. This degradation has been attributed to the lower agglomeration tendency of the nickel particles of the Ti-containing cermets compared to the regular Ni/YSZ cermet [41].

Several perovskite materials based on lanthanum chromite and strontium titanate have also been investigated with regard to their potential application as anodes in SOFCs. They show excellent properties as interconnects. Strontium substituted lanthanum chromites (LSC) have been intensively studied as interconnects [33, 34, 42-48]. They are stable at high temperatures and under reducing conditions. With 5 wt% ruthenium

LSC presented no carbon deposition when used as anode and when methane was used as fuel gas. Its catalytic activity was stable over more than 200h under reducing conditions [46].

1.2.4 Scope of the thesis

This thesis deals with alternative anode materials for solid oxide fuel cells, with emphasis on the perovskite and fluorite-type of materials. The state-of-the-art Ni/YSZ anode has also been subject of study in this work, particularly the elucidation of its hydrogen oxidation reaction mechanism.

A general introduction on SOFC is given in Chapter 1. The principles and materials employed are described. An overview is given on alternative anode materials that are currently being investigated.

In Chapter 2 impedance and polarisation measurements on porous Ni electrodes and modified porous Ni electrodes with fine YSZ particles are presented.

In Chapter 3 the Epelboin's method is implemented to describe and model the hydrogen oxidation reaction on Ni/YSZ anodes.

Electrochemical properties of lanthanum based chromites and Ti-doped YSZ/Ni cermets were specially investigated in Chapters 4 and 5.

In Appendix A a review is presented about percolation theory, which plays a key role when cermets have to be prepared for SOFC electrode applications.

And last, Appendix B presents a model for electrophoretic deposition for a well-stirred suspension, a constant voltage difference across the deposition cell, and a non-ionic solution.

References

- [1] S. Primdahl and M. J. Jorgensen, 'Introduktion til Keramiske Braendsceller', J. Danish Ceram. Soc. 2, 13-20, 1999.
- [2] B. de Boer, PhD Thesis, University of Twente, The Netherlands, 1998.
- [3] W.R. Grove, Phil. Mag. 14, 127, 1839.

- [4] K. Kinoshita, 'Electrochemical oxygen technology', John Wiley & Sons, Inc. New York, 163-259, 1992.
- [5] E. Fontes and E. Nilsson, 'Modelling the fuel cell', *The Industrial Physicist* Aug-Sep, 14-17, 2001.
- [6] Manhattan Scientifics, Inc., www.mhtx.com, Media Center, Bethesda, U.S.A., 2002.
- [7] Industrial Technology Research Institute, www.itri.org.tw, Printable News, Taiwan, 2002.
- [8] Trenton Times N.J., U.S.A., 10-1-2002.
- [9] S.C. Singhal, 'Advances in solid oxide fuel cells', *Solid State Ionics* 135, 305-313, 2000.
- [10] A. Hammou and J. Guindet, 'The CRC handbook of solid state electrochemistry', P.J. Gellings and H.J.M. Bouwmeester (Eds.), Ed. CRC Press. Inc., New York, 408, 1997.
- [11] S.C. Singhal, 'Science and technology of solid oxide fuel cells', *MRS Bulletin*, 16-21, March 2000.
- [12] A. Bieberle, PhD Thesis, ETH Zürich, Switzerland, 2000.
- [13] M. Juhl, S. Primdahl, C. Manon and M. Mogensen, *J. Power Sources* 61, 173, 1996.
- [14] M. Brown, S. Primdahl and M. Mogensen, 'Structure/performance relations for Ni/YSZ anodes for SOFC', *J. Electrochem. Soc.* 147, 2, 475-485, 2000.
- [15] H.U. Anderson, J.H. Kuo and D.M. Sparlin, *Proceedings of the First International Symposium on SOFC*, S.C. Singhal Ed., PV 89-11, The Electrochem. Soc., Pennington, 111, 1989.
- [16] O. Yamamoto, Y. Takeda, R. Kanno and T. Kojima, *Solid State Ionics* 22, 241, 1987.
- [17] S.K. Lau, and S.C. Singhal, 'Potential electrode/electrolyte interactions in solid oxide fuel cells', *Corrosion* 85, 345, 1985.
- [18] O. Yamamoto, Y. Takeda, R. Kanno and T. Kojima, *Proceedings of the First International Symposium on SOFC*, S.C. Singhal Ed., PV 89-11, The Electrochem. Soc., Pennington, 242, 1989.
- [19] J.A. Kilner and B.C.H. Steele, 'Nonstoichiometric oxides', O.T. Sorensen Ed., Academic Press, New York, 233, 1981.
- [20] R.M. Dell and A. Hooper, 'Solid electrolytes', P. Hagenmuller and W. van Gool Eds., Academic Press, New York, 291, 1978.
- [21] A. Gubner, H. Landes, J. Metzger, H. Seeg and R. Stübner, *SOFC V*, U. Stimming, S.C. Singhal, H. Tagawa and W. Lehnert Eds., PV97-40, The Electrochem. Soc., Pennington, 540, 1997.
- [22] O.A. Marina, C. Bagger, S. Primdahl and M. Mogensen, 'A solid oxide fuel cell with gadolinia-doped ceria anode: preparation and performance', *Solid Oxide Fuel Cell* 123, 199-208, 1999.
- [23] S. Primdahl, PhD Thesis, University of Twente, The Netherlands, 1999.
- [24] A.L. Sauvet, J. Guindet and J. Fouletier, *Ionics* 5, 150-155, 1999.
- [25] S. Primdahl, J.R. Hansen, L. Grahl-Madsen and P.H. Larsen, *J. Electrochem. Soc.* 148 (1), A74-A81, 2001.
- [26] B.C.H. Steele, *J. Materials Science* 36, 1053-1068, 2001.
- [27] B.C.H. Steele, 'Materials for fuel cell technology', *Nature* 414, 345-352, 2001.
- [28] E.P. Murray, T. Tsai and S.A. Barnett, *Nature* 400, 649, 1999.
- [29] E.P. Murray and S.A. Barnett, in *Solid Oxide Fuel Cells VI*, S.C. Singhal and M. Dokiya Eds., PV 99-19, The Electrochem. Soc. Proc. Series, Pennington, NJ, 1001, 1999.
- [30] S.D. Park, J.M. Vohs and R.J. Gorte, *Nature* 404, 625, 2000.
- [31] R.J. Gorte, S.D. Park, J.M. Vohs and C.H. Wang, *Adv. Mater.*, 12, 1465, 2000.
- [32] S.D. Park, R.J. Gorte and J.M. Vohs, *Appl. Catal. A*, 200, 55, 2000.

- [33] B.C.H. Steele, *Nature* 400, 619, 1999.
- [34] J. Liu, B.D. Madsen, Z. Ji and S.A. Barnett, *Electrochem. and Solid State Letters* 5 (6) A122-A124, 2002.
- [35] P. Holtapples, J. Bradley, J.T.S. Irvine, A. Kaiser and M. Mogensen, 'Electrochemical characterisation of ceramic SOFC anodes', *J. Electrochem. Soc.* 148, A923-A929, 2001.
- [36] M.T. Colomer, L.S.M. Traqueira, J.R. Jurado and F.M.B. Marques, *Materials Research Bulletin* 30, 515-522, 1995.
- [37] J.T.S. Irvine, A.J. Feighery, D.P. Fagg and S. Garcia-Martin, *Solid State Ionics* 136-137, 879-885, 2000.
- [38] A. Tsoga, A. Naoumidis and P. Nikolopoulos, *Acta Mater.*, 444, 9, 3679-3692, 1996.
- [39] A. Kaiser, A.J. Feighery, D.P. Fagg and J.T.S. Irvine, *Ionics* 4, 215219, 1998.
- [40] K. Kobayashi, S. Yamaguchi, T. Higuchi, S. Shin and Y. Iguchi, *Solid State Ionics* 135, 643-651, 2000.
- [41] D. Skarmoutsos, A. Tsoga, A. Naoumidis and P. Nikolopoulos, *Solid State Ionics* 135, 439-444, 2000.
- [42] J. Sfeir, J. van Herle and A.J. McEvoy, *J. European Cer. Soc.* 19, 897-902, 1999.
- [43] P. Vernoux, M. Guillo, J. Fouletier and A. Hammou, *Solid State Ionics* 135, 425-431, 2000.
- [44] D.P. Fagg, V.V. Kharton, A.V. Kovalevsky, A.P. Viskup, E.N. Naumovich and J.F. Frade, *J. Eur. Ceram. Soc.* 21 (10-11), 1831-1835, 2001.
- [45] A.L. Sauvet and J. Fouletier, *J. Power Sources* 101, 259-266, 2001.
- [46] A.L. Sauvet and J. Fouletier, *Electrochimia Acta* 47, 987-995, 2001.
- [47] G. Pudmich, B.A. Boukamp, M. Gonzalez-Cuenca, W. Jungen, W. Zipprich and F. Tietz, *Solid State Ionics* 135, 433-438, 2000.
- [48] M. Gonzalez-Cuenca, W. Zipprich, B.A. Boukamp, G. Pudmich and F. Tietz, *Fuel Cells* 3-4, 256-264, 2001.

The effect of the presence of fine YSZ particles on the performance of porous nickel electrodes

The electrochemical performance of a porous nickel electrode with its surface modified by deposition of fine yttria-stabilised zirconia (YSZ) powder is compared to that of the 'bare' electrode. Image analysis of the electrode microstructure yields values for the triple phase boundary (TPB) length in the range of 45-61 m/cm². The nickel coverage is in the range of 55-72%. The marked similarity in the performance of bare and modified nickel electrodes in hydrogen oxidation strongly suggests that essential steps in the electrode mechanism on both types of electrodes are similar. The total electrode conductivity increases with increasing TPB length. However, at similar TPB length the electrode conductivity of the modified porous nickel electrode is considerably higher than that of the bare nickel electrode. This result indicates that the presence of fine YSZ particles on the nickel electrode surface creates additional active sites at which the electrode reaction can occur. *

* This chapter has been published in: *Solid State Ionics*, **127**, 269-276 (2000)

2.1 Introduction

In Solid Oxide Fuel Cells (SOFC) a porous cermet made of nickel and yttria-stabilised zirconia (Ni/YSZ) is generally used as anode material [1, 2]. Open porosity is required for the electrode to supply fuel and for the removal of reaction products. The nickel particles, forming a percolative network, have a high catalytic activity and are responsible for transporting electrons from the electrode reaction site to the external circuit. The addition of YSZ is necessary to support the nickel particles, to inhibit coarsening by sintering into larger particles at the usual operating temperature of an SOFC, and to give the cermet a thermal expansion coefficient acceptably close to that of other cell components [2]. As such, the presence of YSZ in the anode is considered to be ‘inactive for the electrode reaction’ and the important steps in the electrode reaction will take place at or in the vicinity of the triple-phase-boundary line (TPB) between electrode, electrolyte and gas phase. An alternative approach is to assign a specific role in the electrochemistry to the YSZ component [3-8].

To clarify the role of the YSZ component in cermet electrodes a comparison is made in this study between the electrochemical performance of a porous nickel electrode and a similar electrode which surface is modified by deposition of fine YSZ. The latter electrode bears resemblance to the cermet electrode, but has a considerably less complex microstructure. In principle, the microstructure of its underlying nickel network is similar to that of the ‘bare’ porous nickel electrode. Using a different layer thickness, annealing time and temperature in subsequent electron beam assisted evaporation steps [9,10], the microstructure of the porous nickel network is varied. Characterisation is performed by image analysis. Both types of electrodes are studied with steady-state polarisation measurements and impedance spectroscopy.

2.2 Experimental

2.2.1 Sample preparation

Ytria-stabilised zirconia rods of 25 mm diameter were obtained by uniaxial pressing of Tosoh-Zirconia TZ-8Y powder at 1.5 bar for 1 min, followed by isostatic pressing at 4000 bar for 5 min. These rods were sintered at 1400°C for 5 h in air. Electrolyte discs of 16.0 mm diameter and 4.0 mm thickness were cut from the sintered rods. A small groove was made around the disc at half thickness for positioning of a Pt wire reference electrode. Prior to use, both sides of the disc were mechanically polished with 320 MESH SiC and 3 μm diamond MM and diamond paste (1 μm). After polishing, the discs were ultrasonically cleaned with ethanol. An Archimedes method was used for determination of its density. Only samples having a density larger than 5.89 $\text{g}\cdot\text{cm}^{-3}$, i.e. 99% of the theoretical density, were used for experiments.

Porous nickel electrodes were prepared by means of an electron beam evaporation process [9,10]. To obtain electrodes with a different microstructure the thickness of the evaporated nickel layer, annealing time and temperature between sequential evaporation steps were varied. Process parameters used for the preparation of the different nickel electrodes are listed in Table 2.1.

For electrochemical experiments, the counter and reference electrodes were painted on the electrolyte disc with Pt paste (Demetron). The whole assembly was annealed at 1000°C for 1 h under reducing conditions (10% H_2 – 90% N_2). The cell geometry is shown schematically in Figure 2.1.

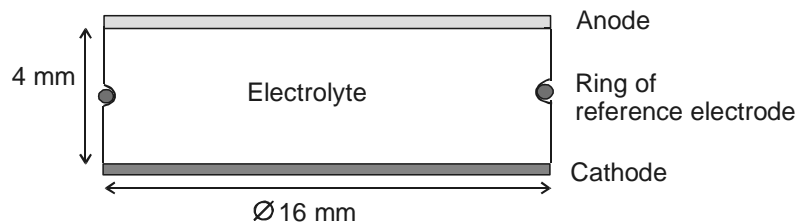


Figure 2.1: Schematic cut of the three-electrode electrochemical cell. The reference electrode is placed in the groove in the middle part of the electrolyte.

The surfaces of three of the seven nickel electrodes were modified with fine YSZ powder. Zirconium-(IV)-nitrate ($\text{Zr}(\text{NO}_3)_4 \cdot 5\text{H}_2\text{O}$) and yttrium-(III)-nitrate ($\text{Y}(\text{NO}_3)_3 \cdot 5\text{H}_2\text{O}$) dissolved in ethanol was used as a precursor solution. The Y:Zr ratio was set equivalent to that in 8mol% YSZ. A small droplet of this solution was placed on the electrode. The solution-treated discs were dried and heated at 200°C for 2 h in air. It should be mentioned that no attempt was made to optimise the procedures for the preparation of the nickel electrodes.

Sample	Layer thickness (nm) of evaporation step					total	Annealing conditions
	Step 1	Step 2	Step 3	Step 4	Step 5		
Ni-1	350	150	150	500		1150	2 h, 1000°C
Ni-2	150	150	150	400	300	1150	2 h, 1000°C
Ni-3	150	150	150	500		950	2 h, 1100°C
Ni-4	150	150	150	500		950	4 h, 1150°C
NiM-1	350	150	150	500		1150	2 h, 1100°C
NiM-2	150	150	150	500	300	1250	2 h, 1100°C
NiM-3	150	150	150	500	300	1250	4 h, 1150°C

Table 2.1: Thickness of the deposited layers of the sequential electron beam evaporation steps during the preparation of the porous nickel electrodes. Intermediate annealing was performed in a 10% H_2 - 90% N_2 gas mixture at a total flow rate of 100 $\text{ml}\cdot\text{min}^{-1}$.

The effect of the different preparation steps on the nickel electrode microstructure was not studied and, therefore, remains unclear. In addition, scanning electron microscopy (SEM) analysis confirmed that no homogeneous dispersion of YSZ particles on the surfaces of the electrodes was obtained and, hence, the coating procedure needs to be improved.

2.2.2 Characterisation of the electrode microstructure

SEM micrographs of the porous nickel electrodes were taken at five different positions on the surface before and after the electrochemical experiments. The pictures obtained were edited to black and white representations, which were transferred into an image analysis system. The results enabled calculation of the total length of the nickel perimeter and the surface coverage by nickel.

2.2.3 Electrochemical characterisation

All electrochemical experiments were performed in a single-gas environment. Hydrogen with 2.3% H₂O at 850°C was introduced with a flow of 100 ml·min⁻¹ regulated by a Brooks 5800E Mass Flow Controller. Two water bubblers controlled the water concentration in the gas mixture. The second water bubbler was used as a cold trap, thereby fixing the water concentration in the gas to the aqueous vapour pressure over water at the bubbler temperature.

Initially, cells maintained under gas flow were heated to 850°C and allowed to stabilise for 50 h. This process was monitored using impedance measurements. Hereafter, reproducible impedance data could be obtained. Characterisation further included, once stable performance was obtained, d.c. polarisation measurements.

Impedance measurements were performed in the frequency range of 1 MHz to 0.01 Hz with a Solartron Frequency Response Analyser 1255 in combination with a Solartron Electrochemical Interface 1287. An excitation voltage of 10 mV (rms) was used to ensure that measurements were performed in the linear regime. The impedance data were analysed using the computer program 'Equivalent Circuit' [11]. The dc polarisation measurements were carried out using a Solartron Electrochemical Interface 1287 for potentiostatic control. Prior to measurements the working electrode was anodically biased, relative to the reference electrode, at 500 mV for 30 min. Hereafter, the bias was decreased stepwise and the current was measured at each bias value. A steady-state current was measured usually within few minutes. The uncompensated resistance of the electrolyte was accounted for when the overpotential was calculated from the bias values. The electrolyte resistance was calculated from data of impedance measurements.

2.3 Results and discussion

2.3.1 Microstructure

Examples of SEM pictures of nickel electrodes with different microstructures are given in Figure 2.2. One SEM picture covers an area of $2.5 \cdot 10^3 \mu\text{m}^2$, which is equivalent to 0.0012% of the total electrode surface area. The results obtained from image analysis before and after electrochemical experiments are given in Table 2.2.

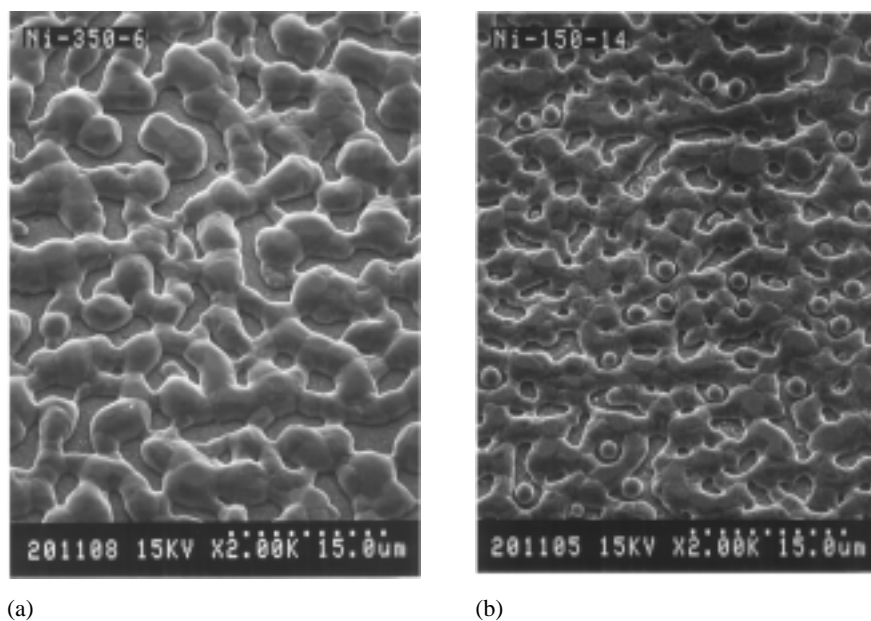


Figure 2.2: SEM micrographs of electrodes (a) Ni-1 and (b) Ni-3 taken after completing the electrochemical experiments on both electrodes.

Small nickel droplets were found to be present before and after electrochemical testing. Their number and shape are not affected by the experiments. As they are incontact with the network they are not expected to be active in the electrode reaction. Therefore, only the continuous nickel network was considered for determination of the nickel perimeter. No clear relationship is found between the nickel coverage and the nickel perimeter

Sample	Perimeter nickel network (m cm^{-2})		Surface coverage Ni (%)	
	Before meas.	After meas.	Before meas.	After meas.
Ni-1	59 (2)	45 (2)	69 (2)	72 (2)
Ni-2	79 (3)	61 (5)	61 (3)	65 (2)
Ni-3	62 (3)	52 (6)	68 (2)	69(3)
Ni-4	56 (4)	56 (5)	59 (3)	60 (2)
NiM-1	45 (2)	53 (3)	60 (2)	55 (2)
NiM-2	59 (3)	54 (4)	76 (3)	73 (4)
NiM-3	59 (5)	59 (6)	69 (3)	65 (2)

Table 2.2: Results from image analysis on the porous electrodes before and after cell evaluation. Average values are given from data taken at five different positions at the surface. The standard deviation is given between parentheses.

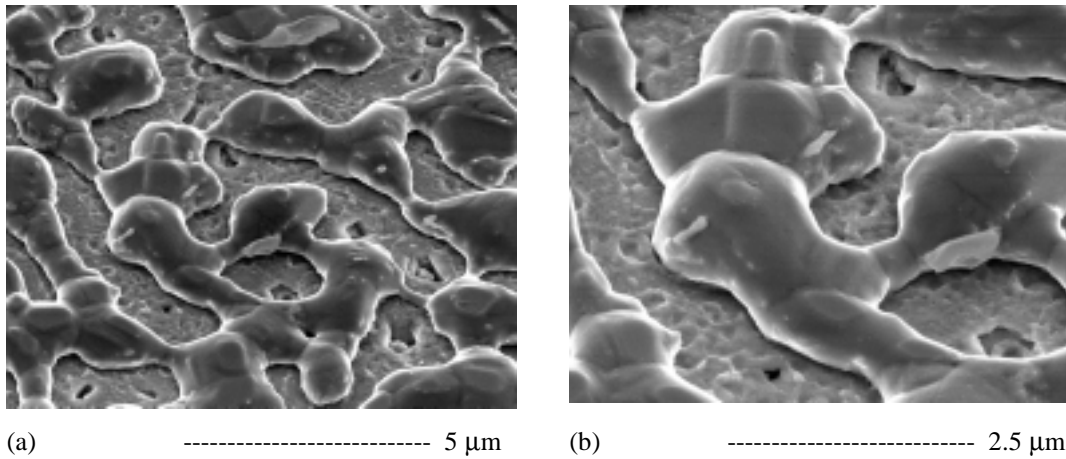


Figure 2.3: SEM micrographs of modified porous nickel electrodes taken after completing the electrochemical experiments.

Figure 2.3 shows SEM images of the modified porous nickel electrode. Small YSZ particles are apparent on the nickel surface as residues of the solution treatment. Sometimes these residues appeared in the form of flakes (not shown). Some roughening of the electrolyte surface is apparent, which could be caused by a thin layer of small YSZ particles. The SEM observations are, however, inadequate in

judging to what extent the presence of small YSZ particles contributes to the TPB length effective for the modified electrodes.

2.3.2 Electrochemical performance

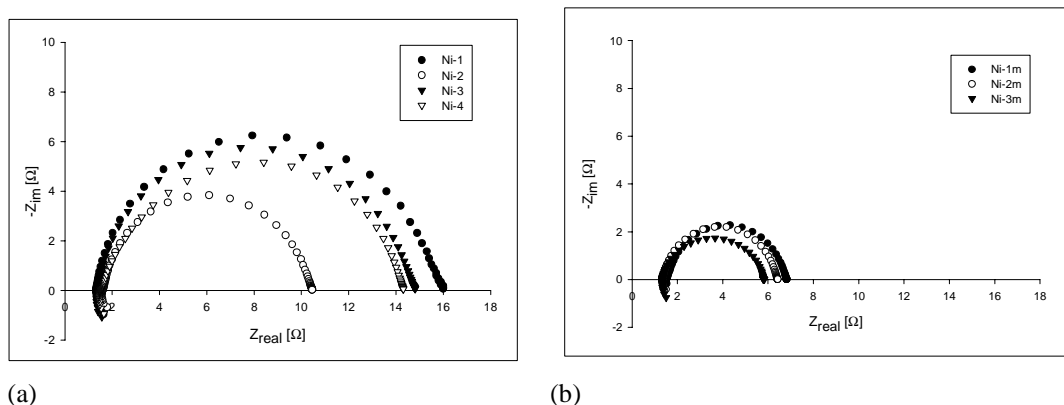


Figure 2.4: Impedance spectra for the (a) bare and (b) modified nickel electrodes from this study measured at zero bias.

Impedance spectra for the ‘bare’ and the modified porous nickel electrodes measured under standard conditions are given Figure 2.4.

Data can be fitted with the circuit $L_w R_{el} (R_1 Q_1) (R_2 Q_2)$. The circuit description code is adopted from Ref. [11]. In this notation L represents an inductance, R a resistance and Q a constant phase element (CPE). The impedance of a CPE is given by $Z_{CPE} = 1/Q(j\omega)^n$, where ω is the angular frequency, j the imaginary unit and n the frequency power. The arc $(R_2 Q_2)$ could not accurately be taken into account for the electrode NiM-3.

Parameters obtained from fitting are listed in Table 2.3. An indication of the quality of the obtained fit is given by the pseudo χ^2 [11]. L_w is associated with the inductance of the wiring and instruments. R_{el} represents the uncompensated electrolyte resistance. A value of 1.42Ω is calculated for R_{el} , assuming a specific conductivity for YSZ at 850°C of $0.148 \Omega^{-1} \cdot \text{cm}^{-1}$ [12].

Table 2.3 shows that this value is in fair good agreement with the experimental values. The scatter is probably introduced by the variation of the position of the wire

reference electrode, which is wrapped around the electrolyte disc. The series combination of (RQ) 's describes the electrode response. The indexing of both arcs is based on their increasing time constant, $\tau \approx RQ$, using the magnitude of Q as an ideal capacitance. To enable a more meaningful comparison of data the values of the frequency powers n_1 and n_2 are fixed to 0.93 and 0.5, respectively (for NiM-3, $n_1 = 0.84$). Within the frequency range of 10 mHz to 50 kHz this procedure yields errors less than 1.5% in both the real and imaginary parts. Only in the case of electrode Ni-4, listed in Table 2.3, the error was about 3%. The (R_1Q_1) arc is found dominant, contributing more than 90% of the total electrode resistance (except for electrode Ni-4). At the low frequency side it overlaps the much smaller contribution of the (R_2Q_2) subcircuit.

	Ni-1	Ni-2	Ni-3	Ni-4	NiM-1	NiM-2	NiM-3
L_w	2.3E-07	5.0E-08	1.9E-07	6.5E-08	1.23E-08	1.14E-07	1.52E-07
R_{el}	1.32	1.59	1.33	1.48	1.50	1.33	1.31
R_1	13.8	8.30	12.5	10.5	4.98	4.76	4.40
Q_1	1.65E-03	1.55E-03	1.86E-03	2.82E-03	1.57E-03	1.92E-03	3.40E-03
n_1	0.93	0.93	0.93	0.93	0.93	0.93	0.84
R_2	0.993	0.588	1.06	2.46	2.78E-01	3.31E-01	
Q_2	6.70E-01	2.61E-01	2.62E-01	7.17E-02	9.68E-02	2.59E-01	
n_2	0.5	0.5	0.5	0.5	0.5	0.5	
R_{tot}	14.8	8.9	13.6	13.0	5.26	5.09	4.40
χ_{ps}^2	2.15E-5	3.44E-5	1.59E-5	2.80E-4	1.24E-05	3.49E-06	1.96E-05

Table 2.3: Parameters obtained from fitting the impedance data of different porous nickel electrodes to the circuit $L_w R_{el} (R_1 Q_1) (R_2 Q_2)$. Resistance R in Ω ; inductance L in H; constant phase element (Q^n) in $s^n \Omega^{-1}$. R_{tot} equals $R_1 + R_2$. The χ_{ps}^2 values indicate reliability of the fitting procedure [11].

The surface modification with fine YSZ seems to decrease the value of R_1 and R_2 , but has no significant effect on the parameters of the constant phase elements obtained from fitting. The same equivalent circuit can be used for both types of electrodes. Therefore, there is no evidence for a change in the reaction mechanism upon modification with YSZ.

Tafel representations of I - η measurements for both types of electrodes are given in Figure 2.5. The Tafel slopes, in both anodic and cathodic directions, slightly diverge with increasing overpotential. For the porous nickel electrodes values of 1.4 and 0.8 were estimated for the apparent anodic and cathodic transfer coefficients, respectively. For the modified porous nickel electrodes the corresponding values are 1.2 and 0.8, respectively. These values were calculated from the first derivative of a polynomial fit to the experimental data at the end values for η in the Tafel plots. The values for both ‘bare’ and modified Ni electrodes are comparable and hence suggest again no apparent change in the reaction mechanism upon modification with YSZ.

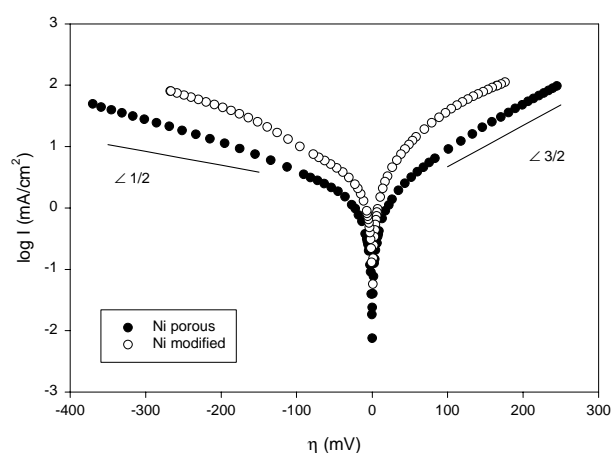


Figure 2.5: Tafel plots for the bare and modified nickel electrodes, showing the anodic and cathodic branches.

2.3.3 Relationship of the microstructure with electrode conductivity

Image analysis of the nickel electrodes before and after electrochemical testing reveals that significant changes have occurred during the measurements (see Table 2.2). These changes are likely to occur in the initial period of 50 h, during which the electrodes are allowed to stabilise (see Section 2). A significant decrease in the total electrode conductivity, σ_{tot} , occurs in the first 30 h of this time period, after which the conductivity tends to become constant with time. The total electrode

conductivity is given by the expression $\sigma_{\text{tot}} = 1/(A \cdot R_{\text{tot}})$, where A is the geometric area of the work electrode.

Figure 2.6 shows for the ‘bare’ and modified nickel, respectively, the total electrode conductivity plotted against nickel perimeter length. In these figures, the conductivity derived from the first impedance measurement during the stabilisation period of 50 h is related to the initial microstructure, whereas the conductivity derived from the last impedance measurement (measured after 50 h stabilisation) is related to the microstructure that was observed after cell evaluation. For the ‘bare’ nickel electrode the data of the first impedance measurements are significantly scattered, while those derived from the last impedance measurement fall more or less on a line. The latter behaviour is expected if the electrode reaction would be confined to the TPB or its close vicinity [13,14]. As seen from Table 2.2, the nickel perimeter of the modified electrodes is less affected by the electrochemical measurements, compared with that observed for the ‘bare’ electrodes.

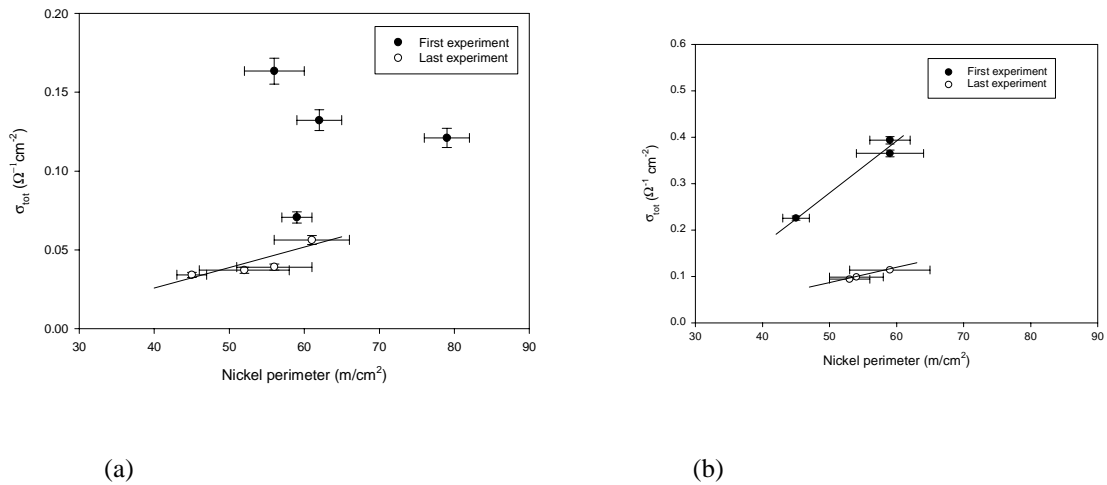


Figure 2.6: Total electrode conductivity as function of the perimeter length of the nickel network for the (a) bare and (b) modified nickel electrodes. The nickel perimeter was obtained from image analysis of the electrode microstructure. The conductivity derived from the first impedance measurement during the stabilisation period of 50 h is plotted against the nickel perimeter obtained *before* and that of the last impedance measurement against the nickel perimeter *after* cell evaluation.

Figure 2.6 (b) shows that the conductivities derived from both first and last impedance measurements follow approximately linear behaviour with the measured nickel parameter length. Also evident from this figure is that the decrease in electrode conductivity during the stabilisation period is not related to a change in the microstructure, at least not on a scale observable with SEM.

Figure 2.7 shows for the two types of electrodes the total electrode conductivity as function of the perimeter length of the nickel network. In both cases, the conductivity increases with the perimeter length. At similar length scale, however, the conductivity of the modified nickel electrode is about twice that exhibited by the bare nickel electrode. This is taken as an indication that the number of active sites has doubled due to the surface modification, but the question arises where these additional sites are located.

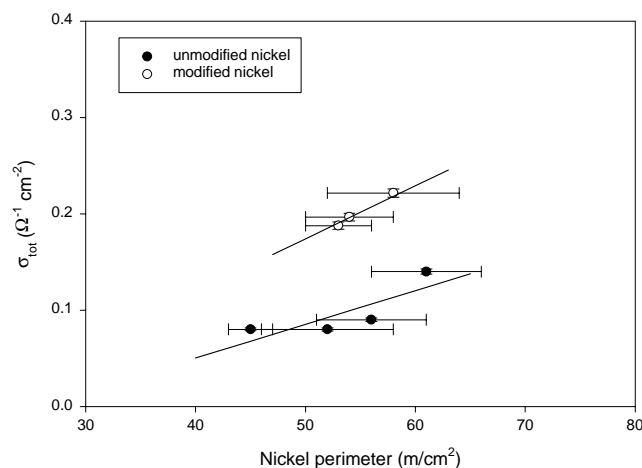


Figure 2.7: Total electrode conductivity as function of the perimeter length of the nickel network for bare and modified porous nickel electrodes. The perimeter length is obtained from image analysis of the electrode microstructure after cell evaluation (Data from Figure 2.6).

When the microstructure is considered in terms of the area of nickel, modification will undoubtedly lead to a decrease in that area being exposed to the gas phase. Since the electrode performance increases upon modification it thus seems that the nickel area

accessible to, e.g., hydrogen adsorbed intermediates does not enter the rate-determining step of the hydrogen oxidation reaction. A plausible explanation for the improved performance of the nickel electrode is that the available TPB area extends with the surface treatment due to roughening of the YSZ surface. Additional research is however required to draw more definite conclusions.

2.4 Conclusions

Porous nickel electrodes on yttria-stabilised zirconia have been modified by dispersion with fine particles of the YSZ phase. The marked similarity in the performance of bare and modified nickel electrodes in hydrogen oxidation strongly suggests that essential steps in the electrode mechanism on both types of electrodes are similar. The significant increase in overall electrode conductivity of the modified electrodes, compared with that of the bare nickel electrodes, could be attributed to an increased number of active sites. Such behaviour resembles that of the Ni/YSZ cermet electrodes in which a large number of active sites is present.

References

- [1] S.C. Singhal, 'Status of solid oxide fuel cell technology', Proc. of the 17th Risø Int. Symp. on Materials Science, High Temperature Electrochemistry: Ceramics and Metals, 123-138, 1996.
- [2] N.Q. Minh, 'Ceramic fuel cells', J. Am. Ceram. Soc. 76, 563-588, 1993.
- [3] M. Mogensen and T. Lindegaard, 'The kinetics of hydrogen oxidation on a Ni/YSZ SOFC electrode at 1000°C', Proc. of Solid Oxide Fuel Cells 1993 (SOFC-III), 484-493, 1993.
- [4] M. Mogensen, 'Electrode kinetics of SOFC anodes and cathodes', Proc. of the 14th Risø Int. Symp. on Materials Science, High Temperature Electrochemical Behaviour of Fast Ion and Mixed Conductors, 117-135, 1993.
- [5] M. Mogensen and S. Skaarup, 'Kinetic and geometric aspects of solid oxide fuel cell electrodes', Solid State Ionics 86-88, 1151, 1996.
- [6] H. Itoh, T. Yamamoto, M. Mori, T. Horita, N. Sakai, H. Yokokawa and M. Dokiya, 'Configurational and electrical behaviour of Ni/YSZ cermet with novel microstructure for solid oxide fuel cell anodes', J. Electrochem. Soc. 144, 641-646, 1997.
- [7] J. Divisek, A. Kornyshev, W. Lehnert, U. Stimming, I.C. Vinke and K. Wioppermann, 'Advanced characterisation techniques for Ni/YSZ cermet electrodes used in SOFC', Electrochemical Proc. 97-18, 606-616, 1997.

- [8] A. Ioselevich, A.A. Kornyshev and W. Lehnert, 'Degradation of SOFC anodes due to sintering of metal particles: correlated percolation model', *J. Electrochem. Soc.* 144, 3010-3019, 1997.
- [9] T.L. Markin, N.J. Bones and R.M. Dell, *Superionic Conductors*, G. Mahan and W. Roth Eds., Plenum Press, New York, 15-35, 1976.
- [10] Y. Yamazaki, T. Namikawa and H. Michibata, *Proc. of the 2nd Int. Symp. on SOFC*, F. Gross, P. Zeghers, S.C. Singhal and H. Iwahara Eds., Office for Official Publications of the European Communities, Luxembourg, 175-181, 1991.
- [11] B.A. Boukamp, 'A nonlinear least squares fit procedure for analysis of immitance data of electrochemical systems', *Solid State Ionics* 20, 31-44, 1986.
- [12] F.P.F. van Berkel and J.P. de Jong, *ECN Internal Report (in Dutch)*, 2918-GR14, 1993.
- [13] T. Norby, O.J. Velle, H. Leth-Olsen and R. Tunold, 'Reaction resistance in relation to three phase boundary length of Ni/YSZ electrodes', *Proc. of the 3rd Int. Symp. on SOFC*, Honolulu, Hawaii, 473-78, 1993.
- [14] J. Mizusaki, H. Tagawa, T. Saito, K. Kamitain, T. Yamamura, K. Hirano, S. Ehara, T. Takagi, T. Hikita, M. Ippommatsu, S. Nakagawa and K. Hashimoto, *J. Electrochem. Soc.* 141, 2129, 1994.

Mechanistic modelling of the H₂ oxidation reaction on Ni/YSZ anodes

The kinetics of the hydrogen oxidation reaction at the Ni/YSZ anode is investigated using the approach that was originally used by Epelboin in 1970 to obtain an expression for the impedance. Experimental impedance data obtained for porous nickel electrodes show an inductive loop at low frequencies. It is shown that this observation can be explained by adopting a reaction scheme in which it is assumed that the surface coverage of intermediate OH⁻ groups is balanced by two consecutive reaction steps. More advanced models are, however, required to fully explain the experimental observations.

3.1 Introduction

The Ni/YSZ system is the state-of-the-art anode of a solid oxide fuel cell (SOFC). At the interface of the three phases, metallic Ni, gaseous H₂-H₂O and ceramic YSZ, hydrogen is oxidised. So far, the kinetics of these processes was studied mainly experimentally using either Ni/YSZ cermet anodes [1-8] or metallic Ni anodes, such as Ni pattern [9-11], Ni point [12-15], or porous Ni electrodes [11,16-20]. Electrochemical information is usually obtained from data of electrochemical impedance spectroscopy (EIS) measurements and from fitting these data to equivalent circuits [21]. However, the interpretation of the results is complicated, since a correlation of the equivalent circuit elements with physical and chemical parameters is not straightforward. Thus, the kinetics of the system can hardly be identified. In addition, studies are often not carried out under the same experimental conditions, so that it is cumbersome to compare the plain impedance data from different studies. Despite the difficulties concerning the interpretation of the EIS data, various reaction mechanisms have been proposed for the Ni / YSZ / H₂-H₂O system in the literature. Extensive summaries are given in Refs. [20, 22, 23]. It should be noticed that so far no consensus exists concerning the reaction mechanism. Neither is it evident whether the (electro-)chemical reactions take place only at the surfaces of Ni and YSZ, or at the triple phase boundary.

In contrast to the numerous experimental studies summarised in Refs. [20, 22, 23] theoretical work in the field of SOFCs is rare. Kinetic aspects of the underlying electrochemical processes under SOFC operating conditions have only recently been considered: first, simulations on reaction mechanisms devoted to SOFCs focused on the Au / YSZ / O₂ system [24, 25]. Impedance spectra were simulated from an electrochemical model. But simulations of the reactions in an operating SOFC are only at the beginning and the interpretation of the underlying reaction mechanisms is still problematic. Furthermore, in the field of surface science and catalysis high-temperature data on the Ni / H₂-H₂O system are very scarce. Therefore, new methods and analysis techniques are required in order to investigate the kinetics. This paper

reports on the technique introduced by Epelboin [26-31] for the analysis of the impedance properties of surface-controlled reactions, but this time applied to the Ni / YSZ / H_2 - H_2O SOFC anode. The aim of this research is to simulate electrochemical impedance spectra using a simple mechanistic model for the hydrogen oxidation reaction, and to compare these with experimental data obtained under well-defined conditions of gas phase and temperature as a function of overpotential.

3.2 Experimental

3.2.1 Sample preparation

The electrolyte consists of a YSZ disc (Tosoh, TZ-8Y) of 4 mm thickness and 16 mm diameter. The preparation procedure is described in Section 2.2.1 of this thesis.

The porous nickel electrode was prepared by means of an electron beam evaporation process (see Chapter 2). The total electrode area was 2 cm^2 . The thickness of the formed layer was estimated to be about $2 \mu\text{m}$.

For electrochemical experiments the counter and reference electrodes were painted on the electrolyte disc with Pt paste (Demetron). The whole assembly was annealed at 1000°C for 1 h under reducing conditions (10% H_2 - 90% N_2). The cell geometry is shown schematically in Figure 3.1.

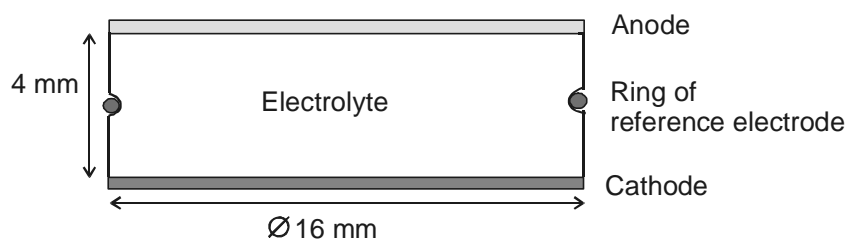


Figure 3.1: Schematic cut of the three-electrode electrochemical cell. The reference electrode is placed in the groove in the middle part of the electrolyte.

3.2.2 Electrochemical characterisation

The Ni electrode properties have been studied by Electrochemical Impedance Spectroscopy (EIS) in a three-electrode arrangement in a single-chamber cell at atmospheric pressure.

At standard conditions a gas flow of $100 \text{ ml}\cdot\text{min}^{-1}$ H_2 with 2.3% H_2O at 850°C was used. Brooks 5800E Mass Flow Controllers regulated all gas flows. Passing the gas mixture through a water bubbler system in a temperature bath controlled the water vapour pressure.

The details of the impedance measurements have been described elsewhere [11]. In summary, impedance measurements were performed in the frequency range of 1 MHz to 0.01 Hz with a Solartron Frequency Response Analyser 1255 in combination with a Solartron Electrochemical Interface 1287. An excitation voltage of 10 mV (rms) was used to ensure that measurements were performed in the linear regime. Also, impedance measurements under certified conditions were carried out at different anodic polarisation values.

3.3 Theoretical background

3.3.1 Electrode reactions

At the anode of a SOFC the overall hydrogen oxidation reaction, $\text{H}_2 + \frac{1}{2} \text{O}_2 \rightleftharpoons \text{H}_2\text{O}$, is supposed to occur in a sequence of steps (see Section 3.4), in which various (intermediate) species can participate. We will assume that all these reaction steps have the form:



where the superscripts (f) and (b) denote forward and backward processes, k_r is the reaction rate constant of reaction r , and $v_{\ell,r}$ the stoichiometric constant of each species ℓ in reaction r . For a Ni/YSZ anode, examples of participating species may include

adsorbed hydrogen and water, but also vacant adsorption sites on the anode surface. When the surface is considered to exist of a finite number of such adsorption sites the concentrations of the participating species are no longer independent, i.e., site-exclusion constraints have to be satisfied. In the case of Langmuir type adsorption, for each type of surface site¹ such a constraint appears as:

$$1 - \sum_{\ell}^{\text{species}} \nu_{con,\ell} \theta_{\ell} = 0 \quad (3.2)$$

with θ the fractional coverage, and ν_{con} a stoichiometric coefficient denoting whether a species participates in the site-exclusion constraint. The total number of species minus the number of site-exclusion constraints remains as independent fractional coverages.

These independent fractional coverages can be calculated from the conservation equations:

$$\left(\frac{\partial c_i^s \theta_i}{\partial t} \right) = \xi_i \quad (3.3)$$

with ξ_i the rate of production or consumption of species i [$\text{mol}\cdot\text{s}^{-1}\cdot\text{m}^{-2}$], and c_i^s the maximum adsorbed concentration² [$\text{mol}\cdot\text{m}^{-2}$]. Consequently, when the reaction kinetics is known, it is possible to calculate the composition at the surface.

To simplify the calculations it is assumed that no mass transfer limitations occur during the H_2 oxidation process.

¹ More than one type of site may be present; for the Ni/YSZ anode a distinction may be made between sites at the Ni and YSZ surfaces.

² Depends on species, e.g., when H_2 adsorbs dissociatively on Ni; H_{ad} and vacant Ni sites S_{Ni} have a maximum concentration equal to the total number of adsorption sites on Ni. When H_2 also adsorbs at YSZ, $H_{ad,Ni}$ and $H_{ad,YSZ}$ should be treated as two individual species.

3.3.2 Reaction kinetics

The rate ξ_i follows from a summation of all nr reactions steps occurring at the surface

$$\xi_i = \sum_r^{nr} \nu_{i,r} (P_r^{(f)} - P_r^{(b)}) \quad (3.4)$$

with P the production rate [$\text{mol}\cdot\text{s}^{-1}\cdot\text{m}^{-2}$], and ν the stoichiometric coefficient. Assuming that each reaction step obeys power law kinetics, the production rates in forward and backward directions are:

$$P_r^{(f,b)} = k_r^{(f,b)}(E) \cdot \prod_{\ell} \theta_{\ell}^{n_{\ell,r}^{(f,b)}} \quad (3.5)$$

with θ the fractional coverages, $n_{\ell,r}$ the reaction order of reaction r in ℓ , and k the specific reaction rate constant [$\text{mol}\cdot\text{s}^{-1}\cdot\text{m}^{-2}$]. Note that the maximum concentrations c_i^s are lumped into the reaction rate constants,

$$k_r(E) = k_r^*(E) \cdot \prod_{\ell} (c_{\ell}^s)^{n_{\ell,r}} \quad (3.6)$$

For reactions in which electron transfer occurs, the reaction rate constant is a function of the electric potential E [V]:

$$\begin{aligned} k_r^{(f)}(E) &= k_r^{(f)} \cdot \exp(\nu_{e,r} (1-\beta) fE) \\ k_r^{(b)}(E) &= k_r^{(b)} \cdot \exp(\nu_{e,r} (-\beta) fE) \end{aligned} \quad (3.7)$$

with $\nu_{e,r}$ the number of electrons transferred in reaction r , β the symmetry coefficient, and f the Faraday constant F [$\text{C}\cdot\text{mol}^{-1}$] divided by RT [$\text{J}\cdot\text{mol}^{-1}$]. A summation over all reactions, of the number of electrons transferred, yields the Faradaic current [$\text{C}\cdot\text{s}^{-1}$]:

$$I = FA \sum_r \nu_{e,r} (P_r^{(f)} - P_r^{(b)}) \quad (3.8)$$

where A is the geometric surface area of the anode.

3.3.3 Electrode potential at equilibrium

At equilibrium the Faradaic current is zero. The equilibrium condition requires that forward and backward rates are balanced. The corresponding equilibrium constant reads:

$$K_{\text{overall}}^{\text{eff.}} = \frac{P_{H_2O}}{P_{H_2}} = \prod_r \left(\frac{k_r^{(f)}(E_{\text{eq}})}{k_r^{(b)}(E_{\text{eq}})} \right)^{\nu_r} \quad (3.9)$$

where ν_r is the stoichiometric number of reaction r [32], and E_{eq} the potential at which equilibrium is observed. Accordingly the equilibrium potential can be calculated from

$$E_{\text{eq}} = \frac{1}{\sum (\nu_r \cdot \nu_{e,r}) f} \cdot \left[\ln \left(\frac{P_{H_2O}}{P_{H_2}} \right) + \sum \nu_r \ln \left(\frac{k_r^{(b)}}{k_r^{(f)}} \right) \right] \quad (3.10)$$

It should be noted that in practice the potential E_{eq} is measured relative to a reference electrode. The choice of the reference electrode will be reflected in the pre-exponential values of the reaction rate constants.

3.3.4 Non-equilibrium

Generally, the electrode potential is expressed in terms of an overpotential $\eta = E - E_{\text{eq}}$. If the overpotential is unequal to zero, the forward and backward rates of each reaction step are no longer the same. The corresponding current can be calculated from equation (3.8), which requires knowledge of the kinetics and the values of the fractional coverages at the surface.

If k , ν and β etc. are known parameters, only the fractional coverages need to be determined. Consequently, there are nc independent variables and an equal number of independent equations is required. For each ‘virtual species’, i.e., the vacant sites, the corresponding site-exclusion constraint (3.2) provides an independent equation. The conservation equations (3.3) for the ‘real’ adsorbed species provide the remaining independent equations.

If the system is at steady state, the left hand sides of (3.3) vanish. Hence,

$$\xi_i = 0 \quad (3.11)$$

The set of nc equations (3.2) and (3.11) is solved using a Newton-Rhapson iteration procedure;

$$\begin{aligned} \sum_{\ell}^{nc} v_{con,\ell} \delta\theta_{\ell} &= 1 - \sum_{\ell}^{nc} v_{con,\ell} \theta_{\ell}^{(N)} \\ \sum_{\ell} \left(\frac{\partial \xi_i}{\partial \theta_{\ell}} \right)^{(N)} \delta\theta_{\ell} &= -\xi_i^{(N)} \end{aligned} \quad (3.12)$$

with N the number of iterations performed, and δ the estimated error in the corresponding variable, i.e., $\delta\theta_{\ell} = \theta_{\ell}^{(N+1)} - \theta_{\ell}^{(N)}$.

This set of linear equations can be written in $(nc \times nc)$ matrix form:

$$\mathbf{Ax} = \mathbf{b} \quad (3.13)$$

and solving it, yields new estimates for the independent variables. Subsequently, the updated set of equations can again be solved, and the procedure is repeated until the Euclidean, or l_2 , vector norm $\|\mathbf{b}\| = \sqrt{b_1^2 + \dots + b_n^2}$ [33] of vector \mathbf{b} has sufficiently reduced to zero.

3.3.5 Impedance

If a sine wave perturbation ΔE is superimposed on the cell voltage E , the sine wave responses to the fractional coverages and current, $\Delta\theta_{\ell}$ and ΔI , can be obtained by linearising the concentration balance equations,

$$\left(\frac{\partial c_i^s \theta_i}{\partial t} \right) = j\omega \cdot c_i^s \Delta\theta_i = \sum \left(\frac{\partial \xi_i}{\partial \theta_{\ell}} \right) \Delta\theta_{\ell} + \left(\frac{\partial \xi_i}{\partial E} \right) \Delta E \quad (3.14)$$

and the expression for the Faradaic current:

$$\Delta I = \sum \left(\frac{\partial I}{\partial \theta_{\ell}} \right) \Delta\theta_{\ell} + \left(\frac{\partial I}{\partial E} \right) \Delta E \quad (3.15)$$

We prefer to rewrite the set in terms of the impedance:

$$\frac{1}{Z} = \left(\frac{\Delta I}{\Delta E} \right) \quad (3.16)$$

which results in:

$$\left(\frac{\Delta I}{\Delta E} \right) - \sum \left(\left(\frac{\partial I}{\partial \theta_\ell} \right) \left(\frac{\Delta \theta_\ell}{\Delta E} \right) \right) = \left(\frac{\partial I}{\partial E} \right) \quad (3.17)$$

$$j\omega \cdot C_i^s \left(\frac{\Delta \theta_i}{\Delta E} \right) - \sum \left(\left(\frac{\partial \xi_i}{\partial \theta_\ell} \right) \left(\frac{\Delta \theta_\ell}{\Delta E} \right) \right) = \left(\frac{\partial \xi_i}{\partial E} \right) \quad (3.18)$$

This is a linear set of $(nc+1)$ equations, containing $(nc+1)$ independent (complex) variables $(\Delta \theta_i/\Delta E, \Delta I/\Delta E)$, and can thus be solved. The total impedance is calculated from:

$$Z_{\text{tot}} = \frac{Z}{1 + j\omega C_{\text{dl}} Z} + R_{\text{el}} \quad (3.19)$$

where C_{dl} is the double layer capacitance and R_{el} is the electrolyte resistance.

Expression (3.19) can be fitted to experimental data using a multi-dimensional Simplex non-linear regression routine [34].

3.4 Electrochemical models for the Ni / YSZ / H_2 - H_2O anode

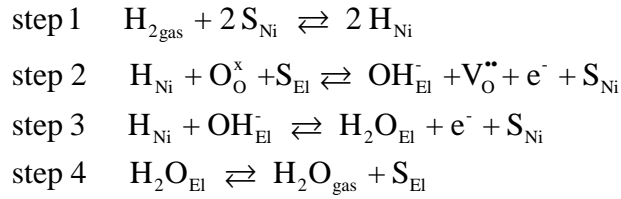
Different mechanistic models for the electrochemical oxidation of hydrogen on Ni or Ni/YSZ cermets have been proposed in the literature [5, 11, 32-35]. Up to now there is no consensus concerning a single model. A survey of proposed models is given below. Each of these models includes adsorption, surface and charge transfer reactions, which take place either at the Ni or at the YSZ surfaces, in the close vicinity of triple phase boundary regions, where Ni, YSZ and the gas phase meet.

3.4.1 Typical models reported in literature

Models are divided here in two groups, depending on where the different reaction steps take place: exclusively at Ni or at both Ni and YSZ.

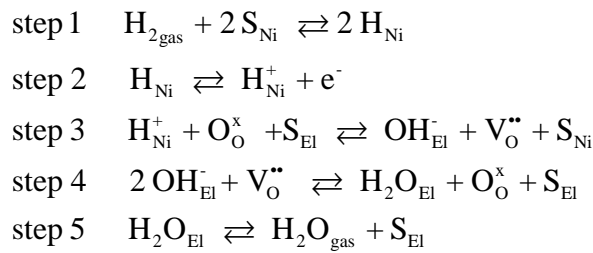
3.4.1.1 Schemes involving reaction steps occurring at both Ni and YSZ

De Boer [11] postulated the following sequence of reactions at the porous nickel anode:



where Ni is the sink for electrons, the subscript *El* denotes species adsorbed on YSZ and *Ni* denotes species adsorbed on nickel. Correspondingly, S_{Ni} and S_{El} denote vacant sites on the nickel electrode surface and the YSZ surface, respectively. The author assumed the dissociative adsorption of hydrogen to occur on the Ni surface (step 1), charge transfer between hydrogen and both lattice oxygen and hydroxyl ions at the triple phase boundary (steps 2 and 3, respectively) and desorption of water molecules from the YSZ surface (step 4).

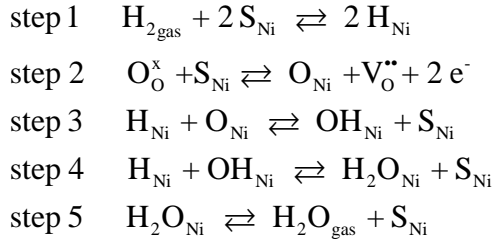
Mogensen et al. [38] reported a scheme in which protons act as mediators in the reaction:



Because the high concentration of electronic charge carriers in metallic nickel will effectively screen the charge of adsorbed protons, it is debatable whether the entities should be treated as protons or neutral hydrogen atoms. This scheme is not considered any further in this study.

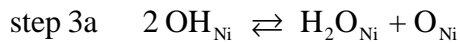
3.4.1.2 Schemes involving reaction steps occurring only at the Ni surface

Mizusaki *et al.* [37] proposed the following scheme for the electrode reaction, which was assigned to proceed only via the nickel surface:

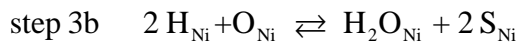


These authors conducted a series of studies on Ni patterned electrodes on YSZ single crystals. They assume lattice oxygen to adsorb on Ni near the TPB via charge transfer. Hydrogen is supposed to react with oxygen atoms and hydroxyl groups to form hydroxyl groups and water, respectively (steps 3 and 4). All surface intermediates involved bear no charge, which presents a marked difference with respect to the above formulations of the hydrogen oxidation mechanism, where both charged and uncharged species occur.

Bieberle *et al.* [32] altered the scheme proposed by Mizusaki *et al.* [37]. They introduced one more, parallel, step in which two hydroxyl groups react under formation of water and oxygen atoms, according to

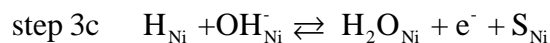
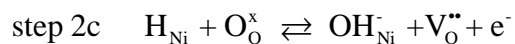


Ihara *et al.* [36] presented a model for Ni/YSZ cermets in which all reaction steps take place on nickel with surface coverages of H, O and H_2O considered to be in equilibrium. The reaction scheme is similar to that proposed by Mizusaki *et al.*, in which steps 3 and 4 are replaced by:



In their model Ihara *et al.* assumed this reaction to be the rate-determining step. They claim that their model can explain the different characteristics observed in their experimental data. Reaction step 3b, however, considers collision between three atoms, which is not very likely from a reaction kinetic point of view.

An alternative scheme is proposed in this work, which is a slight variation of that presented by De Boer [11]. It is assumed that all reaction steps take place on Ni. The resulting reaction scheme resembles that of Misuzaki *et al.*, in which steps 2, 3, 4 are replaced by,



The most essential assumption in this mechanism is that only one electron transfer can take place at a time, while Mizusaki *et al.* [37], Ihara *et al.* [36] and Bieberle *et al.* [32] assume a two-electron transfer step (step 2).

3.5 Results and discussion

Impedance measurements were performed under well-defined conditions at different overpotentials (see Section 3.2.2). Data are presented in Figure 3.2.

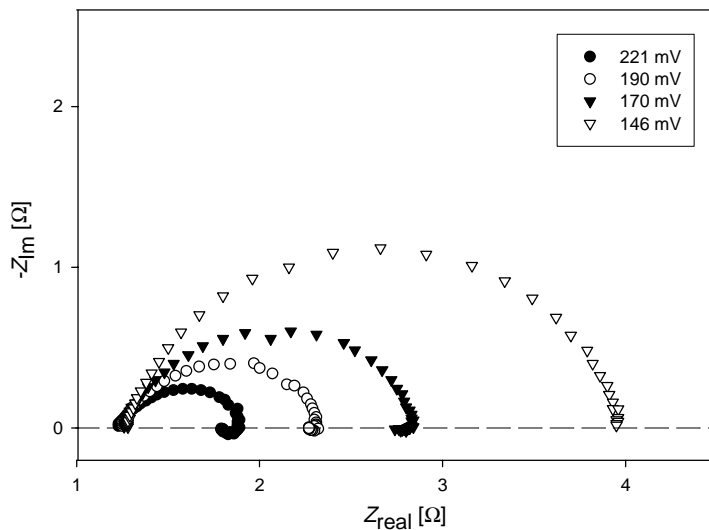


Figure 3.2: Impedance spectra for a porous Ni anode measured at different values for the anodic overpotential.

From this figure it is immediately apparent that at high values for the overpotential the impedance includes an inductive loop. Its occurrence can be explained in a multistep approach of electrode kinetics by the relaxation of the electrode coverage of an adsorbed intermediate [26-31]. Figure 3.3 shows a fit of the reaction scheme proposed by De Boer [11] to the experimental data obtained at potential 221 mV, taking $\beta = 1/2$. In this scheme the concentration of OH^- groups is bounded by two consecutive reaction steps. The kinetic parameters used in fitting giving the best agreement are listed in Table 3.1. Although the fit is rather poor, the occurrence of the inductive loop at low frequency values in the experimental impedance plot is nicely reproduced. Similar results were obtained for the adapted version of the model of De Boer, in which the reactions occur on Ni. Fitting was not possible by invoking above models proposed by Mizusaki *et al.* [37], Ihara *et al.* [36] and Bieberle *et al.* [32]. Figure 3.4 shows the Bode plot corresponding to the data presented in Figure 3.3. Here again the essential features are reproduced. It was however not possible to obtain a unique set of kinetic parameters to fit the observed evolution of the impedance spectra with increasing overpotential values. Clearly more advanced reaction schemes must be invoked to explain the experimental observations.

k_1^f / k_1^b	0.15 / $2 \cdot 10^6$
k_2^f / k_2^b	0.15 / 0.85
k_3^f / k_3^b	$4.5 / 7.5 \cdot 10^{-4}$
k_4^f / k_4^b	25 / 0.03
C_{dl}	25 F/m
R_{el}	1.23 Ω
c^s	1 mol·m ⁻²

Table 3.1: Parameters obtained from fitting the impedance spectra ($\eta = 221$ mV) to the reaction scheme proposed by the Boer [11].

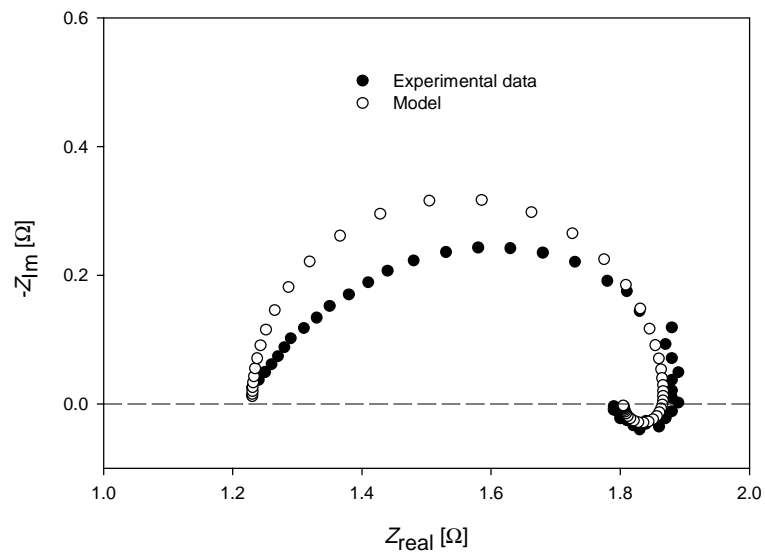


Figure 3.3: Fit of the scheme proposed by De Boer [11] to experimental impedance data at $\eta = 221\text{mV}$. Kinetic parameters used in the fitting procedure are listed in Table 3.1.

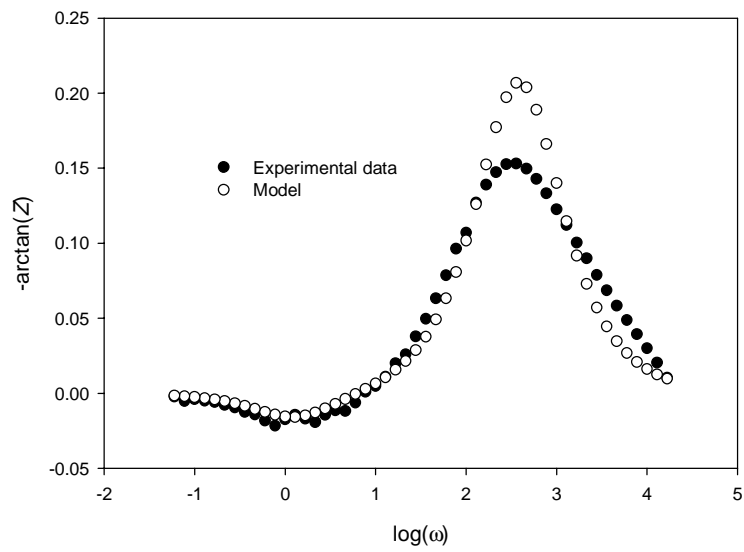


Figure 3.4: Bode plot presentations of the experimental and simulated impedance data shown in Figure 3.3.

3.6 Conclusions

On the basis of the reported work, it is reasonable to conclude that charge transfer processes dominate the hydrogen oxidation kinetics occurring at the nickel anode. The characteristic inductive loop can be reproduced by assuming that two consecutive reaction steps govern the surface coverage of intermediate OH⁻ groups. More advanced reaction schemes must be invoked to fully explain the experimental observations.

References

- [1] T. Kawada, N. Sakai, H. Yokokawa, M. Dokiya, M. Mori and T. Iwata, *Solid State Ionics* 40/41, 402, 1990.
- [2] J. Geyer, H. Kohlmüller, H. Landes, R. Stübner, in: U. Stimming, S.C. Singhal, H. Tagawa and W. Lehnert Eds., *Proc. of the 5th Int. Symp. on SOFC (SOFC-V)*, Aachen, Germany, The Electrochemical Society, Pennington, NJ, USA, 585, 1997.
- [3] S. Primdahl and M. Mogensen, *J. Electrochem. Soc.* 144, 3409, 1997.
- [4] M. Mogensen and S. Skaarup, *Solid State Ionics* 86-88, 1151, 1996.
- [5] M. Mogensen, S. Sunde and S. Primdahl, in: F.W. Poulsen, N. Bonanos, S. Linderorth, M. Mogensen, B. Zachau-Christiansen Eds., *Proc. of the 17th Risø Int. Symp. on Mat. Sci.: High Temperature Electrochemistry: Ceramics and Metals*, Risø National Laboratory, Roskilde, Denmark, 77, 1996.
- [6] P. Holtappels, L.G.J. de Haart and U. Stimming, *J. Electrochem. Soc.* 146, 1620, 1999.
- [7] P. Holtappels, L.G.J. de Haart and U. Stimming, *J. Electrochem. Soc.* 146, 2976, 1999.
- [8] J. Divisek, A. Kornyshev, W. Lehnert, U. Stimming, I.C. Vinke and K. Wippermann, in: U. Stimming, S.C. Singhal, H. Tagawa, W. Lehnert Eds., *Proc. of the 5th Int. Symp. on SOFC (SOFC-V)*, Aachen, Germany, The Electrochemical Society, Pennington, NJ, USA, 606, 1997.
- [9] J. Mizusaki, H. Tagawa, T. Saito, T. Yamamura, K. Kamitani, K. Hirano, S. Ehara, T. Takagi, T. Hikita, M. Ippomatsu, S. Nakagawa and K. Hashimoto, *Solid State Ionics* 70/71, 52, 1994.
- [10] J. Mizusaki, H. Tagawa, T. Saito, T. Yamamura, K. Kamitani, K. Hirano, S. Ehara, T. Takagi, T. Hikita, M. Ippomatsu, S. Nakagawa and K. Hashimoto, *J. Electrochem. Soc.* 141, 2129, 1994.
- [11] B. de Boer, PhD Thesis, University of Twente, The Netherlands, 1998.
- [12] R.J. Aaberg, PhD Thesis, NTNU Trondheim, Norway, 1998.
- [13] T. Norby, O.J. Velle, H. Leth-Olsen and R. Tundold, in: S.C. Singhal, H. Iwahara Eds., *Proc. of the 3rd Int. Symp. on SOFC (SOFC-III)*, Honolulu, Hawaii, USA, The Electrochemical Society, Pennington, NJ, USA, 473, 1993.
- [14] T. Norby and P. Kofstad, in: F.W. Poulsen, N. Bonanos, S. Linderorth, M. Mogensen, B. Zachau-Christiansen Eds., *Proc. of the 17th Risø Int. Symp. on Mat. Sci.: High Temperature Electrochemistry: Ceramics and Metals*, Risø National Laboratory, Roskilde, Denmark, 381, 1996.

- [15] F.Z. Mohamedi-Boulenouar, J. Guindet and A. Hammou, in: U. Stimming, S.C. Singhal, H. Tagawa, W. Lehnert Eds., Proc. of the 5th Int. Symp. on SOFC (SOFC-V), Aachen, Germany, The Electrochemical Society, Pennington, NJ, USA, 441, 1997.
- [16] S.P. Jiang and S.P.S. Badwal, J. Electrochem. Soc. 144, 3777, 1997.
- [17] S.P. Jianga and S.P.S. Badwal, Solid State Ionics 123, 209, 1999.
- [18] S.P. Jiang and S.P.S. Badwal, Solid State Ionics 122, 211, 1999.
- [19] N. Nakagawa, H. Sakurai, K. Kondo, T. Morimoto, K. Hatanaka and K. Kato, J. Electrochem. Soc. 142, 3474, 1995.
- [20] S. Primdahl, PhD Thesis, University Twente, The Netherlands, 1999.
- [21] J.R. Macdonald, Impedance Spectroscopy, Wiley, New York, NY, USA, 1987.
- [22] K. Wippermann, in: K. Nisanciogly Ed., Materials and Mechanisms: 12th SOFC Workshop, Wadahl, Norway, International Energy Agency, Paris, 31, 1999.
- [23] A. Bieberle, PhD Thesis, ETH Zürich, Zürich, Switzerland, 2000.
- [24] B.A. van Hassel, B.A. Boukamp and A.J. Burggraaf, Solid State Ionics 48, 139, 1991.
- [25] B.A. van Hassel, B.A. Boukamp and A.J. Burggraaf, Solid State Ionics 48, 155, 1991
- [26] I. Epelboin and M. Keddam, J. Electrochem. Soc. 117, 1052, 1970.
- [27] I. Epelboin and R. Wiart, J. Electrochem. Soc. 118, 577, 1971.
- [28] I. Epelboin and M. Keddam, Electrochim. Acta 17, 177, 1972.
- [29] I. Epelboin M. Ksouri and R. Wiart, J. Electrochem. Soc. 122, 1206, 1975.
- [30] I. Epelboin, C. Gabrielli, M. Keddam and H. Takenouti, Electrochim. Acta 20, 913, 1975.
- [31] I. Epelboin M. Ksouri and R. Wiart, J. Electroanal. Chem. 65, 373, 1975.
- [32] J. O' M Bockris, A.K.N. Reddy and M. Gamboa-Aldeco, Modern Electrochemistry 2A, 2nd Ed., KA/PP, New York, 1183, 2000.
- [33] E. Kreyszig, Advanced Engineering Mathematics, 6th edition, John Wile & Sons, New York, 1024, 1988.
- [34] W.H. Press, S.A. Teukolsky, W.T. Vetterling and B.P. Flannery, Numerical Recipes in Fortran 77, 2nd Ed., Cambridge University Press, Cambridge, 402-406, 1992.
- [35] A. Bieberle and L.J. Gauckler, Solid State Ionics 146, 23-41, 2002.
- [36] M. Ihara, T. Kusano and C. Yokoyama, J. Electrochem. Soc. 148, A209-A219, 2001.
- [37] J. Mizusaki, T. Yamamura, N. Mori, H. Tagawa, in: F.W. Poulsen, N. Bonanos, S. Linderorth, M. Mogensen and B. Zachau-Christiansen Eds., Proc. of the 17th Risø Int. Symp. on Mat. Sci.: High Temperature Electrochemistry: Ceramics and Metals, Risø National Laboratory, Roskilde, Denmark, 363, 1996.
- [38] M. Mogensen and T. Lindegaard, in: F.W. Poulsen, N. Bonanos, S. Linderorth, M. Mogensen and B. Zachau-Christiansen Eds., Proc. of the 3th Risø Int. Symp. on SOFC, Risø National Laboratory, Roskilde, Denmark, 484, 1993.

Chromite-titanate perovskites for application as anodes in solid oxide fuel cells

Two types of lanthanum-based chromite-titanate perovskite materials have been tested for use as porous ceramic anodes in SOFC. The ceramic electrodes were found to be quite stable and reproducible. The calcium- or strontium-substituted chromium-rich materials, with composition $\text{La}_{0.7}\text{A}_{0.3}\text{Cr}_{0.8}\text{Ti}_{0.2}\text{O}_{3-\delta}$ ($\text{A} = \text{Ca}, \text{Sr}$), showed *p*-type conductivity under reducing conditions. The titanium-rich composition, $\text{La}_{0.7}\text{Ca}_{0.3}\text{Cr}_{0.2}\text{Ti}_{0.8}\text{O}_{3-\delta}$, showed *n*-type conductivity. Both types of materials were active electrodes in a $\text{H}_2/\text{H}_2\text{O}$ gas mixture at 850°C . The electronic conductivity becomes an important limiting factor if the electrode thickness is reduced from $100\ \mu\text{m}$ to $20\ \mu\text{m}$. For the $20\ \mu\text{m}$ thin layer electrodes a dominant (fractal) Gerischer type response was observed in the electrode dispersion. The high frequency ‘cut-off’ resistance showed a significant dependence on $p\text{O}_2$, similar to that found for the electronic conductivity. This effect could be ascribed to a limiting sheet resistance of the electrodes.*

* This chapter has been published in: *Fuel Cells*, **1**, No. 3-4, 256-264 (2001)

4.1 Introduction

The currently used material for anodes in SOFCs is a porous Ni/YSZ cermet that is optimised for the oxidation of hydrogen, but it presents some problems that have to be overcome in order to achieve the best cell performance. The nickel metal in the cermet tends to agglomerate after prolonged operation time leading to a reduced three-phase-boundary and an increasing resistance. The use of humidified natural gas can cause carbon deposition on the anode and poisoning by sulphur, finally resulting in a breakdown of cell performance. Hence, there is a great interest in finding new materials that avoid these drawbacks. But these prospective materials must also fulfil a series of stringent requirements, i.e.,

- thermodynamic stability under reducing conditions,
- sufficient catalytic activity for hydrogen or methane oxidation,
- high electronic and ionic conductivity,
- thermal expansion coefficients (TECs) which are compatible to other cell components,
- no adverse chemical reactions with the electrolyte or interconnect for prolonged operation times at high temperatures and in reducing atmospheres.

In this study several perovskite materials have been synthesised and tested as porous ceramic electrodes on yttria-stabilised zirconia (YSZ) electrolyte. The prospective electrode properties as SOFC anodes were tested in a controlled hydrogen/steam atmosphere. Combinations (solid solutions) in the lanthanum chromite - calcium or strontium titanate system have been tested as electrode material. The alkaline-earth containing LaCrO_3 end-member is already being applied as interconnect in SOFC stacks. All these mixed conducting oxide materials have TEC values which are close to the TEC of YSZ. This can be regarded as a major prerequisite for use as SOFC electrode. The electrical and ionic (defect) properties of these materials can be influenced by appropriate substitution on the lanthanum/calcium sites (sites A) and on

the chromium/titanium sites (sites B). In this work the ratio Cr/Ti has been varied, resulting in a transition from a *p*-type to an *n*-type conductor.

The relation between the composition and the electrode properties have been studied by Electrochemical Impedance Spectroscopy (EIS) in a three-electrode arrangement using a single-chamber cell.

4.2 Experimental

4.2.1 Sample preparation

The perovskite materials were synthesised using the Pechini method [1]. Nitrates, carbonates and oxides of the metals were complexed in an aqueous solution with citric acid and subsequently heated with ethylene glycol. After polyesterification and removal of the excess liquid, a resin was formed, which was first heated up to 300°C to decompose the organic constituents. Subsequently the product was ground in a mortar and finally calcined at 900°C to produce the perovskite powder.

X-ray diffraction (XRD, Siemens D 5000, Cu-K α) was carried out both on calcined powders and powders obtained after sintering and subsequent grinding. The thermal expansion coefficients (TEC) of the pressed and sintered bars were measured between 30 and 1000°C using a Netzsch DIL 402E pushrod dilatometer and applying a constant heating rate of 3°C/min up to either 1000°C or 1200°C. The particle size distribution of the obtained powders was measured with a Shimadzu Centrifugal Particle Size Analyser (SA-CP3). The different compositions, which have been prepared, are presented in Table 4.1.

For conductivity measurements the calcined powders were pressed uniaxially at 125 MPa into bars with dimensions of 2×4×20 mm³. These were sintered in air at 1400°C for 10 h. Temperature dependent conductivity measurements were carried out using a four-point method with collinear and equidistant Au contacts. The *p*O₂ dependence of the conductivity was established using a range of N₂/H₂/H₂O mixtures. The conductivity was calculated according to [2]:

$$\sigma_e = \frac{1}{2\pi \cdot s} \frac{I_{14}}{V_{23}} \cdot f \quad (4.1)$$

where I_{14} is the current applied to the outermost electrodes and V_{23} the voltage measured between probes 2 and 3. s is the distance between the latter two probes. The investigated samples could not be considered to be semi-infinite, hence a factor, f [2], was used which depends on the ratio between sample dimensions and inter probe distance, s .

Code	Composition	TEC×10 ⁶ [K ⁻¹]	Crystal structure	lattice parameters [Å]	Remarks ^(*)
LCCT-7382	La _{0.7} Ca _{0.3} Cr _{0.8} Ti _{0.2} O ₃	10.4	ortho-rhombic	a=5.4643 b=5.4755 c=7.7309	
LCCT-7328	La _{0.7} Ca _{0.3} Cr _{0.2} Ti _{0.8} O ₃	11.5		not determined (poor crystallization)	La ₄ Ca ₂ Ti ₅ O ₁₈ , La ₄ CaTi ₅ O ₁₇
LSCT-7382	La _{0.7} Sr _{0.3} Cr _{0.8} Ti _{0.2} O ₃	10.4	hexagonal	a=5.5047 c=13.3504	

Table 4.1: Name code, chemical composition, thermal expansion coefficient between room temperature and 1000°C and crystallographic properties of selected powders after sintering at 1400°C. For the TEC measurements sintered bars were used.

(*) Small amounts of additional phases according to JCPDS database

4.2.2 Preparation and characterisation of electrodes

For impedance measurements thick (100 μm) and thin (~20 μm) perovskite electrodes were screen-printed on YSZ discs (Tosoh, TZ-8Y) of 4 mm thickness and 16 mm diameter (see Figure 4.1). The electrodes were sintered for 5 h at 1225°C or 1300°C. It turned out to be rather difficult to reproducibly obtain crack free, 100 μm thick electrode layers of these perovskite materials. Hence the influence on electrochemical properties for a reduction to 20 μm was investigated as well.

A platinum counter electrode (same size as the perovskite working electrode, Ø 10 mm) was painted at the opposite side of the perovskite electrode using a Pt paste. A thin Pt wire, wrapped around in a small groove at half thickness of the cylindrical pellet, served as reference electrode (see Figure 4.1). This ring electrode was also painted with Pt paste in order to improve the electrical contact with the YSZ pellet.

The Pt electrodes were burnt in at 1000°C (1 h, heating rate 2°C/min) in a 4% H₂ in N₂ atmosphere.

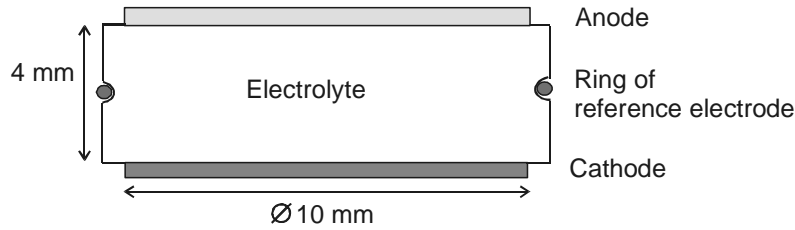


Figure 4.1: Schematic cut of the three-electrode electrochemical cell. The reference electrode is placed in the groove in the middle part of the electrolyte.

Impedance measurements were carried out in the frequency range from 0.01 Hz to 1 MHz (100 kHz in some cases) in a single-gas environment using a Solartron Frequency Response Analyser 1255 in combination with a Solartron Electrochemical Interface 1287. An excitation voltage with amplitude of 10 mV was used to ensure that the measurements were performed in the linear regime. No bias voltage was applied. Measurements with hydrogen as a fuel gas were performed at different temperatures in the range 700°C to 850°C and with different fuel gas concentrations. Nitrogen (99.999%) was used as a balancing gas in all the experiments.

The standard H₂/N₂ gas stream was moisturised to a level of 2.3% H₂O, using a temperature controlled double water-bubbler system. For $p_{\text{H}_2\text{O}}$ dependent measurements the hydrogen content was set at 80%. The water vapour content was controlled by adjusting the temperature of the water-bubblers. The nitrogen flow was adjusted to balance the overall flow to 100%. The used gas mixtures are presented in the figures. The bulk properties of the perovskite electrodes are directly related to the p_{O_2} , hence these properties are presented with respect to the calculated equilibrium value, obtained from the preset p_{H_2} and $p_{\text{H}_2\text{O}}$ values.

The impedance data were checked on validity using a Kramers-Kronig transformation test programme [3]. The data sets were analysed and modelled with a CNLS-fit programme [4,5]

4.2.3 Characterisation of the electrode microstructure

The interface of the YSZ/electrode was investigated by means of a JEOL JSM-5800 SEM (Scanning Electron Microscopy). Micrographs were taken before and after electrochemical experiments.

4.3 Results

4.3.1 Characterisation of the materials (XRD, particle size, TEC)

The XRD of the LCCT-7382 and LSCT-7382 revealed a single-phase perovskite material with orthorhombic and hexagonal lattice, respectively [6] (see Table 4.1). In the case of the LCCT-7328, minor phases of $\text{La}_4\text{Ca}_2\text{Ti}_5\text{O}_{18}$ and $\text{La}_4\text{CaTi}_5\text{O}_{17}$ were detected. The particle size distribution of the calcined powders was in the 0.3 to 3 μm range. Values of the TEC data for different compositions of the perovskite and results of the XRD measurements are also given in Table 4.1. Compounds with 80% chromium have a TEC very close to that of YSZ, $(10.6\text{-}11.0)\times 10^{-6} \text{ K}^{-1}$ [7].

4.3.2 Microstructure

The LSCT-7382 electrode was sintered on the surface of the YSZ pellet at 1225°C. Before and after the electrochemical measurements the electrode/electrolyte interface of a sample was investigated by SEM. The electrode showed a porosity of about 50%, the grain size of the perovskite particles was mainly around 1 μm . Hence, it was concluded that the particle size did not increase during the sintering step.

To characterise the contact region between electrolyte and electrode, the electrode was removed with concentrated nitric acid and ultrasonic treatment. Figure 4.2 (b) shows the micrograph of the electrode area after removal. The observed roughness indicates an intimate contact between the electrode and the electrolyte. The origin of this roughness is not clear, but it has also been observed for electrode structures directly after the sintering process. The electrochemical measurements or the acid dissolution treatment did not influence the surface structure of the not-covered YSZ

electrolyte area, as can be seen in Figure 4.2 (a). For a proper insight into this effect further elemental surface analysis would be desirable.

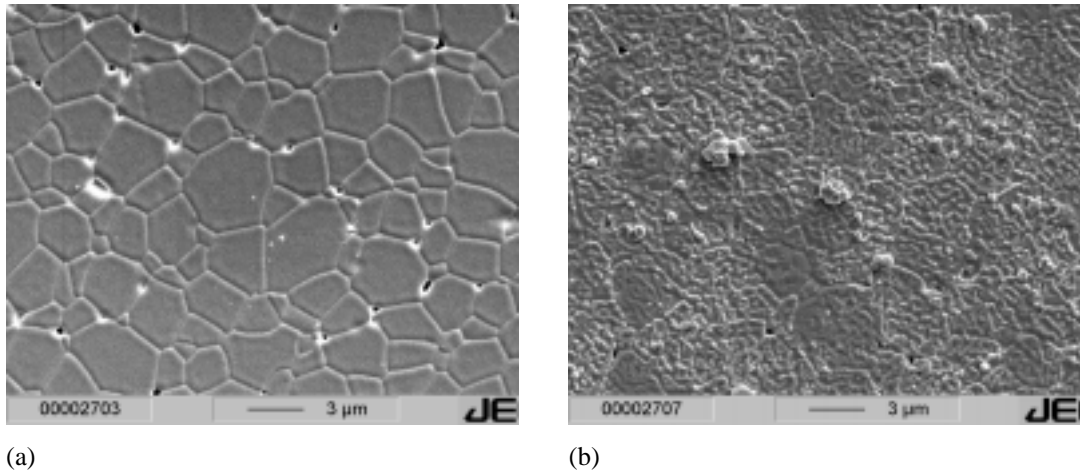


Figure 4.2: SEM micrographs of a LSCT sample after removal of the electrode with HNO_3 and ultrasonic cleaning. (a): free electrolyte surface outside the geometric electrode area. (b): electrolyte surface originally covered with the LSCT-7382 electrode.

4.3.3 *Electronic conductivity*

The electronic conductivity of perovskite samples was investigated as a function of the $p\text{O}_2$ (especially in the low $p\text{O}_2$ range) at temperatures between 700°C and 850°C , i.e. under the same conditions as the electrochemical investigation on the electrodes (see Figure 4.3). For both the LCCT-7328 and the LSCT-7328 n-type electronic conductivity was found in the low $p\text{O}_2$ range with values of about 0.1 S/cm at 850°C and 10^{-20} bar $p\text{O}_2$. The calcium doped lanthanum titanate without Cr is reported to exhibit n-type electronic conductivity [8]. Thus for a composition with 80% Ti on the B-site, this n-type behaviour may also be expected.

For the LCCT-7382 a much lower electronic conductivity ($\sim 10^{-4} \text{ S/cm}$) was found in the low $p\text{O}_2$ range. This compound exhibited p-type conduction behaviour in this $p\text{O}_2$ range, as is also reported for the pure chromite, LCC [9-11].

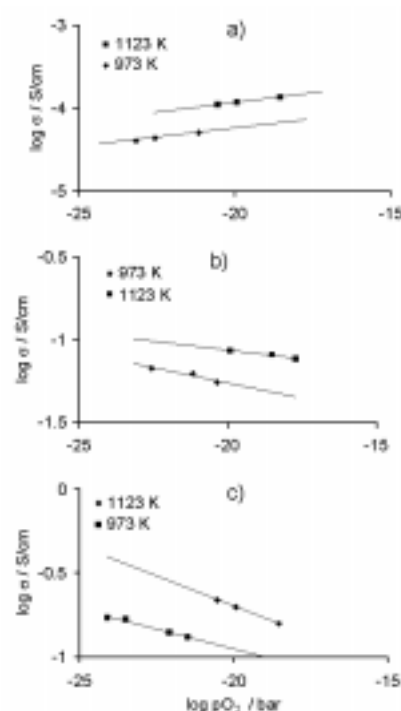


Figure 4.3: Electronic conductivity of a) LCCT-7382, b) LCCT-7328 and c) LSCT-7328 as function of the pO_2 at 700°C and 850°C. Lines serve as a guide to the eye.

4.3.4 Electrode response of thick electrodes

Both ceramic electrodes (LSCT-7382 and LCCT-7328, approximately 100 μm thick) showed an electrode dispersion in the impedance representation that resembles a depressed and somewhat skewed semi-circle (see Figures 4.4 and 4.5).

Visual inspection of the impedance diagrams indicates a single semi-circle response. Careful analysis using a CNLS-fit procedure clearly indicates that at least two (distributed) time constants are present, i.e. two depressed semi-circles. Hence, the analysis of the major part of the dispersion was carried out with a simple $R_{el}(R_1Q_1)(R_2Q_2)$ circuit, which gave a more than ten-fold improvement in the χ^2_{fit} -value over a single semi-circle. Here the ‘Circuit Description Code’ developed by Boukamp [5] is used. The constant phase element (CPE, denoted by Q) is defined in

the admittance representation as [5]: $Y(\omega) = Y_0 \times (j\omega)^n$. R_{el} is related to the electrolyte resistance. The (R_1Q_1) part represents the high frequency semi-circular dispersion and (R_2Q_2) the low frequency arc.

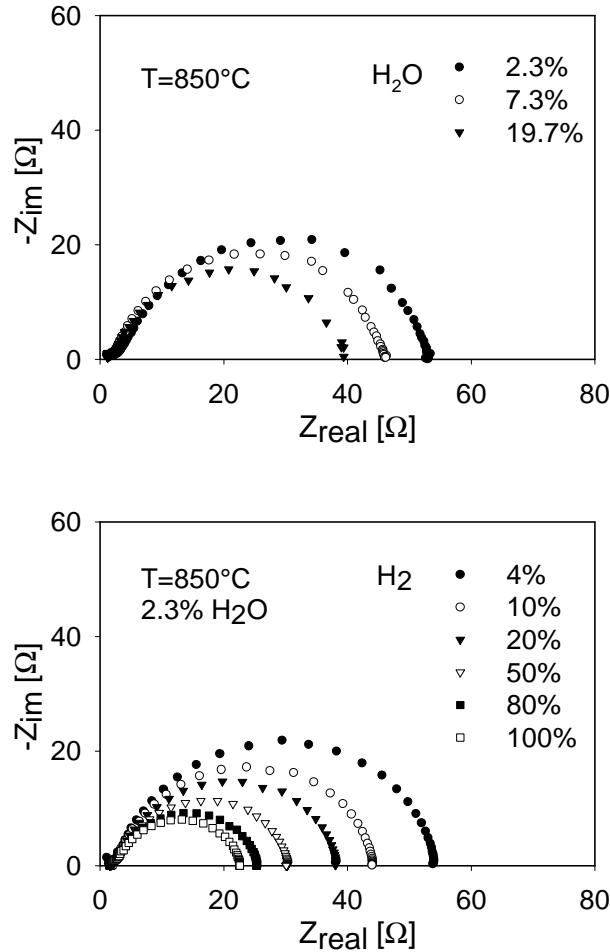


Figure 4.4: Partial pressure dependence of the electrode impedance of a 100 μm thick LCCT-7328 anode; above as $f(p\text{H}_2\text{O})$, below as $f(p\text{H}_2)$.

The activation energy of the overall electrode dispersion (polarisation resistance) was measured in the temperature range of 700 to 850°C in an atmosphere of 4% H₂ and 2.3% H₂O with N₂ as balancing gas. The *n*-type LCCT-7328 electrode showed the

highest activation energy, i.e. $130 \pm 5 \text{ kJ}\cdot\text{mol}^{-1}$. For the *p*-type LSCT-7382 this was somewhat lower, i.e. $86 \pm 1 \text{ kJ}\cdot\text{mol}^{-1}$.

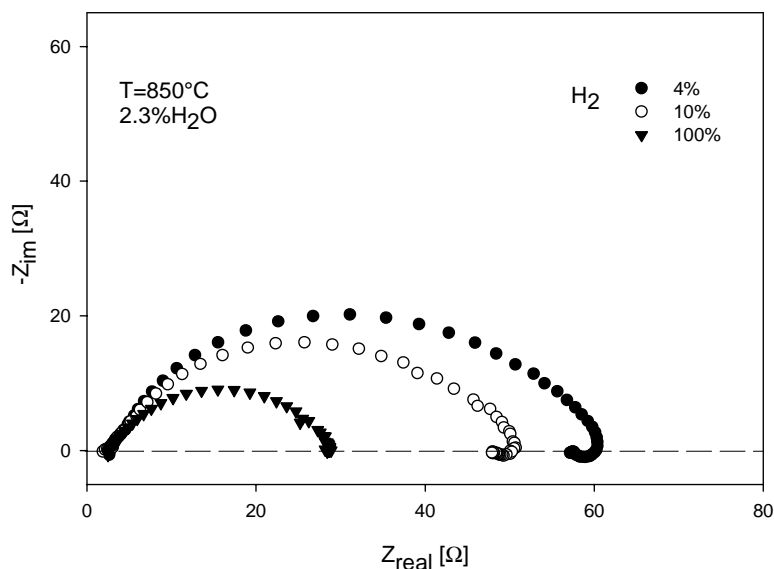


Figure 4.5: Hydrogen partial pressure dependence of electrode impedance for a 100 μm thick LSCT-7382 anode.

The dependence of the electrode dispersion on the hydrogen partial pressure was studied at 850°C with a 2.3% H_2O background pressure and N_2 as balancing gas. Both electrodes showed a clear decrease in the electrode polarisation resistance with increasing $p\text{H}_2$, as can be seen in Figures 4.4 and 4.5. The $p\text{H}_2\text{O}$ dependence was determined similarly in 80% H_2 with N_2 as the balancing gas. For the LCCT-7328 this dependence is presented also in Figure 4.4. From these measurements the $p\text{H}_2$ and $p\text{H}_2\text{O}$ power dependence was established for the circuit elements R_1 , Q_1 and R_2 , Q_2 . In order to facilitate comparison between the circuit parameters the resistance is presented as a conductance (admittance form: $\sigma_i = R_i^{-1}$). Hence the power dependence, m , is presented as: $\sigma_i, Q_i - Y_0 \propto (p\text{H}_2)^m$ or $(p\text{H}_2\text{O})^m$. The largest dependence was found for the low frequency Q_2 -element of the LSCT-7382 electrode with $m_{\text{H}_2} = 0.28$ and $m_{\text{H}_2\text{O}} = -0.58$. The Q -elements of the LCCT-7328 electrode were independent of both $p\text{H}_2$ and $p\text{H}_2\text{O}$. All values for m are presented in Table 4.2.

Composition:		LSCT-7382 (Fig. 4.5 data)		LCCT-7328 (Fig. 4.4 data)	
$R^{-1}, Q \propto (pX)^m$:		$m(pH_2)$	$m(pH_2O)$	$m(pH_2)$	$m(pH_2O)$
$\sigma_1 = (R_1)^{-1}$	(hf)	+0.08	+0.23	+0.19	--
Q_1-Y_0	(hf)	+0.13	--	--	--
$\sigma_2 = (R_2)^{-1}$	(lf)	+0.21	-0.1	+0.28	+0.15
Q_2-Y_0	(lf)	+0.28	-0.58	--	--

Table 4.2: Values for the partial pressure power dependence m of the circuit elements, obtained from pH_2 and pH_2O dependent impedance measurements. hf = high frequency arc, lf = low frequency arc. The resistances are presented as conductances.

The corresponding, approximate capacitance values are derived from the summit frequencies of the separate (RQ) arc dispersions, using $R \cdot C \cdot 2\pi f_{\text{summit}} = 1$. These capacitances are quite large, about 15 μF and 30 μF for the LSCT-7382 electrode (Q_1 and Q_2 , respectively), and 10 μF and 60 μF for the LCCT-7328 electrode.

As expected, the electrolyte resistance, R_{el} was independent of the H_2 or H_2O partial pressure with an activation energy of 60 kJ/mol. No influence of the electrode composition was observed. The apparent inductive loop at the low frequency end, observed for LSCT7382 (Figure 4.5), must be interpreted as a *negative differential* capacitance parallel to a *negative differential* resistance. The origin of this effect is not yet clear, although it has also been observed for SOFC anodes by other authors as well [12-13].

4.3.5 Thin electrodes

The electrode dispersions of the 20 μm thin electrodes (compositions LCCT-7382 and LCCT-7328) were quite different from those of the 100 μm thick electrodes (see

Figure 4.6 and Figures 4.4 and 4.5), although they showed the same trends with respect to the $p\text{H}_2$ and $p\text{H}_2\text{O}$ dependencies.

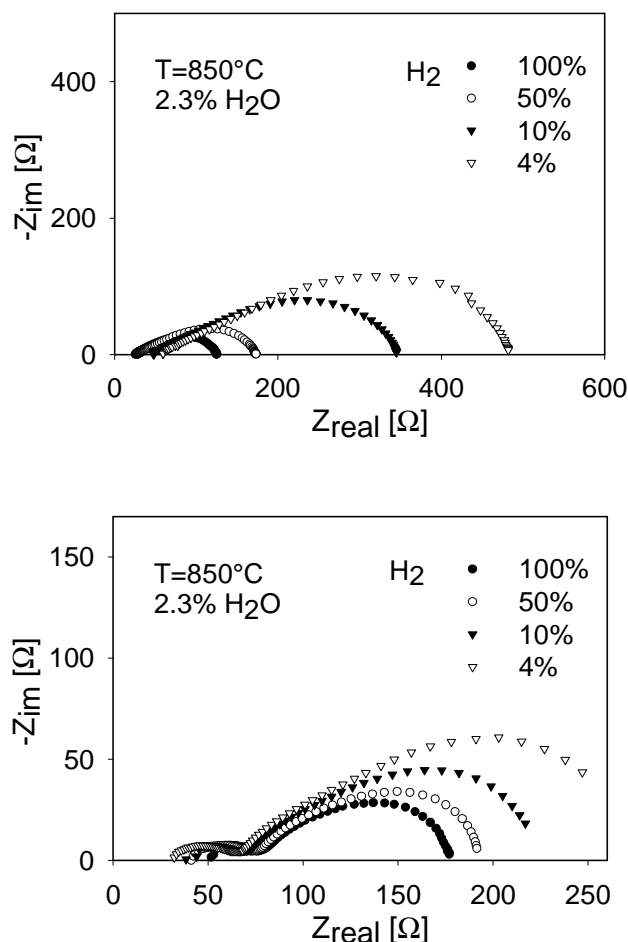


Figure 4.6: Impedance spectra of the 20 μm thick n-type LCCT-7328 (top) and p-type LCCT-7382 (bottom) anode, at 850°C for different hydrogen contents in the fuel gas.

A major difference is the rather large ‘high frequency cut-off’ resistance, $R_{\text{cut-off}}$, which normally is determined by the electrolyte resistance, R_{el} . The value of R_{el} should depend only on the 3-electrode geometry. It is, in principle, independent of $p\text{H}_2$ and $p\text{H}_2\text{O}$, as is the case for the thick electrodes. For the n-type LCCT-7328 electrode this resistance decreases with decreasing $p\text{O}_2$ with $R_{\text{cut-off}} \div (p\text{O}_2)^{0.08}$ (i.e. increasing $p\text{H}_2$ or decreasing $p\text{H}_2\text{O}$). For the p-type LCCT-7382 electrode $R_{\text{cut-off}}$ increases with decreasing $p\text{O}_2$, $R_{\text{cut-off}} \div (p\text{O}_2)^{-0.04}$. In Figure 4.7 these resistances are presented as conductivities in order to show the relation with the $p\text{O}_2$ dependence of

the electronic conductivity of these compositions, which have been presented in Figures 4.3 a) and 4.3 b).

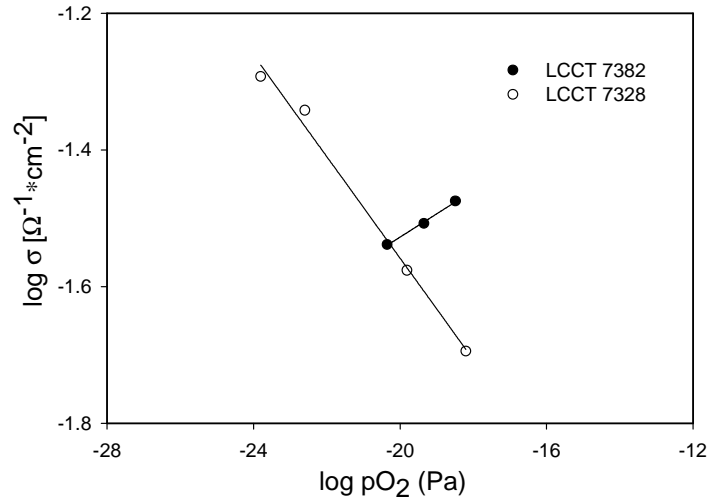


Figure 4.7: Sheet conductivity of the 20 μm thick n-type LCCT-7328 and p-type LCCT-7382 anodes as function of pO_2 . Lines serve as a guide to the eye.

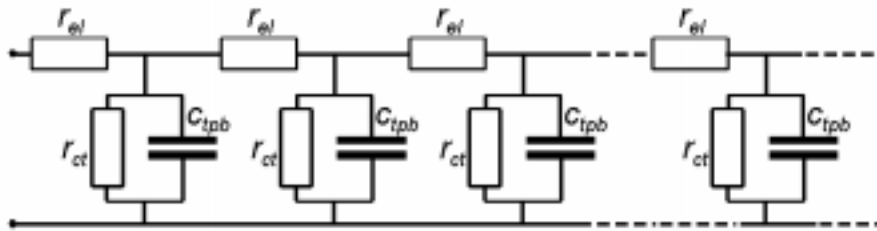


Figure 4.8: Transmission line model which leads to a Gerischer type impedance response:

$$Z(\omega) = \sqrt{\frac{r_{el}}{C_{tpb}}} \cdot \left[\frac{1}{r_{ct} \cdot C_{tpb}} + j\omega \right]^{-0.5} . \text{ With: } r_{el} \text{ electronic spreading resistance of the electrode, } r_{ct} \text{ charge transfer resistance, } C_{tpb} \text{ electrochemical capacitance at the TPB.}$$

The observed behaviour of $R_{cut-off}$ for both types of electrodes points to a limitation by the electronic conductivity in the high frequency regime. This is in accordance with the observed pO_2 dependence for the p - and n -type conductivities of the LCCT-7382 and the LCCT-7328 electrode materials, respectively. Most likely the ‘sheet resistance’ of the thin electrodes is too high to be ignored.

A further difference, with respect to the impedances of the thick electrodes, is the shape of the dispersion (Figure 4.6). The CNLS-analysis indicates that the low frequency dispersion has the form of a Gerischer impedance [14]. It could be modelled quite reasonably by a ‘fractal’ modification of the Gerischer expression:

$$Z = Z_0 (k + j\omega)^{-\alpha} \quad (4.2)$$

The value of α was about 0.35 and, within experimental error, temperature independent.

The standard Gerischer element, with $\alpha = 1/2$, can be modelled by a transmission line model with a ‘leaky’ capacitance, as schematically presented in Figure 4.8, i.e.,

$$Z_G(\omega) = \sqrt{\frac{r_{el}}{c_{tpb}}} \cdot \left[\frac{1}{r_{ct} \cdot c_{tpb}} + j\omega \right]^{-0.5} \quad (4.3)$$

A much improved modelling of the low frequency end of the data could be obtained through the use of a ‘double fractal’ Gerischer expression:

$$Z_{d-fr} = Z_0 \left[k + (j\omega)^\beta \right]^{-\alpha} \quad (4.4)$$

where β is less than one (this dispersion relation has the same form as the phenomenological Havriliak-Negami dielectric dispersion relation [15]). An example of the CNLS-modelling of the LCCT-7328 with both modified Gerischer expressions is presented in Figure 4.9. The residuals plots (inserts in Figure 4.9) clearly indicate the significant improvement using the ‘double fractal’ Gerischer expression.

For the data analysis the single fractal Gerischer expression, equation (4.2), was used, as it is readily available in the modified version of ‘Equivalent Circuit’ [16]. The small arc in the high frequency range was modelled with an additional (RQ). For both electrodes, the same pO_2 dependency of the ‘rate constant’, k , was found with a value of -0.35 . For the LCCT-7328 a pO_2 dependence of 0.15 was found for the resistance $R_{cut-off}$, the Gerischer element G ($= Z_0^{-1}$) showed a dependence of -0.10 . In the case of the LCCT-7382 only k showed a pO_2 dependence of -0.35 , the other parameters values were independent of the oxygen partial pressure.

Arrhenius plots of the equivalent circuit elements of the LCCT-7328 are shown in Figure 4.10; the activation energies of the equivalent circuit elements are given in Table 4.3.

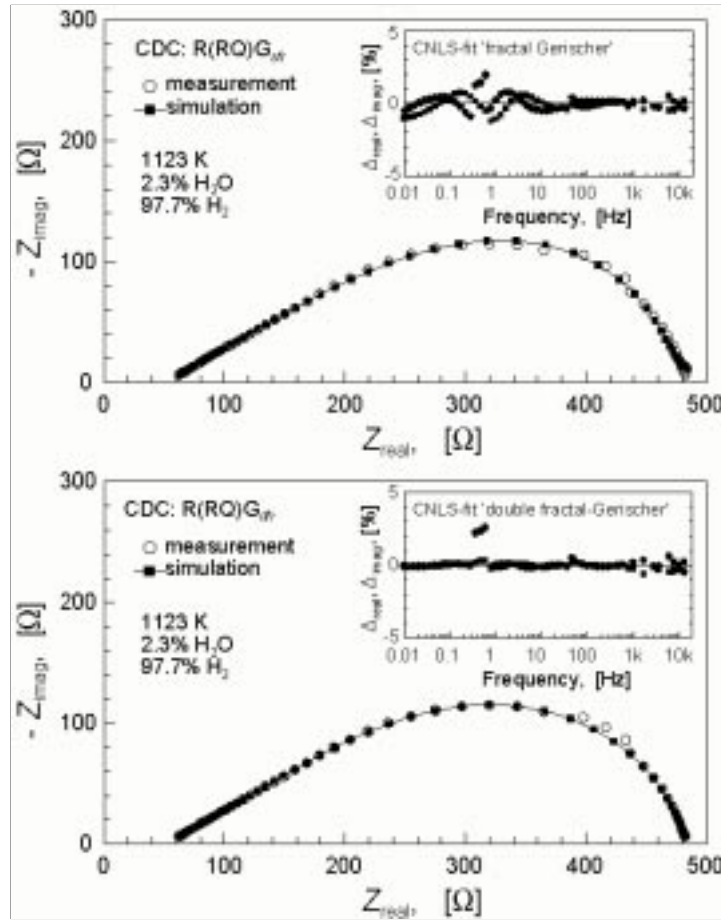


Figure 4.9: CNLS-fit of electrode dispersion for 20 μm thick LCCT-7328 with a ‘single fractal Gerischer’ (G_{sfr}) and a ‘double fractal’ Gerischer. The residual plots are presented in the insert.

The resistance, $R_{\text{cut-off}}$, is due to electronic conductivity of the electrode (neglecting the much smaller electrolyte resistance), therefore the activation energy of this resistance is reflecting the activation energy of the electronic conductivity. With 76 $\text{kJ}\cdot\text{mol}^{-1}$ this value is close to the 66 $\text{kJ}\cdot\text{mol}^{-1}$ found for the electronic conductivity with the four-probe technique (see above).

The stability and reproducibility of the electrodes was checked using the 20 μm thin electrodes. No major degradation was observed after 72 h at 850°C under reducing

conditions. To test the reproducibility of the electrode preparation method, two samples of the LCCT-7328 composition were compared.

The electrode impedances measured at 850°C in moisturised hydrogen were nearly identical in shape and magnitude, as can be seen from Figure 4.11.

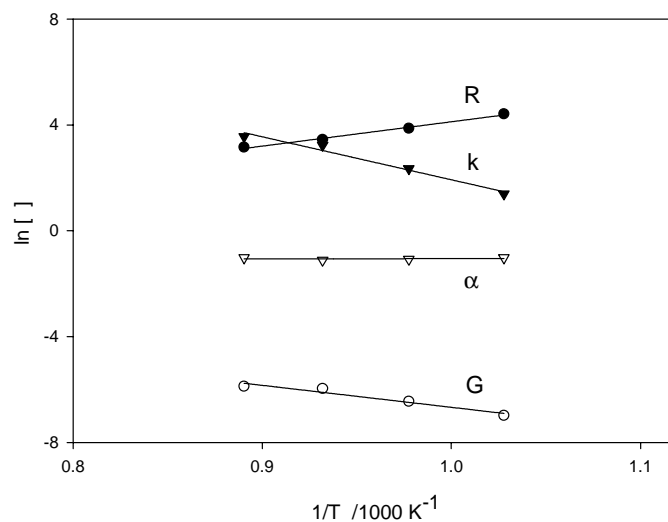


Figure 4.10: Arrhenius plots of the equivalent circuit elements of the 20 μm thick LCCT-7328.

	$R_{\text{cut-off}}$	$G-Z_0$	k	α
E_A [kJ/mol]	76	-69	-135	-

Table 4.3: Activation energies of the equivalent circuit elements for the LCCT-7328 (Figure 4.6 data).

4.4 Discussion

The electrode impedance for the 100 μm thick electrodes is much larger than for the optimised Ni/YSZ cermet anodes [17]. From the observed impedance spectra it is not possible to elucidate a detailed model for the electrode reaction. Several processes may be responsible for the shape and magnitude of the electrode dispersion, e.g., adsorption-dissociation of H_2 and H_2O on the ceramic surface, reaction with (sub-) surface oxygen of the perovskite and diffusion to a triple phase boundary area at the YSZ/electrode interface.

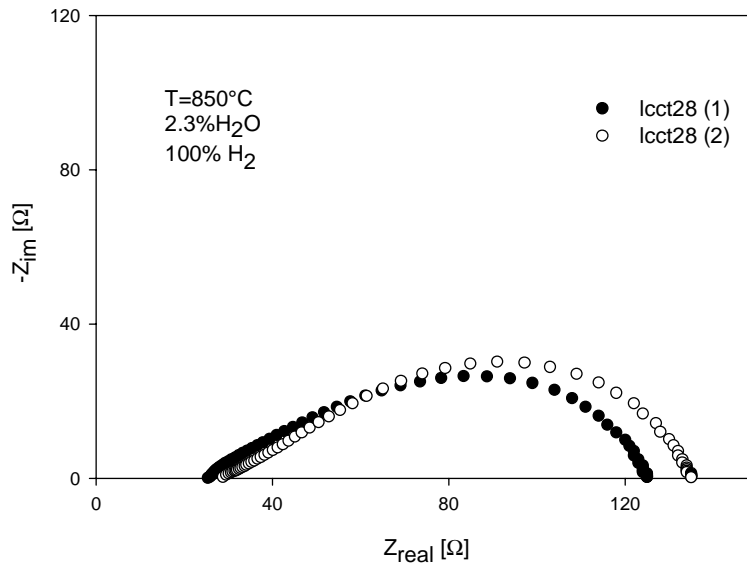


Figure 4.11: Reproducibility of 20 μm thick LCCT-7328 anodes.

The porous electrode is a largely distributed system of electronic, ionic and gaseous pathways. Yet the impedance spectra seem to indicate that adsorption/desorption and reaction is more dominant as rate controlling step than diffusion. In the latter case CPE's with values for n (in $Q: Y(\omega) = Y_0 \times (j\omega)^n$) less than 0.5 should have been observed. Here the n -values are closer to 1, indicating (distributed-) capacitive behaviour. A rough estimate of the electrode surface area (from grain size, density, porosity and macroscopic ceramic-electrode volume) indicates a *maximum* value for an adsorption capacitance of ~ 500 mF. For this a Langmuir-type adsorption of H_2 and/or H_2O is assumed. But it is very likely that only a small region near the triple phase boundary line will be electrochemically active, hence much lower values may be expected. Another possibility is the '*chemical capacitance*' associated with the oxygen non-stoichiometry of the perovskites. It is easy to show that such a capacitance could reach a value of 500 F, in case the entire electrode layer is electrochemically active and assuming a thermodynamic enhancement factor of 1. Thus, the observed (comparable) capacitance values of ~ 10 -50 μF could quite well be due to adsorption. The $p\text{H}_2$ and $p\text{H}_2\text{O}$ independent Q -values for the n -type LCCT-7328 electrode (Table 4.2) could then be explained tentatively by saturation of the

adsorption sites. Unfortunately, the electrode reaction is too complex to allow a simple interpretation based on the observed pH_2 and pH_2O dependencies.

The occurrence of a Gerischer impedance in the thin electrodes is more difficult to explain. This is especially true for the high frequency resistance, which for the thick electrodes just represents the ‘non-faradaic’ electrolyte resistance. A possible interpretation can be based on a transmission line model.

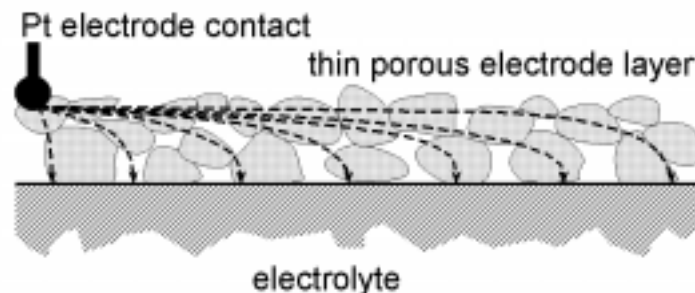


Figure 4.12: Cartoon of the current lines emanating from a single Pt-electrode contact in a thin porous electrode layer.

For very thin electrode layers the lateral electrode resistance can add a significant contribution to the overall electrode impedance. This is depicted in the cartoon of Figure 4.12.

The current density will decrease with distance from the Pt contact point, which represents the electrical connection between the Pt grid and the ceramic electrode. The electrode impedance can be modelled in a qualitative way using a semi-infinite transmission line model. Assuming a complex semi-infinite transmission line with a specific impedance, Z_x , per unit length and a parallel conductance (admittance), of Y_y , per unit length, the overall impedance can be written as [18]:

$$Z(\omega) = \sqrt{\frac{Z_x}{Y_y}} \quad (4.5)$$

With $Z_x = r_x \Omega/\text{cm}$ and $Y_y = j\omega c_y \text{ S}/\text{cm}$, the simple Warburg expression (semi-infinite diffusion) is obtained.

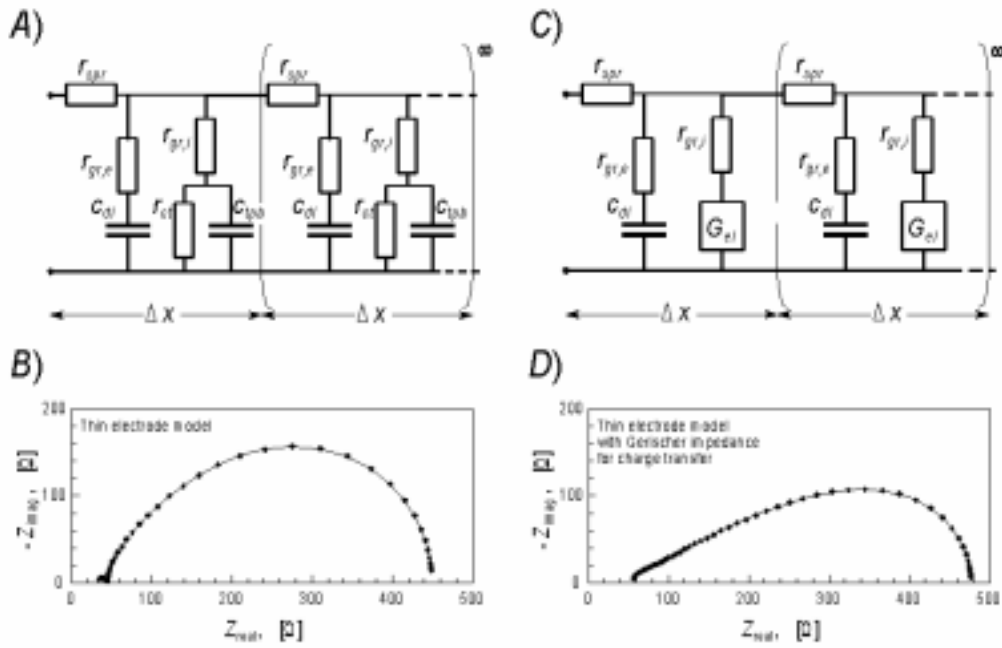


Figure 4.13: Simple one dimensional transmission line type modelling of the distributed electrode of the thin layer anodes. **A)** Model with high frequency ($R_{el}C_{dl}$) and electrochemical low frequency branches. **B)** Simulation of the model **A** dispersion (Table 4.4, see text for details). **C)** Modified model with distributed electrochemical branch, presented by a Gerischer impedance. **D)** Simulation of the model **C** dispersion (Table 4.4). r_{spr} : lateral electronic resistance [Ω], $r_{gr,e}$: electronic grain resistance [Ωcm], c_{dl} : double layer capacitance [F/cm], r_{ct} : charge transfer resistance [Ωcm], c_{tpb} : triple phase boundary capacitance [F/cm], $r_{gr,i}$: electronic grain resistance of the ionic current branch [Ωcm]. G_{el} distributed response at the TPB.

This one dimensional, general expression can be used to model the electrode impedance of a thin porous electrode. In the construction of the model one must include also the non-Faradaic (electronic) conduction, which becomes important at higher frequencies. This contribution is presented in Figure 4.13A by the $r_{gr,e} - c_{dl}$ branches. The lateral resistance is given by the ‘spreading resistance’ r_{spr} . The electronic conductance perpendicular to the electrolyte interface is given by $r_{gr,e}$,

which of course is just another representation of the electronic conductivity of the grains. c_{dl} represents the electronic/ionic double layer capacitance between the electrode grains and the electrolyte.

The second branch in Figure 4.13A signifies the electrochemical reactions. The charge transfer resistance is given by r_{ct} , while the capacitance, c_{tpb} models the (electrochemical) double layer-adsorption capacitance at, or near, the triple phase boundary. The combined electronic-ionic resistance for this electrochemical branch is represented by $r_{gr,i}$. A lower case symbol is used for all circuit elements to express that these are ‘specific’ impedances. To make the model more realistic one may assume a ‘width’ of 1 cm for the electrode, thus retaining the one-dimensionality while the parameters are expressed in unit/cm² or unit·cm². This then allows the use of realistic values for the various parameters.

The repeat unit for a length Δx is indicated in Figure 4.13 by the circuit between the parenthesis. For the limit $\Delta x \rightarrow 0$ the following expression for the model impedance is obtained:

$$Z(\omega) = \sqrt{\frac{r_{spr}}{Y_{gr,e} + Y_{ct}}} \quad (4.6)$$

with:

$$Y_{gr,e} = \frac{1}{r_{gr,e}} \cdot \frac{1 + j\omega r_{gr,e} c_{dl}}{1 + (\omega r_{gr,e} c_{dl})^2} \quad (4.7)$$

and:

$$Y_{ct} = \left[r_{gr,i} + r_{ct} \frac{1 - j\omega r_{ct} c_{tpb}}{1 + (\omega r_{ct} c_{tpb})^2} \right]^{-1} \quad (4.8)$$

Equation (4.6) shows two competitive parallel branches. If we assume that for increasing frequencies the parallel electronic branch will dominate we obtain a simplified formula:

$$Z(\omega)_{\omega \rightarrow \infty} \approx \sqrt{\frac{r_{\text{spr}}}{Y_{\text{gr, e}}}} \approx \sqrt{r_{\text{spr}} \cdot r_{\text{gr, e}} \div R_{\text{cl}}} \quad (4.9)$$

This is an important step as it shows how the extra high frequency resistance is obtained, *and* that this resistance is directly proportional to the electronic resistance of the electrode layer. Hence, this resistance must dictate the $p\text{O}_2$ dependence of $R_{\text{cut-off}}$ in the thin electrodes.

Modelling the measured impedance with the equation set (4.6-4.8), as depicted in Figure 4.13B, does not yield a good comparison with the measured thin electrode response. This is hardly surprising, since this one-dimensional model is far too simplistic. The current path, schematically presented in Figure 4.12, should also be subjected to a kind of distribution that is strongly related to the randomly positioned contact points with the Pt gauze. Furthermore, the ionic branch in Figure 4.13A might also be a distributed function. A simple modification is to replace the charge transfer resistance and the parallel capacitance in the ionic path by a Gerischer impedance, see Figure 4.13C. The model impedance, Figure 4.13D, now strongly resembles the measured electrode impedance. The input parameters for both modelling results are presented in Table 4.4.

Parameter	Model A	Model C	unit
r_{spr}	100	200	Ω
$r_{\text{gr,e}}$	20	50	$\Omega \cdot \text{cm}^2$
C_{dl}	$1.0 \cdot 10^{-6}$	$5.0 \cdot 10^{-6}$	F/cm^2
$r_{\text{gr,i}}$	20	20	$\Omega \cdot \text{cm}^2$
r_{ct}	2000	n.a.	$\Omega \cdot \text{cm}^2$
C_{tpb}	$5.0 \cdot 10^{-4}$	n.a.	F/cm^2
$G: Z_0$	n.a.	500	$\Omega \cdot \text{cm}^2$
$G: k$	n.a.	0.2	s^{-1}

Table 4.4: Parameter values used in the simulation of the thin layer electrode impedance of Figures 13A-B and 13C-D.

The model for the interpretation of the Gerischer impedance, presented here, differs significantly from the model presented by Adler [19] for a porous perovskite type cathode. The Gerischer impedance derived by Adler is based on the combined surface oxygen exchange process, coupled with the bulk diffusion in the electrode structure. This implies that, in our case, the Gerischer impedance should also have been observed for the thick electrodes, which is not the case.

4.5 Conclusions

The perovskite electrodes are electrochemically active towards hydrogen oxidation, although the electronic conductivity is not sufficient if thin electrodes (20 μm layer thickness) have to be prepared for SOFC. The total electrode resistance of the electrodes was about a factor 10 higher than that of the-state-of-the-art SOFC anode Ni/YSZ.

The materials have been found to be stable under reducing conditions and measurements were reproducible with different samples of the same composition.

References

- [1] M.P. Pechini, US Patent 3, 697, 1967.
- [2] L.B. Valdes, Proc. IRE 42, 420-427, 1954.
- [3] B.A. Boukamp, J. Electrochem. Soc. 142, 1885-1894, 1995.
- [4] B.A. Boukamp, Solid State Ionics 18-19, 136-140, 1986.
- [5] B.A. Boukamp, Solid State Ionics 1986, 20, 31-44, 1986.
- [6] G. Pudmich, B.A. Boukamp, M. Gonzalez-Cuenca, W. Jungen, W. Zipprich and F. Tietz, Solid State Ionics 135-137, 433-438, 2000.
- [7] R. Männer, E. Ivers-Tiffée and W. Wersing, in: F. Grosz, P. Zegers, S.C. Singhal and O. Yamamoto Eds., SOFC II, Commission of the European Communities, Luxemburg, L. EUR-13564-EN. 715, 1991.
- [8] T. Inoue, N. Seki, J. Kamimae, K. Eguchi and H. Arai, Solid State Ionics 48, 283-288, 1991.
- [9] N.Q. Minh and T. Takahashi, Science and Technology of Ceramic Fuel Cells, Elsevier, 1995.
- [10] V.V. Kharton, A. Yaremchenko and E. Naumovich, J. Solid State Electrochem. 3, 303-326, 1999.
- [11] N. Sakai, J. Materials Science 25, 4531-4534, 1990.
- [12] B. de Boer, PhD Thesis, University of Twente, 1998.
- [13] A. Bieberle, PhD Thesis, ETH Zürich, 2000.

- [14] M. Sluyters-Rehbach and J.H. Sluyters, *Comprehensive Treatise of Electrochemistry* 9, Ed. E. Yeager Plenum, New York 274, 1984.
- [15] S. Havriliak and S. Negami, *Polymer* 8, 161, 1967.
- [16] B.A. Boukamp, *Equivalent Circuit, Users Manual*, Report CT89/214/128, University of Twente, 1989.
- [17] H. Koide, Y. Someya, T. Yoshida and T. Maruyama, *Solid State Ionics* 132, 253-260, 2000.
- [18] J. Ross Macdonald, *Impedance Spectroscopy*, WILEY, New York, 1987.
- [19] S. Adler, *Solid State Ionics* 111, 125-134, 1998.

Hydrogen oxidation on Ni/Y₂O₃-ZrO₂-TiO₂ cermet anodes

Hydrogen oxidation was studied for screen-printed cermet anodes composed of nickel metal and yttria-stabilised zirconia with additions of 5 and 10 mol% titania. Electrochemical impedance spectroscopy and current-overpotential measurements at 850°C were used to characterise the behaviour of the anodes. The impedance spectra at open circuit potential indicated the presence of three different processes dependent on the H₂/H₂O ratio and temperature. The measurements revealed a similar behaviour as functions of H₂ and H₂O partial pressures for the cermets with 5 and 10 mol% titania. The total electrode resistance increases with increasing the sintering temperature of the cermets from 1300°C to 1400°C. Contrary to earlier observations made for Ni/YSZ, the results showed that for the Ti-containing cermets the total electrode resistance decreases with time. It is clear that further research is necessary to evaluate their possible use as anode in SOFC applications.

5.1 Introduction

Cermets made of nickel and yttria-stabilised zirconia (YSZ) are the state-of-the-art anodes in the solid oxide fuel cell (SOFC). Although Ni/YSZ cermets are used worldwide in SOFC development, there are some inherent disadvantages. One is sulphur poisoning in the case where natural gas is used as fuel. Another is reduction of the catalytic activity during long-term operation at 900-1000°C [1]. This is due to the sintering activity of nickel, resulting in the coarsening of Ni particles and, therefore, a reduction of the extent of the triple phase boundary (TPB) length at which the reaction takes place.

To improve the performance of the Ni/YSZ cermets, the use of Ti-doped YSZ ceramics has been proposed [2-6]. Because of the mixed ionic-electronic conducting properties of $\text{Y}_2\text{O}_3\text{-ZrO}_2\text{-TiO}_2$ (YZT) ceramics, resulting from the additional electronic conductivity due to the $\text{Ti}^{4+} \rightarrow \text{Ti}^{3+}$ valence change under reducing conditions, it is expected that the electrocatalytic reaction would be enhanced due to a spreading of the reaction zone [7, 8]. The use of YZT in the cermets reduces the agglomeration of Ni particles during long-term operation, thus avoiding reduction of the TPB length with time [8-10]. Furthermore, the TiO_2 substitution results in a lowering of the TEC values of the cermets and, therefore, to an improved match with the electrolyte [10]. Due to the n-type electronic conductivity of the ceramic, it is possible to reduce the nickel content in the cermet.

We have started an experimental study to explore the possible use of Ni/YZT cermets as anode in SOFC applications. In this initial work, cermets were prepared from NiO and YSZ containing 5 and 10 mol% of titania. These were screen-printed and tested as anode in the hydrogen oxidation reaction. Impedance spectroscopy at various $\text{H}_2/\text{H}_2\text{O}$ ratios, bias potentials and temperatures, and $I\text{-}\eta$ measurements were employed in order to characterise their behaviour.

5.2 Experimental

5.2.1 Powder preparation

The YZT powders investigated were synthesised at the Forschungszentrum Jülich, Germany, by spray-drying of aqueous nitrate solutions according to the procedure as described in detail elsewhere [11]. The stock solution contained a nominal Y³⁺ content of 15 mol% and 85 mol% of Zr⁴⁺ leading to a ceramic of 8 mol% yttria-stabilised zirconia (8YSZ). Titania, either 5 or 10 mol%, was added to the yttrium- and zirconium-containing nitrate solution by the precipitation of titanium oxyhydroxides from a titanium trichloride hydrochloric solution with ammonia and subsequent dissolution of the fresh precipitate in dilute nitric acid. Assuming a complete dissolution of titanium ions in the fluorite lattice, the compounds resulting from the admixture of the titanium solution have a nominal composition of Y_{0.141}Zr_{0.809}Ti_{0.05}O_{1.93} and Y_{0.133}Zr_{0.767}Ti_{0.10}O_{1.93}. These compositions are termed hereafter as YSZ5Ti and YSZ10Ti, respectively. The two powders were calcined after spray-drying for 5 h at 900°C in air. Parts of the YZT powders were mixed with the appropriate amounts of NiO (J.T. Baker, >99%) to achieve nickel contents of 40 vol% after reduction of the NiO/YZT mixtures. The powder mixtures with NiO were wet milled with ethanol in a centrifugal ball mill for 120 h. Phase purity of the product was checked by powder X-ray diffraction.

5.2.2 Preparation of the electrochemical cell

The electrolyte consists of a YSZ disc (Tosoh, TZ-8Y) of 4 mm thickness and 16 mm diameter. The preparation procedure is described in Section 2.2.1 of this thesis.

The Ni/YZT cermet anode was screen-printed on the YSZ disc and sintered either at 1300°C or 1400°C for 3 h in air. Its thickness was ~20µm. The geometrical area was 0.78 cm². The cell geometry is shown schematically in Figure 5.1.

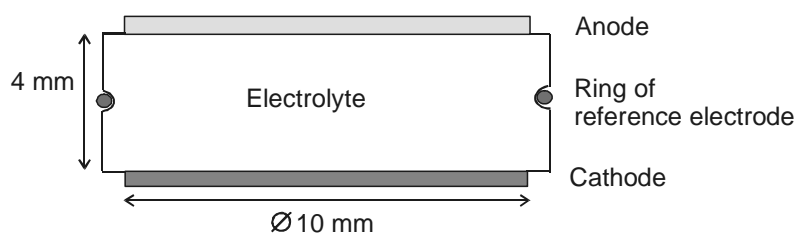


Figure 5.1: Schematic cut of the three-electrode electrochemical cell. The reference electrode is placed in the groove in the middle part of the electrolyte.

5.2.3 Electrochemical testing

Experiments were conducted in a single-chamber environment at atmospheric pressure with different $\text{H}_2/\text{H}_2\text{O}$ ratios. Nitrogen (99.999%) was used as a balancing gas in all experiments. The H_2/N_2 gas stream was moisturised, using a temperature controlled double water-bubbler system. The water vapour content was controlled through adjusting the temperature of the water-bubblers. At standard conditions a gas flow of 100 ml/min H_2 with 2.3% H_2O at 850°C was used.

Impedance measurements were carried out in the frequency range from 0.01 Hz to 1 MHz (100 kHz in some cases) using a Solartron Frequency Response Analyser 1255 in combination with a Solartron Electrochemical Interface 1287.

An excitation voltage with amplitude of 10 mV was used to ensure that the measurements were performed in the linear regime. Impedance measurements were carried out at open circuit potential in the $p\text{H}_2$ range from 9.98×10^4 to 4.95×10^3 Pa (or from 100% to 4% of H_2 content in the gas atmosphere) with $p\text{H}_2\text{O}$ fixed at 2.28×10^3 Pa. Impedance measurements were also carried out at open circuit potential in the $p\text{H}_2\text{O}$ range from 2.33×10^3 to 2.00×10^4 Pa (or from 2.3% to 19.7% of H_2O content in the gas atmosphere) fixing $p\text{H}_2$ at 8.11×10^4 Pa. Impedance measurements under standard conditions, the electrode being anodically polarised at 50, 100, 200, 300, 400 and 500 mV relative to the reference electrode, were also carried out. Potential values given in this list are not corrected for the ohmic IR drop of the electrolyte. Measurements of the activation energy were performed at standard conditions by decreasing the temperature from 850°C to 700°C in steps of 50°C.

The current-overpotential ($I-\eta$) measurements were carried out under standard conditions using a Solartron Electrochemical Interface 1287 for potentiostatic control. Prior to measurement the working electrode was anodically biased, relative to the reference electrode, at 750 mV for 30 min. Hereafter, the bias was decreased stepwise and the current was measured at each bias value. A steady-state current was measured usually within a few minutes. Overpotential data were corrected for the uncompensated series resistance of the electrolyte, the value of which was obtained from data of impedance measurements.

5.2.4 Microstructural characterization

After completing the electrochemical experiments, micrographs of the cermets were taken with a JEOL JSM-5800 Scanning Electron Microscope.

5.3 Results

5.3.1 Microstructure

Figure 5.2 shows micrographs of the Ni/YSZ10Ti cermet layer screen-printed on the YSZ electrolyte disc taken with the SEM after approximately 400 h of electrochemical testing. No difference in microstructure was observed between the Ni/YSZ5Ti and Ni/YSZ10Ti cermet anodes sintered at the same temperature. A porosity of ~50% was estimated from values of the layer thickness, mass and theoretical densities of both nickel and YZT.

Figure 5.3 shows the cross-section micrographs of Ni/YSZ10Ti sintered at 1300°C (top) and 1400°C (bottom). The thickness appears to be homogeneous all over the layer. The cermet anode sintered at 1300°C appears somewhat more porous and composed of finer particles than that sintered at 1400°C.

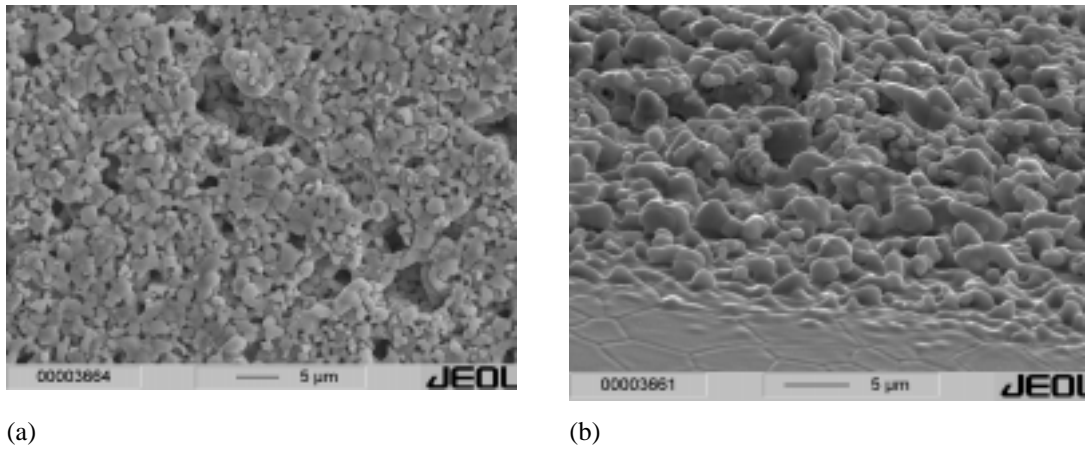


Figure 5.2: SEM micrographs of a screen-printed Ni/YSZ10Ti cermet anode taken after ~400 h of electrochemical testing. Micrographs were taken from the central area (a) and the rim (b). Note the free electrolyte surface at the rim of the anode.

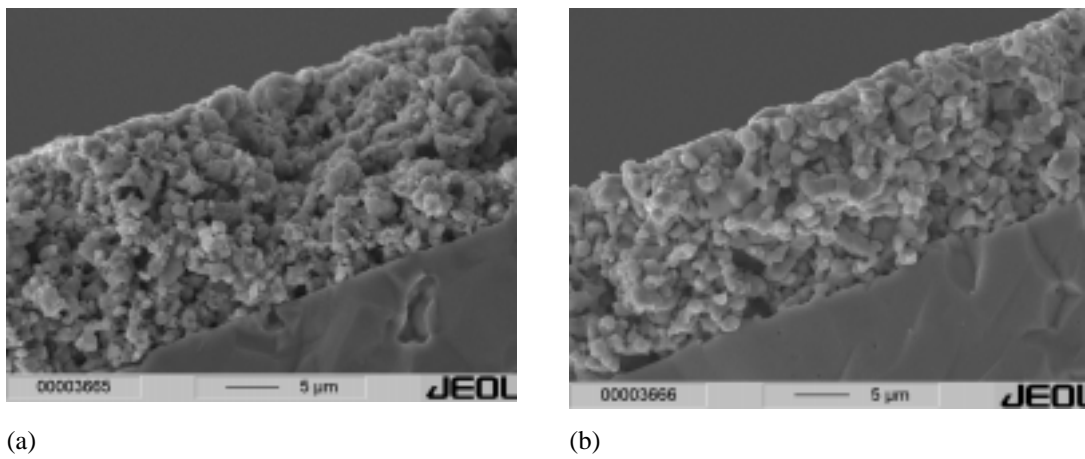


Figure 5.3: SEM cross-section micrographs of Ni/YSZ10Ti cermet anodes sintered at 1300°C (a) and 1400°C (b). Micrographs were taken after ~400 h of electrochemical testing.

5.3.2 Electrochemical experiments

5.3.2.1 Impedance measurements

Figure 5.4 shows impedance spectra obtained for different cermets under standard conditions. The spectra clearly show two depressed semi-circles. The spectra of Ni/YSZ5Ti and Ni/YSZ10Ti both sintered at 1300°C strongly resemble each other; Ni/YSZ10Ti sintered at 1400°C shows a considerably larger total electrode resistance.

Figure 5.5 shows impedance spectra of Ni/YSZ5Ti sintered at 1300°C as functions of p_{H_2} and $p_{\text{H}_2\text{O}}$ at 850°C. Spectra for the other samples were found to be similar. The apparent reaction orders with respect to H₂ and H₂O for the total electrode conductivity are shown in the insets of Figures 5.6 and 5.7. The overall reaction orders for both H₂ and H₂O are of the order of 0.2-0.3.

Activation energies of the total electrode conductivity for the different Ni/YZT cermets are shown in Table 5.2.

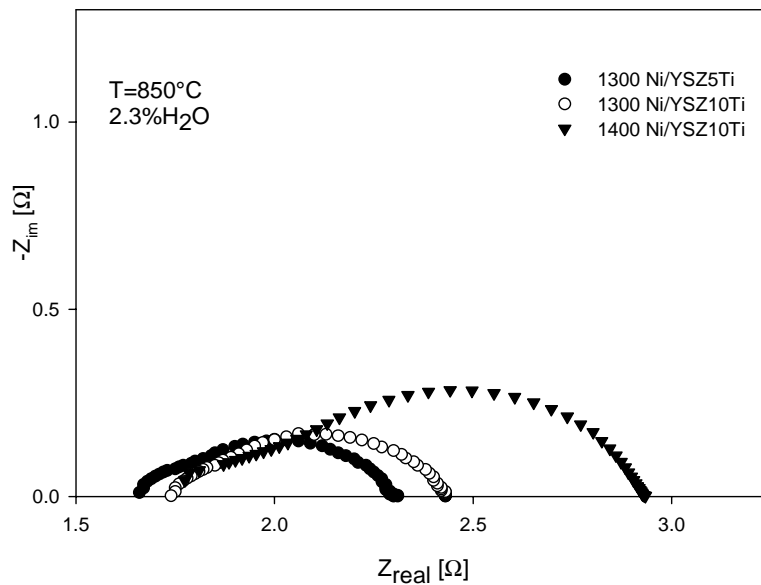


Figure 5.4: Impedance spectra of the three Ni/YZT cermets measured under standard conditions. The prefix in the notation for the cermets indicates the sintering temperature.

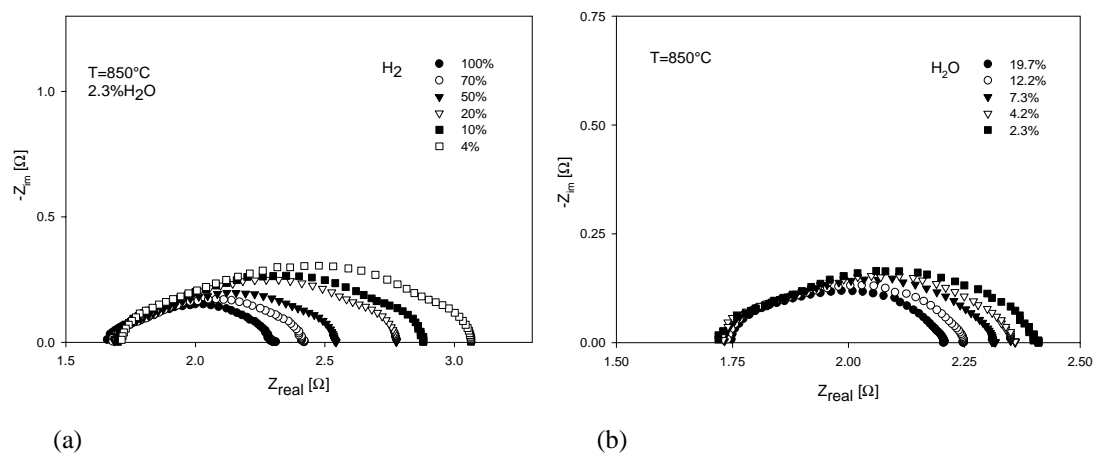


Figure 5.5: Partial pressure dependencies of the electrode impedance at 850°C of cermet Ni/YSZ5Ti sintered at 1300°C as functions of (a) p_{H_2} and (b) p_{H_2O} .

$T_{sinter}(^{\circ}C)$	cermet	E_a (kJ/mol)
1300	Ni/YSZ5Ti	117
1300	Ni/YSZ10Ti	134
1400	Ni/YSZ10Ti	124

Table 5.2: Activation energies for the total electrode conductivity. Data were extracted from data of impedance measurements under standard conditions in the range 700- 850°C.

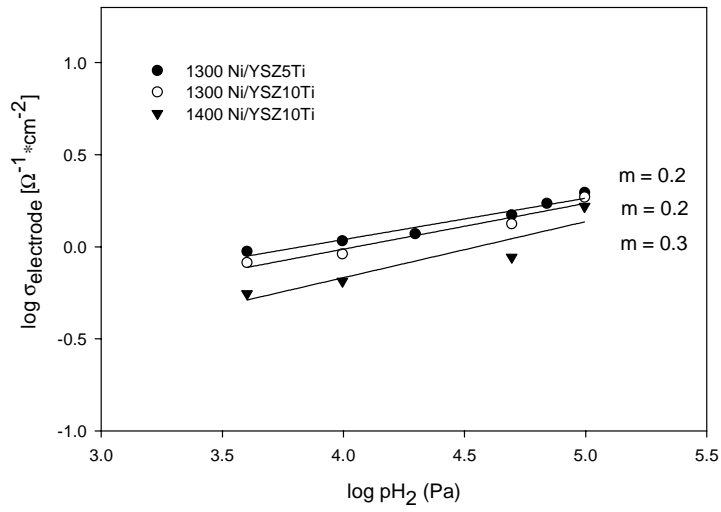


Figure 5.6: Total electrode conductivity for the three Ni/YZT cermet as a function of p_{H_2} measured at 850°C and $p_{H_2O}=2.3\times 10^5$ Pa. Corresponding values for the order m of the p_{H_2} dependence are as indicated.

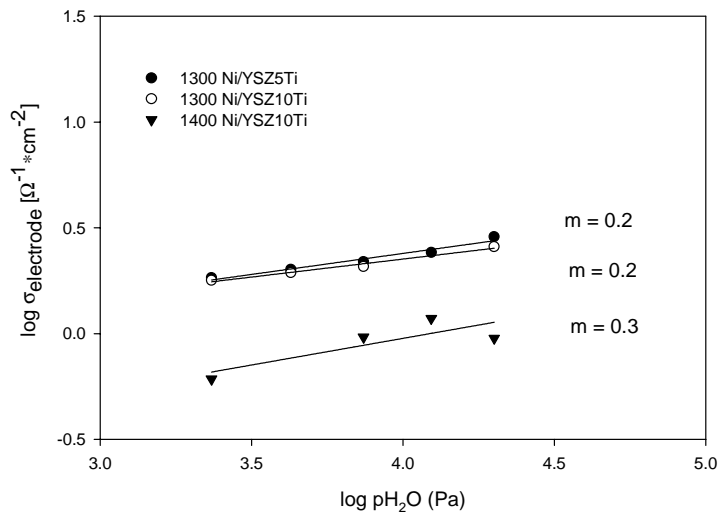


Figure 5.7: Total electrode conductivity for the three Ni/YZT cermet as a function of p_{H_2O} measured at 850°C and $p_{H_2}=8.1\times 10^4$ Pa. Corresponding values for the order m of the p_{H_2O} dependence are as indicated.

Almost all impedance spectra could be analysed with the equivalent circuit presented in Figure 5.8. Results from the analysis of the impedance spectra of the cermet Ni/YSZ5Ti sintered at 1300°C are presented in next sections.

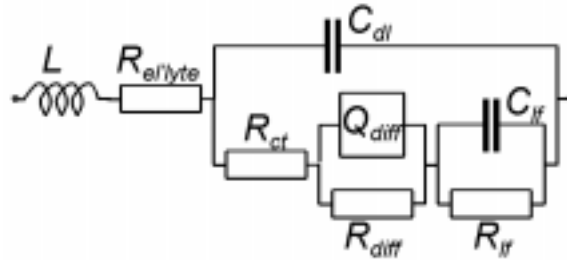


Figure 5.8: Equivalent circuit model used in the CNLS-analysis of the electrode impedance for the Ni/YSZ5Ti cermet sintered at 1300°C.

In Figure 5.8 L is an inductance, which is introduced by the measurement instrument, C_{dl} is a double layer capacitance. The lower branch presents the chemical route of the charge transfer process (R_{ct}). Although the actual processes take place in a ‘distributed system’, this simplification can characterise quite well the impedance spectra with a pseudo- χ^2 value [12] in the range 7×10^{-6} to 3×10^{-7} . These values were quite close to the χ^2 values obtained from a Kramers-Kronig transform test [13] of the data, which indicates that the equivalent circuit model adequately can describe the measured impedance spectra. Furthermore, the CNLS-parameters show a consistent dependence on pH_2 or pH_2O .

The Q_{diff} represents a CPE (Constant Phase Element), which is parameterised by (admittance form):

$$Y(\omega) = Y_0 \cdot (j\omega)^n = (Y'_0 \cdot j \cdot \omega)^n \quad (5.1)$$

Although the first expression is used in general, the second representation often results in a less ‘erratic’ behaviour of the parameter Y'_0 . The relation between the two

parameters is given by $Y_0' = (Y_0)^{1/n}$. In this chapter the parameter Y_0' will be called the ‘normalised parameter’, or normalised Q_{diff} .

5.3.2.2 $p\text{H}_2$ dependence of the circuit parameters

The electrolyte resistance, $R_{\text{el'lyte}}$, is independent of the $p\text{H}_2$, as expected (see Figure 5.9). Both the charge transfer resistance, R_{ct} , and the ‘diffusion’ resistance, R_{diff} , show a clear $p\text{H}_2$ dependence. In Figure 5.9 a trend line with slope $-1/4$ is drawn for comparison. An actual fit to the data points results in values close to $-1/4$.

The apparent double layer capacitance, C_{dl} , seems to show some dependence (see Figure 5.10), but the error estimate is rather large for this parameter ($\sim 20\text{-}40\%$). The Y_0 parameter of the Q_{diff} CPE shows a clear $p\text{H}_2$ dependence, with an approximate $+1/4$ power. For the normalised Y_0' this value is even somewhat higher.

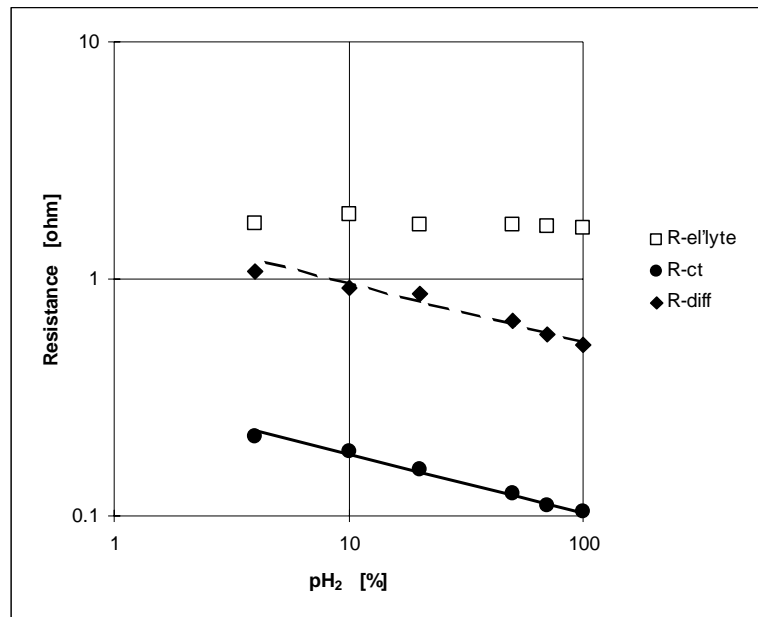


Figure 5.9: $p\text{H}_2$ dependencies of the electrolyte resistance, the charge transfer resistance and the ‘diffusion’ resistance.

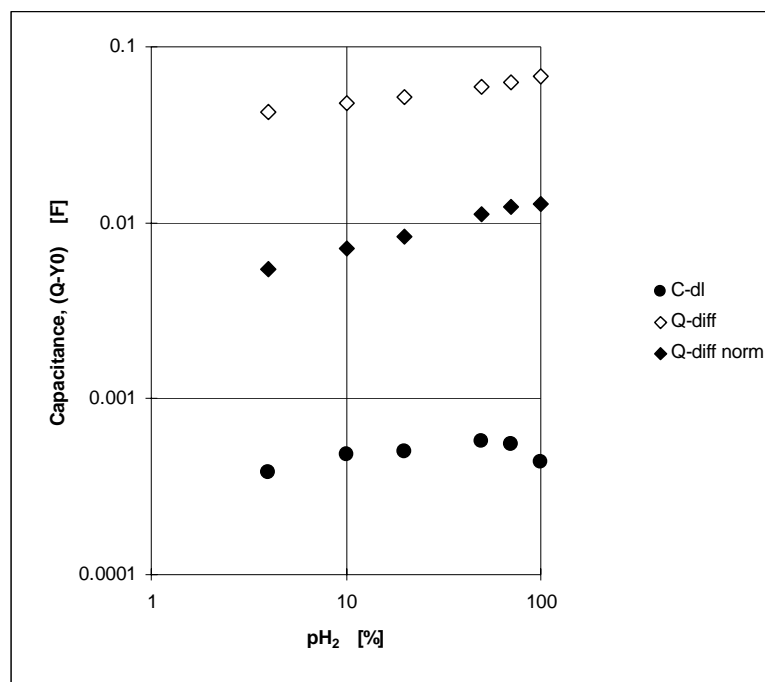


Figure 5.10: $p\text{H}_2$ dependence of the double layer capacitance and the ‘diffusion’ CPE. The normalised parameter of the ‘diffusion’ CPE is also shown (see text).

5.3.2.3 $p\text{H}_2\text{O}$ dependence of the circuit parameters

The electrolyte resistance, $R_{\text{el'lyte}}$, is independent of the $p\text{H}_2\text{O}$ as expected (see Figure 5.11). The charge transfer resistance, R_{ct} , however, seems to approach a saturation value. The initial slope is close to 1/4 (broken line in Figure 5.11). The ‘diffusion’ resistance, R_{diff} , shows, as for the $p\text{H}_2$ dependence, approximately a $-1/4$ power.

The double layer capacitance (Figure 5.12) does not show a $p\text{H}_2\text{O}$ dependence (within the parameter uncertainty). The Y_0 parameter of the CPE shows, in contrast with the $p\text{H}_2$ dependence, approximately a $-1/4$ power dependence.

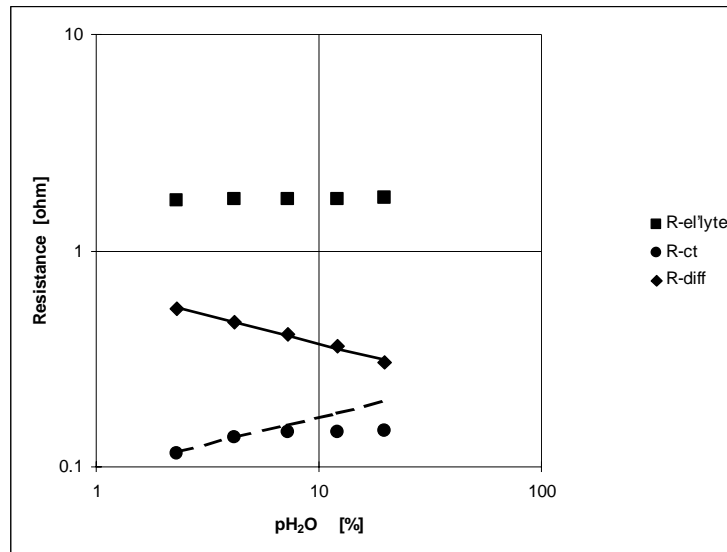


Figure 5.11: $p\text{H}_2\text{O}$ dependencies of the electrolyte resistance, the charge transfer resistance and the ‘diffusion’ resistance.

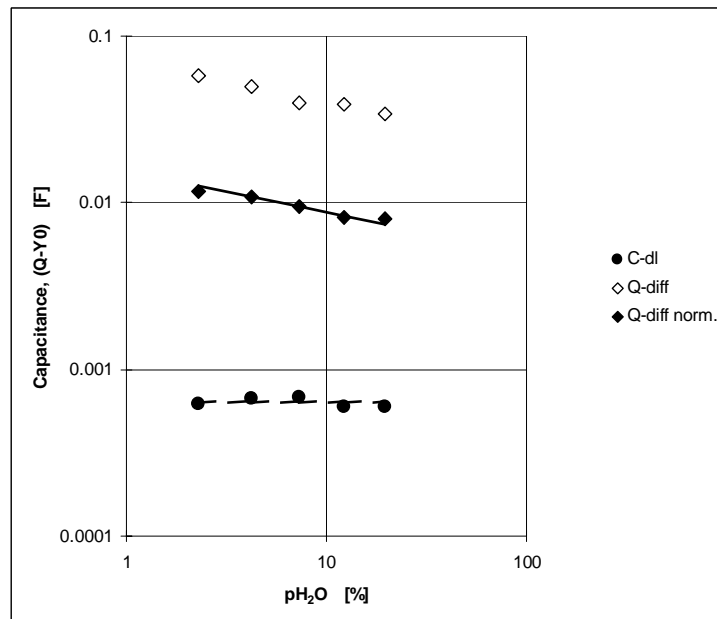


Figure 5.12: $p\text{H}_2\text{O}$ dependencies of the double layer capacitance and the ‘diffusion’ CPE. The normalised parameter of the ‘diffusion’ CPE is also shown. Lines serve as a guide to the eye.

5.3.2.4 pO_2 dependence of the circuit parameters

The conductive properties of the YZT depend on the partial pressure of oxygen, which is connected to the hydrogen and water partial pressures through the following expression, provided that equilibrium is attained:

$$pO_2 = K \frac{(pH_2O)^2}{(pH_2)^2} \quad (5.2)$$

Hence, when the pH_2O is fixed and the pH_2 is increased, the pO_2 will decrease. Vice versa, the pO_2 will increase when the pH_2O is increased. In fact, the pH_2 and pH_2O dependencies of the parameters can be plotted as a function of pO_2 in a single graph. This can help in distinguishing which parameters could pertain to bulk and surface properties of the YZT particles, and which parameters are not directly related to properties of the YZT.

Figure 5.13 shows a compilation of the resistance values. The electrolyte resistance, $R_{el'lyte}$, is independent of pO_2 within experimental accuracy, as expected. The charge transfer resistance, R_{ct} , clearly shows a pO_2 dependence and could relate to the defect chemistry of the YZT phase. Disagreement in data from pH_2 and pH_2O dependent measurements for the 'diffusion' resistance, R_{diff} , (see Figure 5.13), indicates that in this case the pO_2 is not the governing parameter. Hence this resistance cannot be directly related to the YZT defect properties.

In contrast, the Y_0 parameter of the diffusion CPE shows again consistent pO_2 dependence like R_{ct} . An even clearer trend is observed for the normalised, Y_0' parameter, indicating a decrease with increasing pO_2 , see Figure 5.14. The double layer capacitance, C_{dl} , shows within experimental error, to be more or less independent of the oxygen partial pressure.

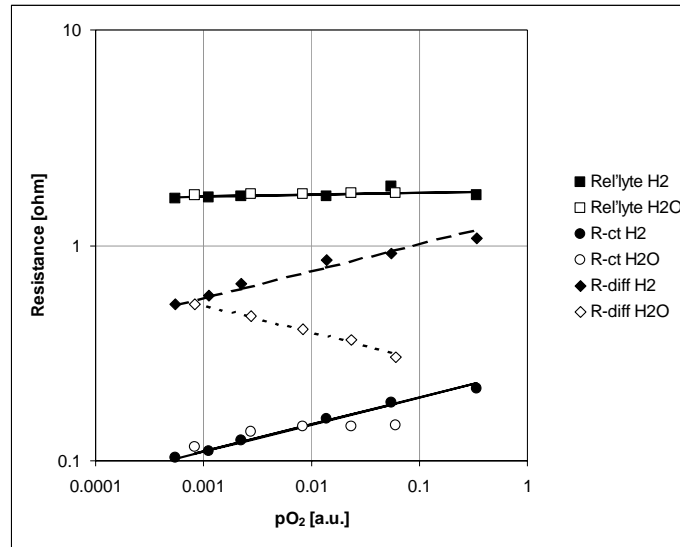


Figure 5.13: pH_2 and pH_2O dependencies of the resistive elements transformed to pO_2 dependencies. Closed symbols with varying pH_2 and open symbols with varying pH_2O . Lines serve as a guide to the eye.

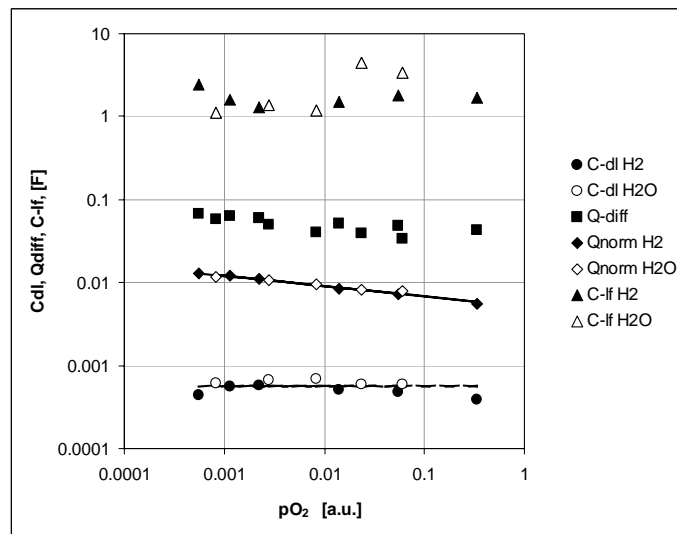


Figure 5.14: pH_2 and pH_2O dependencies of the capacitances and the diffusion CPE transformed to pO_2 dependencies. Closed symbols with varying pH_2 and open symbols with varying pH_2O .

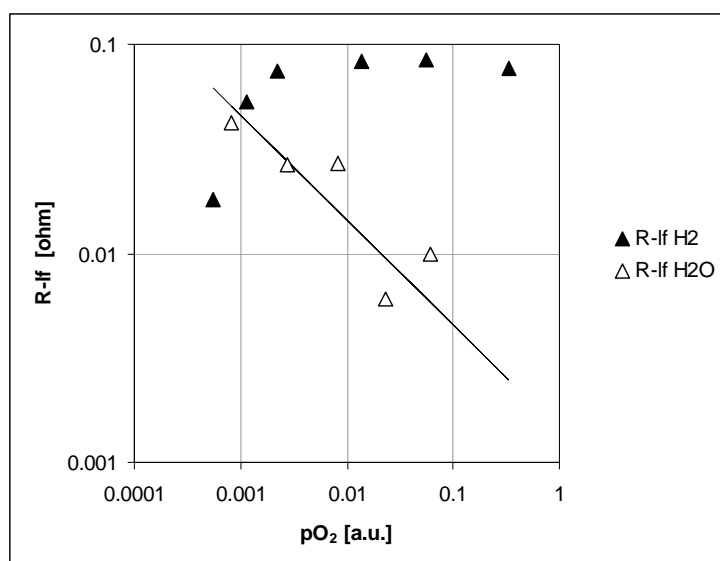


Figure 5.15: pH_2 and pH_2O dependencies of the low frequency resistance, R_{if} , transformed to pO_2 dependencies.

The low frequency capacitance, C_{if} , can also be regarded to be independent of pO_2 , as the error estimate often is quite large. On the other hand the low frequency resistance, R_{if} , seems to be strongly dependent on the pH_2O and to a lesser extent on the pH_2 , see Figure 5.15.

5.3.2.5 Polarisation dependence of the circuit parameters

The charge transfer resistance, R_{ct} , shows, up to about 0.3 V bias, an exponential decrease with an approximate charge transfer coefficient of -0.3 (see Figure 5.17). For higher bias values R_{ct} increases again, but in this voltage range the electrode dispersion changes considerably, showing an additional ‘inductive loop’ and a significant capacitive loop at the low frequency limit (see Figure 5.16). The electrolyte resistance shows no dependence on bias potential.

The behaviour of R_{diff} up to about 0.3 V is rather erratic, for higher bias potentials a clear decrease is noticeable (Figure 5.17).

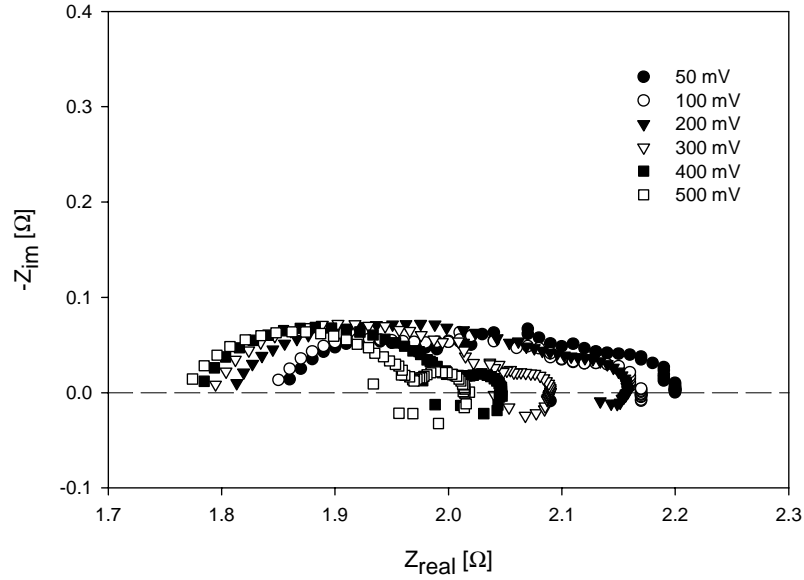


Figure 5.16: Impedance spectra for the cermet Ni/YSZ5Ti (sintered at 1300°C) measured under standard conditions at different values for the anodic polarisation. Potential values shown in the insert are not corrected for the ohmic IR drop of the electrolyte.

The behaviour of Q_{diff} is more pronounced. The charge transfer coefficient for the Y_0 -parameter (see Figure 5.18) is approximately -0.45 . For the normalised Y_0' a value of approximately -0.7 is found. The frequency power dependence of the CPE clearly tends to $n = 0.5$ under bias, which is indicative of diffusion behaviour (Warburg impedance).

The low frequency semicircle (R_{lf} - C_{lf}) is, within the rather large experimental error, not affected by the applied bias, see Figure 5.19.

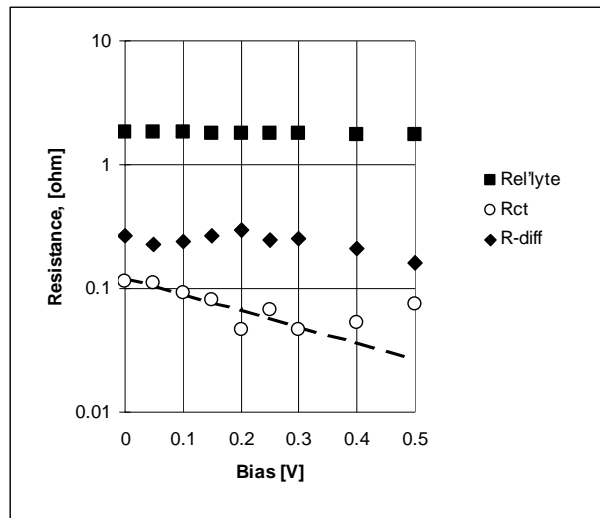


Figure 5.17: Bias dependence of the resistive parameters for anodic polarisation. The broken line presents an exponential fit to the R_{ct} data points on the range 0-0.3 V.

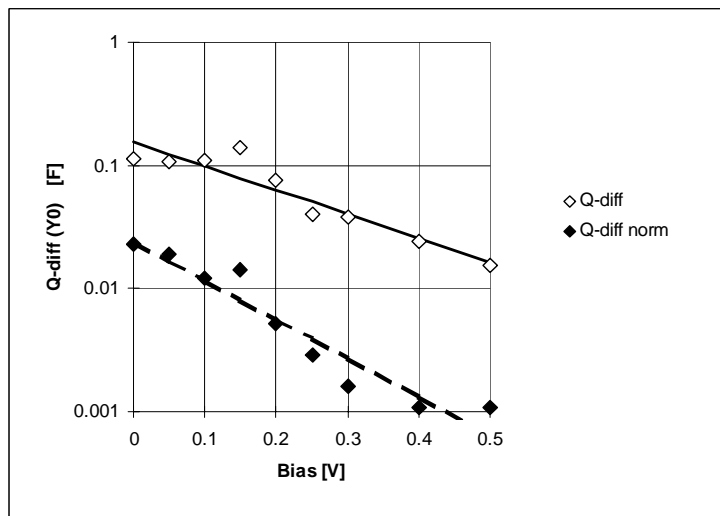


Figure 5.18: Bias dependence of the Y_0 and normalised Y_0 parameters of the 'diffusion' CPE. The lines present an exponential fit to the parameters.

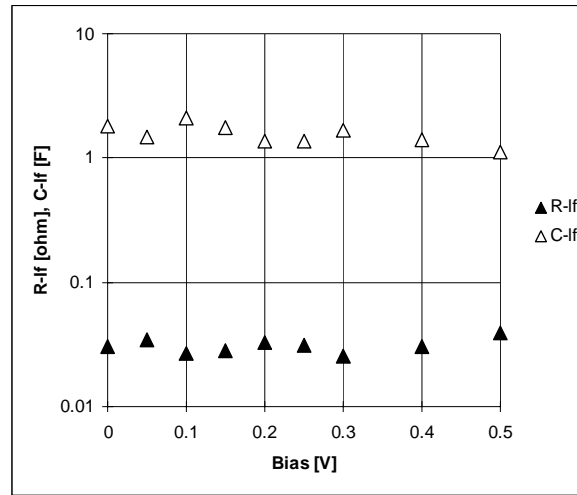


Figure 5.19: Parameters (R_{lf} , C_{lf}) of the low frequency semicircle versus bias voltage.

5.3.2.6 I - η measurements

Tafel representations of the I - η measurements for the different Ni/YZT cermets, performed under standard conditions, are given in Figure 5.20. Cathodic and anodic transfer coefficients estimated from the Tafel plots are listed in Table 5.1.

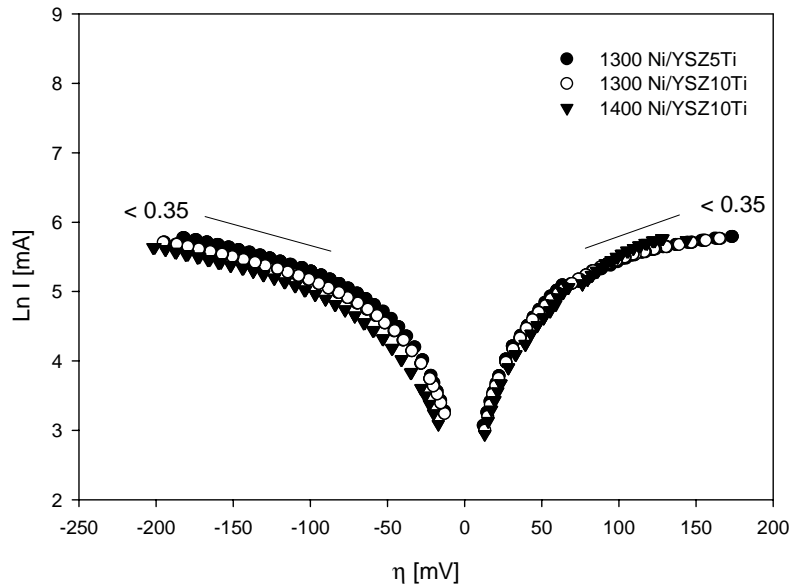


Figure 5.20: Tafel plots for different Ni/YZT cermets measured under standard conditions.

cermet	α_a	α_c
1300 Ni/YSZ5Ti	0.29	0.30
1300 Ni/YSZ10Ti	0.30	0.32
1400 Ni/YSZ10Ti	0.30	0.35

Table 5.1: Estimated values for the apparent charge transfer coefficients from I - η measurements for the different Ni/YZT cermets.

5.3.2.7 Electrode stability

Figures 5.21, 5.22 and 5.23 show for the different cermets the evolution of the impedance spectra with time. Spectra were recorded after each electrochemical test over a total period of approximately 400 h. Note that for each cermet the total electrode polarization decreases considerably with time. Also note the increasing value for the high frequency intercept with time. This effect is much smaller for Ni/YSZ10Ti sintered at 1400°C, compared with the cermets sintered at 1300°C.

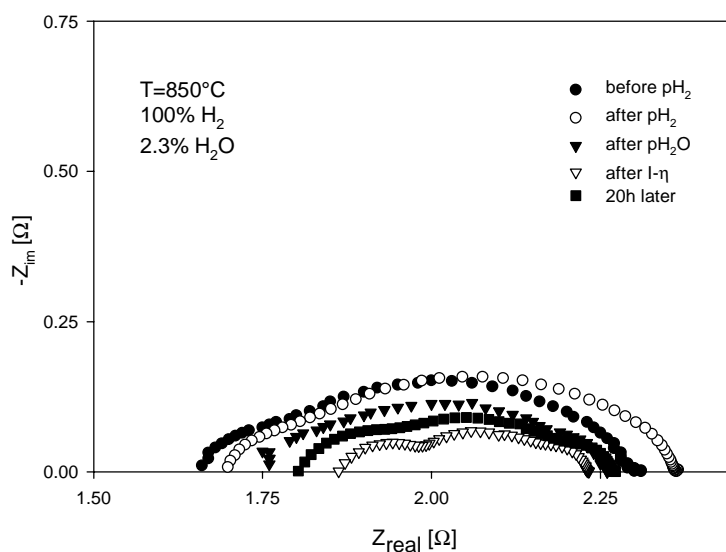


Figure 5.21: Impedance spectra for the cermet Ni/YSZ5Ti (sintered at 1300°C) measured under standard conditions. Individual spectra were taken after each electrochemical test over a total period of ~400 h.

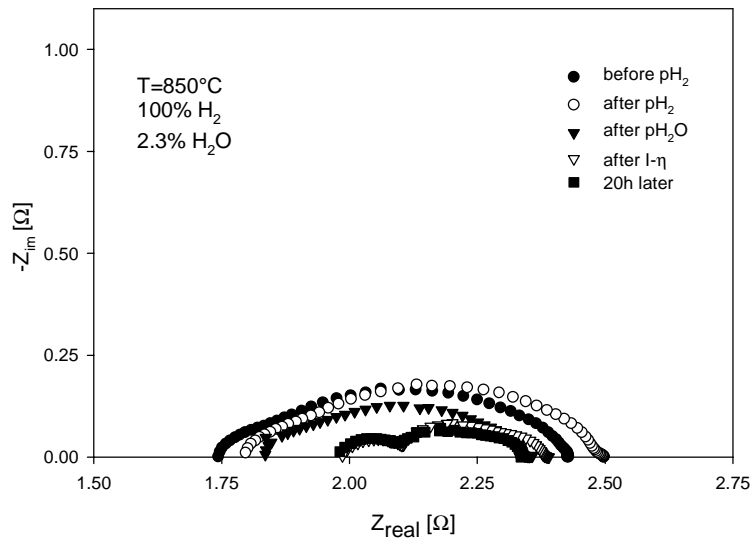


Figure 5.22: Impedance spectra for the cermet Ni/YSZ10Ti (sintered at 1300°C) measured under standard conditions. Individual spectra were taken after each electrochemical test over a total period of ~400 h.

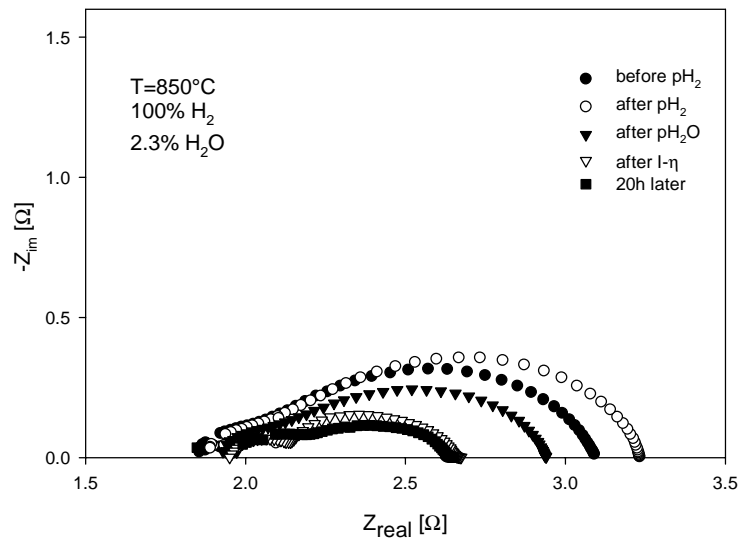


Figure 5.23: Impedance spectra for the cermet Ni/YSZ10Ti (sintered at 1400°C) measured under standard conditions. Individual spectra were taken after each electrochemical test over a total period of ~400 h.

5.4 Discussion and conclusions

The Ni/YZT cermets, which have not yet been optimised, show a good performance at 850°C. Comparable performances were obtained for the 5% and 10% Ti-doped YSZ cermets sintered at 1300°C, but these electrodes show some degradation with time (see Figures 5.21 and 5.22). The 10% Ti-doped YSZ cermet, sintered at 1400°C, shows a good stability with time, but it also shows the highest electrode resistance.

The cermet electrode represents a very distributed system, in which the electrode processes occur nonuniformly through the depth of the electrode. Nevertheless the equivalent circuit given in Figure 5.8 is able to model the impedance data as function of $p\text{H}_2$, $p\text{H}_2\text{O}$ and under polarisation. The double layer capacitance, C_{dl} , has a value of about 1 mF/cm². This is somewhat higher than observed for a Ni-patterned electrode on YSZ (~0.3 mF/cm², [14]), but somewhat lower than for a fine-grained Ni/YSZ cermet electrode (~2 mF/cm², [14]). The charge transfer resistance, R_{ct} , appears to be polarisation dependent, i.e., decreasing with increasing bias potential. For a clear assignment further research is necessary.

The frequency power dependence, n , of Q_{diff} was found to be around 0.6 to 0.7 in the partial pressure dependent measurements. If a bias is applied this value decreases to a value of $n \approx 0.5$ (± 0.05), which corresponds to a Warburg diffusion impedance. Similar electrode responses have been observed for porous noble metal electrodes on ionic conductors with a non-vanishing electronic conductivity [15-17]. The occurrence of the diffusion-like impedance Q_{diff} might be related to the spreading of the reaction zone in Ni/YZT cermets. Charge transfer could occur on redox centres of the free YZT surface, but the process is accompanied by the subsurface diffusion of electronic charge carriers to assure the electroneutrality. The parameter Y_0' decreases with increasing $p\text{O}_2$ (whether caused by increasing $p\text{H}_2\text{O}$ or decreasing $p\text{H}_2$), which is a strong argument for the importance of defect electrons in the electrode response of Ni/YZT cermets. Further study is however required to elucidate the mechanism of the electrode reaction.

The electrochemical behaviour of the studied Ni/YZT cermets can be summarised as follows:

- Under standard conditions, the overall shape of the impedance spectra is similar for all three cermets, indicating that the reaction mechanism is the same for the different compositions and microstructures. Impedance data also show that at least three processes play a role in the electrode reaction.
- Analysis of the slopes in the Tafel plots yields approximate values of 0.3 for both the apparent anodic and cathodic transfer coefficients (see Table 5.1).
- It can be seen from the impedance spectra presented in Figures 5.21, 5.22 and 5.23 that there is a large influence of the measurements on the electrode performance, lowering the total electrode resistance considerably. It can be observed that it is mostly the low frequency arc that evolves with time. This evolution of the total electrode resistance with time has not been observed before with the Ni/YSZ cermets, in which the total electrode resistance tends to increase with time. This effect could be ascribed to the presence of Ti in the ceramic, although further research is necessary to unravel this.
- An increase in the value for the high frequency intercept with time could be observed (see Figures 5.21 to 5.23). It seems that there is an ‘interface resistance’ which develops in time. This effect is much smaller for the 1400 Ni/YSZ10Ti cermet. This could be due to a better attachment of the electrode on the electrolyte in this sample.

The different Ni/YZT cermets investigated showed a similar behaviour as function of H₂ partial pressure. The same was observed for the H₂O partial pressure. The total electrode resistance for the composition sintered at 1400°C was larger than those sintered at 1300°C. The shape of the impedance diagram was similar for all compositions. All cermets investigated showed a large decrease in electrode polarisation with time, which was not observed before with Ni/YSZ cermets. Total electrode resistance of the Ni/YZT cermets was of the same order of that of the state-of-the-art SOFC Ni/YSZ. Further research is necessary to elucidate the role of Ti in the electrochemical performance of Ni/YZT cermets.

References

- [1] T. Setoguchi, K. Okamoto, K. Eguchi and H. Arai, *J. Electrochem. Soc.* 139, 2875-2880, 1992.
- [2] S.S. Liou and W.L. Worrell, *Appl. Phys. A* 49, 25-31, 1989.
- [3] L.S.M. Traqueira, T. Pagnier and F.M.B. Marques, *J. Eur. Ceram. Soc.* 17, 1019-1026, 1997.
- [4] M.T. Colomer, L.S.M. Traqueira, J.R. Jurado and F.M.B. Marques, *Materials Research Bulletin* 30, 4, 515-522, 1995.
- [5] A. Kaiser, A.J. Feighery, D.P. Fagg and J.T.S. Irvine, *Ionics* 4, 215-219, 1998.
- [6] A.J. Feighery, J.T.S. Irvine, D.P. Fagg, A. Kaiser, *J. Solid State Chemistry* 143, 273-276, 1999.
- [7] K. Kobayashi, Y. Kai, S. Yamaguchi, N. Fukatsu, T. Kawashime and Y. Iguchi, *Solid State Ionics* 93, 193-199, 1997.
- [8] D. Skarmoutsos, A. Tsoga, A. Naoumidis, P. Nikolopoulos, *Solid State Ionics* 135, 439-444, 2000.
- [9] A. Tsoga, A. Naoumidis and P. Nikolopoulos, *Acta Mater.* 44, 3679-3692, 1996.
- [10] D. Skarmoutsos, F. Tietz and P. Nikolopoulos, *Fuel Cells* 1, 3-4, 243-248, 2001.
- [11] P. Kontouros, R. Förthmann, A. Naoumidis, G. Stochniol and E. Syskakis, *Ionics* 1, 40-50, 1995.
- [12] B.A. Boukamp, *Solid State Ionics* 1986, 20, 31-44, 1986.
- [13] B.A. Boukamp, *J. Electrochem. Soc.* 142, 1885-1894, 1995.
- [14] B. de Boer, PhD Thesis, University of Twente, 1998.
- [15] B.A. Boukamp, B.A. van Hassel, I.C. Vinke, K.J. de Vries and A.J. Burggraaf, *Electrochim. Acta* 38, 1817-1825, 1993.
- [16] B.A. Boukamp, 'Elucidation by EIS of the electrode reaction of the BiCuVOx/noble metal/oxygen electrode system', Presented at the 5th Micro-Symposium on Electrochemical Impedance Analysis, Balatonföldvár, Hungary May/June 1999, accepted, *ACH-Models in Chemistry* 137 [2/3], 225-242, 2000.
- [17] B.A. Boukamp, *Solid State Ionics* 135-137, 75-82, 2000.

Appendix A

Percolation and conduction in disordered media

Transport properties of disordered media are treated from the point of view of percolation theory. For this purpose, elements of percolation theory are presented as well as an introduction to the effective medium theory and scaling laws that govern the properties of percolative systems near the critical point. A review is given of the most relevant statistical discrete models (network modelling) and continuum percolation models. Finally the possibilities of these models to predict the effective properties (mainly conductivity) of several composite materials are presented and discussed.

A.1 Introduction

Only recently the ideas of the statistical physics of disordered media, such as percolation theory, effective-medium theories, scaling laws and network modelling of the medium have been applied to study the transport and reaction phenomena in composite media. By disordered media we mean, within this context, media with an irregular microstructure. Examples are composite materials and porous media.

This appendix reviews the relevant literature on the subject, defines and discusses relevant ideas of the statistical physics of disordered media, and reviews the progress that has been made as a result of the application of such ideas. In particular the important effect of the topology (connectivity) of the system on its transport and reaction properties is stressed here.

A.1.1 *Transport in disordered media*

Disorder in materials plays an important role in many situations of industrial and scientific interest. Of all the disordered systems, composites, porous media and polymers are the most important ones. These systems have been studied for a long time, but it was not until recently with the development of new techniques and theories, that it has become possible to study the structure of such systems in a better manner and to gain a deeper understanding of their properties. New techniques have also allowed to model the structure of many disordered media in such a manner that their properties can be more easily studied. Network representation is one example.

From a general point of view, models describing transport in disordered media can be divided into classical and statistical models. An outline about what they consist of is given here.

A.1.1.1 Classical Models

Classical models represent the classical approach for describing materials of complex and irregular geometry. The material is treated as a continuum and the parameters characterising the system, such as temperature or conductivity, are defined as smooth

functions of time and position. Classical models have been widely applied because of their convenience and familiarity to the engineer but they have some important limitations: one is that they are not well suited for describing drastic changes in the connectivity of the medium [1]. For information about continuum models the interested reader is referred to [1-4].

A.1.1.2 Statistical percolation models

Statistical models represent the new approach for describing disordered media. These models are divided into two categories:

- a) Statistical discrete models
- b) Statistical continuum models

In a *statistical discrete model* the material is treated as a collection of elements such as sites in the crystalline lattice, voids etc. They are based on a network representation of the system and concepts of statistical physics of disordered media are used to describe the percolative behaviour of such networks.

Concepts of percolation theory, scaling laws and effective-medium theory are used for the development of statistical discrete models.

Statistical continuum models were developed for two-phase composite materials and porous media. In these models a continuous matrix represents the system. The other phase, which is composed by inclusions, sticks or plates, is embedded into the matrix. Both discrete and continuum models can describe properly drastic changes in the connectivity of the medium, but their main shortcoming is the large computational effort that is required for a realistic discrete treatment of the system. In this chapter these statistical models are all reviewed.

A.2 Percolation theory

In this section an overview is given of the most relevant elements of percolation theory. The two characteristic treatments, i.e. site and bond percolation treatments are defined together with the most relevant percolation quantities. An introduction is also

given to the effective medium percolation theory and to the scaling laws that govern the percolation systems near the critical point, the so-called percolation threshold.

A.2.1 What is percolation?

Percolation theory deals with the properties of classical particles interacting with a random medium. It is of wide applicability and provides a simple representation of a system showing critical behaviour.

Percolation phenomena are characterised by a transition point, the so-called *percolation threshold* p_c . At this p_c a sudden change in the properties of a disordered medium occurs when its previously disconnected regions (see pictures (a) and (b) in Figure A.1) grow together to form a continuous path (see picture (c) in Figure A.1). This change in the state of the system is considered to be the geometric analogue of a *second order phase transition*, such as when a ferromagnetic material undergoes spontaneous magnetisation M at $T < T_C$ with T_C the Curie Temperature [5].

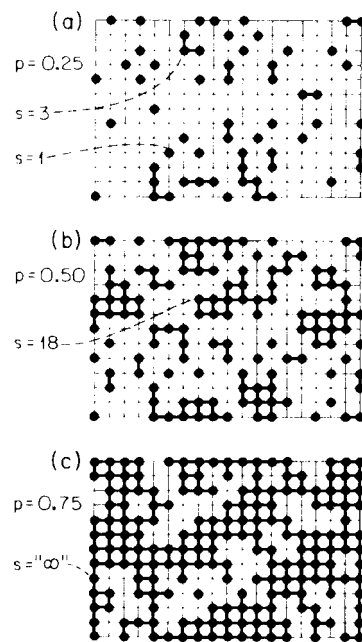


Figure A.1: Site percolation on a square network. Solid circles denote occupied sites.

Nowadays, essentially two approaches are used to solve percolation problems [6]: Monte Carlo simulations and scaling theory.

The first one can be considered as the ‘experimental approach’ to percolation and in many cases Monte Carlo results are the only information available. In this case one first generates a computer model of the disordered medium. In the scaling theory relationships between critical exponents are reported on the basis of scaling

assumptions which are usually confronted with the results obtained from Monte Carlo methods [2, 5, 7-9].

A.2.2 *The percolation problem*

Here some terminology will be introduced which will be useful in understanding the problem of percolation in a random medium in more general terms.

A.2.2.1 The medium

In the terminology of percolation phenomena, the medium is defined as an infinite set or *network* of objects called *sites*, even if reality deals with finite systems. The paths connecting sites are called *bonds* and the number of them connected to a site is called its *co-ordination number* [1].

The medium in percolation phenomena, although it may vary randomly from point to point, is constant in time and dictates the paths of the particles. In this case the randomness is ascribed to the *medium*.

A.2.2.2 Bond and site percolation treatments

To define percolation phenomena some random mechanism has to be associated with the medium. This can be done in two distinct ways and therefore two different treatments exist: the bond percolation treatment and the site percolation treatment.

Bond percolation treatment

In the *bond* percolation treatment the bonds of the network are either open (connecting two sites), randomly and independently of each other, with probability p , or closed with probability $1-p$ (see Figure A.2). In this case all the sites in the network are supposed to be occupied. Two sites are called *connected* if at least one path exists between them consisting of open (or connecting) bonds only. A set of connected sites bounded by vacant bonds is called a *cluster*. If the network is of a very large extent and if p is sufficiently small, the size of any connected cluster is likely to be small. But if p is close to 1, the network should be entirely connected, apart from occasional small holes. At some well-defined value of p , there is a transition in the topological

structure of the random network, this value of p is called *bond percolation threshold*, p_{cb} . This is the largest fraction of occupied bonds below which there is no sample-spanning cluster of occupied bonds.

Site percolation treatment

In the case of *site* percolation treatment, sites of the network are occupied with probability p (and vacant with probability $1-p$) and all the bonds are supposed to be open. Two nearest neighbouring sites are called *connected* if they are

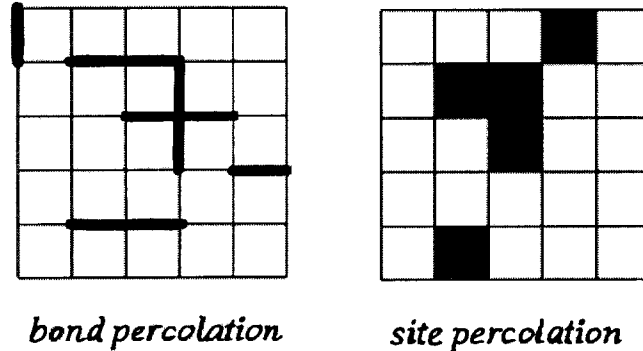


Figure A.2: Bond and site percolation in a two-dimensional network.

both occupied, and *connected clusters* on the network are again defined in the obvious way. As before, there is a site percolation threshold p_{cs} above which an infinite cluster of occupied sites spans the network. It is always possible to convert a bond percolation problem to a site percolation problem on a different lattice [5,10] and, therefore, site percolation problems are more fundamental. In fact, most engineering problems of interest that will be discussed in this work are site percolation problems.

Note that the percolation phenomenon as defined above is a static process in such a way that once a percolation cluster is generated its configuration is in equilibrium and does not change with time.

A.2.3 Universal scaling laws: critical exponents

Numerical and theoretical evidence exist [1, 2, 5] that, the behaviour of many percolation quantities near the percolation threshold is insensitive to the lattice structure for periodic D -dimensional networks. Therefore, near the percolation threshold p_c , most percolation quantities obey scaling laws that are independent of the network structure and its microscopic details. This fact is reflected, for instance in the following scaling law for the most relevant percolation probability $P_s(p)$, which is only valid in the vicinity of p_c [5]:

$$P_s(p) \sim (p - p_c)^\beta \quad (\text{A.1})$$

The *critical exponents* depend only on the dimension, D , of the system and if the same critical exponents describe two different phenomena they are said to belong to the same *universality class*. If two phenomena are described by two different sets of critical exponents the physical laws governing the two phenomena are fundamentally different. Thus, critical exponents can help to distinguish between different classes of problems and the physical laws that govern them.

There are several physical quantities that also follow scaling laws at the critical region, for instance the electrical conductivity σ in a composite or metallic material, the spontaneous magnetisation M in a ferromagnetic material, the specific heat C in a phase transition, etc. [7, 8]. For a regular network of resistors the conductivity $\sigma(p)$ follows the scaling law [9, 13, 14]:

$$\sigma \sim (p - p_c)^t \quad (\text{A.2})$$

for p just above p_c , because for p less than p_c the network is not conducting. The critical exponent t determines how conductivity approaches to zero at $p = p_c$. It has not yet been possible to calculate exactly the values of t for 3D networks, but it can be estimated by means of theoretical methods, for instance the finite-size scaling [11], the renormalisation group method [5, 12, 15], and conductance measurements [9, 14, 16]. Values for t of 1.26 and 1.87 were obtained for 2D and 3D networks respectively by Sahimi *et al.* [11].

In the case of two-phase composite materials the critical region is quite broad and therefore such universal scaling laws can be very useful to predict the effective properties of this material over a broad range of the volume fraction V of the components [2]. The conductivity in such systems, in which only one phase is conducting and whose particles do not overlap one another, follows the scaling law in the vicinity of the percolation threshold:

$$\sigma \sim (V - V_c)^t \quad (\text{A.3})$$

in which V is the volume fraction of conducting material and V_c is the critical volume fraction necessary for the conductive phase to percolate.

Studies supporting equation (A.3) and their theoretical assumptions span a wide range of materials, including inorganic conductive mixtures [17], metal/polymer mixtures [18, 19], and carbon black/polymer mixtures [20, 21].

For systems in which both phases are conducting or particles overlap, expression (A.3) is not valid and more complicated expressions have to be used to predict the conductivity [22, 23]. In Section 3 these cases will be studied in detail.

A.2.4 Effective medium percolation theory

Far from the percolation threshold p_c , the effective properties of a disordered medium can be accurately predicted by the effective-medium approximation (EMA). In its original form, developed by Bruggeman [24] and Landauer [25], the EMA was unrelated to percolation, but recently it has been combined with elements of percolation theory [6, 9, 12, 23]. This has given rise to an effective-medium percolation theory (EMPT) that has been the first analytical approximation able to predict a percolation threshold valid for describing material properties near the percolation threshold. This EMPT provides the overall conductivity of a random mixture of particles of two different conductivities under the assumption that the inhomogeneous surrounding of a particle can be replaced by an effective medium [12]. The theory gives the following expression for the effective resistivity, ρ_m , of a random mixture of particles of two different resistivities ρ_1 and ρ_2 :

$$\rho_m = \frac{4\rho_1\rho_2}{\rho_1(3V_2 - 1) + \rho_2(3V_1 - 1) + \alpha} \quad (\text{A.4})$$

in which V_1 and V_2 are the volume fraction of components 1 and 2 respectively, and α is calculated from the expression:

$$\alpha = \left\{ \left[\rho_1(3V_2 - 1) + \rho_2(3V_1 - 1) \right]^2 + 8\rho_1\rho_2 \right\}^{1/2} \quad (\text{A.5})$$

A.2.5 Approach of Kirkpatrick

Kirkpatrick extended the effective-medium approximation (EMA) to percolation networks of bonds whose conductivity is assigned at random [9]. He demonstrated by means of computer calculations that the EMPT provides an extremely accurate solution to the bond percolation problem, except in the vicinity of the percolation threshold, where it deviates by a few percent (see data points in Figure A.3 when p_c is approached). In Figure A.3 the solid line represents the predictions of the EMPT and data points (circles and triangles) are computer calculations for 3D resistor networks with $15 \times 15 \times 15$ nodes. $\sigma(0)$ has a characteristic value of large allowed regions of the material. In the critical region the scaling expression (A.2) holds true.

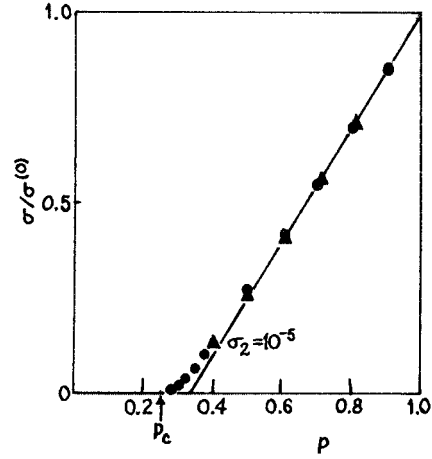


Figure A.3: Conductivity of a simple cubic network with two different conductances: $\sigma_1=1$ (with probability p) and $\sigma_2=10^{-5}$ (with probability $(1-p)$), assigned at random.

The EMPT expression derived by Kirkpatrick [9] to calculate the solid line appearing in Figure A.3 is:

$$\sigma_m = \frac{\varphi}{z-2} + \frac{\theta^{1/2}}{z-2} \quad (\text{A.6})$$

in which z is the number of bonds at each node of the network, and φ and θ are:

$$\varphi = \left\{ \left(\frac{zp}{2} - 1 \right) \sigma_1 + \left(\frac{z(1-p)}{2} - 1 \right) \sigma_2 \right\} \quad (\text{A.7})$$

$$\theta = \left\{ \left(\left(\frac{zp}{2} - 1 \right) \sigma_1 + \left(\frac{z(1-p)}{2} - 1 \right) \sigma_2 \right)^2 + 2(z-2)\sigma_1\sigma_2 \right\} \quad (\text{A.8})$$

in which σ_1 and σ_2 are the two possible conductivities for the bonds in the network, each of them occurring with probabilities p and $p-1$, respectively. Figure A.3 represents the case in which $\sigma_1 \gg \sigma_2$.

A.2.6 Approach of Wu and Liu

The model developed by Wu and Liu [22] to calculate the conductivity of composite materials of any number of phases is also based on the EMPT. The main feature of this model consists of replacing the composite by a homogeneous medium with the effective conductivity of the composite. This homogeneous medium is approximated by a resistor network, in which all resistors are equal. The most relevant assumptions of the model are:

- each constituent phase consists of small particles (such as grains of different sizes and shapes),
- the average size of the particles is much smaller than the dimensions of the sample,
- random distribution of the two (or more) phases in the material, i.e. any specific particle has an equal probability of appearing in any position in the whole sample.

For a two-phase composite the final formula for the effective electronic conductivity is:

$$\sigma_e = \frac{E_1 + \sqrt{E_1^2 + E_2}}{4} \quad (\text{A.9})$$

with:

$$E_1 = 3(V_1\sigma_1 + V_2\sigma_2) - (\sigma_1 + \sigma_2) \quad (\text{A.10})$$

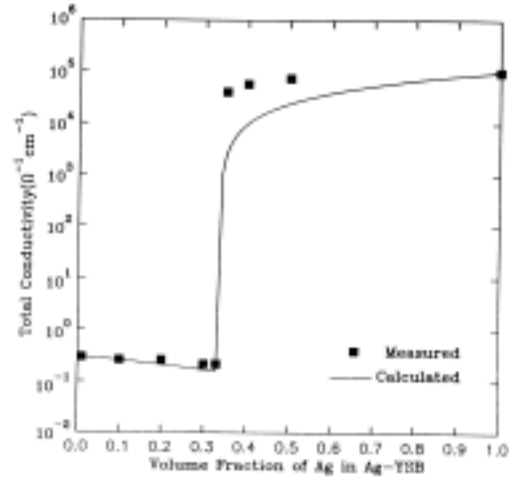
$$E_2 = 8\sigma_1\sigma_2 \quad (\text{A.11})$$

in which σ_1 and σ_2 are the electronic conductivity of phase 1 and 2, respectively, and V_1 and V_2 are the volume fractions of component 1 and 2. Analogous formulae can be

derived for the ionic conductivity of the composite σ_i . In this case σ_1 and σ_2 are the ionic conductivity of phase 1 and 2, respectively. The total conductivity of the composite is defined as follows:

$$\sigma_{\text{total}} = \sigma_e + \sigma_i \quad (\text{A.12})$$

Figure A.4 shows the total conductivity as a function of volume fraction of Ag, for Ag-YSB, in which YSB is yttria-stabilised bismuth oxide. The agreement of the theoretical curve with the experimental data is very good. The deviation of the three points from the theoretical curve may be due to experimental errors.



The critical volume fraction for the most conducting phase V_2 using this network model is found to be $1/3$, independent of the composite material, which is in a very good agreement with experimental V_c values obtained for Ni-YSZ and Ag-YSB among others.

Figure A.4: Total conductivity (theoretical and experimental) of Ag-YSB composite material.

A.3 Conduction and percolation in composite materials

Transport properties of composite materials include, among others, electrical resistivity (conductivity), diffusion constants, and permeability. In the early seventies several authors began to realise that composite materials had percolation properties, such as a percolation threshold, scaling behaviour etc. Therefore, they tried to explain transport properties of such materials by means of percolation theory.

A variety of percolation models have been proposed for describing transport properties of composites. Sahimi [1] and Lux [26] have given an extensive review on these percolation models. In this section it is intended to study the applicability of some of the most relevant discrete and continuum percolation models that exist for

predicting the effective properties (mainly conductivity) of composite media. Furthermore, the concept of critical volume fraction V_c will be explained in detail. It is an important parameter, which tells us about the amount of material necessary for the composite material to percolate.

For an extensive review on the matter, the reader is referred to the work by Ondracek [27]. He strongly emphasizes the importance of the relationship between microstructure and electrical, magnetic and thermal properties of two-phase materials.

A.3.1 Classification of composite materials

In general a system is called *disordered* when its inhomogeneities persist at different length scales. Therefore classical continuum models, in which the properties of the system, namely conductivity, mobility etc, are considered smooth functions of time and space, are not suitable for describing such systems. Composite materials are one example of disordered media consisting of mixtures of two or more phases. They constitute a large class of natural or man-made disordered or heterogeneous systems. Included in this class are: metal-insulator materials, powders, polymers, porous media and granular materials.

A.3.2 Critical volume fraction

The first step on combining percolation theory with physical properties of materials was taken by Scher and Zallen [28]. They proposed, for site percolation problems on a lattice, that p_c is an *invariant* when expressed as a *critical volume fraction* V_c , depending only on dimensionality and not on the details of the lattice structure. The critical volume fraction is the critical content of conductive filler and it is defined as:

$$V_c = p_c f \tag{A.13}$$

The factor f is the filling factor of the lattice when each of its sites is occupied by a hard sphere in such a way that two nearest neighbour spheres touch one another at one point. It is defined as:

$$f = \frac{V_s}{V_c} \quad (\text{A.14})$$

where v_s is the volume of a sphere and v_c is the volume of a unit cell containing one sphere.

The values of V_c are of the order of 0.45 for 2D and of the order of 0.16 for 3D. Furthermore, V_c was also found to be an invariant, within 10% or less, for irregular lattices [23]. For instance, for randomly close-packed (RCP) mixtures of hard spheres, V_c was found to be 0.146 [29], which is a value as close to the average V_c of 0.16 as any of the crystalline structures.

The invariant V_c holds only for percolative systems built up of non-overlapping particles. For example, in 2D, overlapping discs with random centres require a higher area of coverage (of the order of 0.68) in order to percolate [30]. Correspondingly in 3D, overlapping spheres with centres distributed at random have a $V_c = 0.2854$.

In 3D systems built up of overlapping ellipsoids randomly placed in a matrix, it has been proven that V_c depends strongly on the particle shape [31]. Among all ellipsoids of revolution the value of V_c is maximum for spherical particles.

Systems of such permeable anisotropic objects exist in two important areas of applications: porous media and conduction properties in disordered semiconductors [33, 32].

A.3.3 Applications of statistical discrete models

Statistical discrete percolation models are aimed to describe transport properties in materials whose structure can be considered random from a microscopic point of view. A regular (or irregular) network in which sites and bonds are occupied at random describes these structures. For one-phase conducting materials “random” means that there are holes of arbitrary shape randomly distributed in the material. For two-phase composite materials, “random distribution” means that the two phases cannot be identified from their structure, so that they both play a symmetric role.

If the material is represented by a distribution as shown in Figure A.5, the dark particles in the figure may be either one phase or the other in the material.

This implies that any specific particle has an equal probability of appearing in any position of the whole sample. In contrast, uniform distribution means that the same form or pattern of particle distribution is occurring throughout the sample.

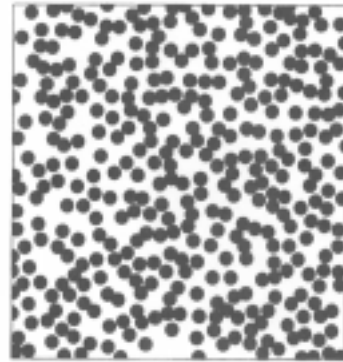


Figure A.5: Computer generated microstructure of a two-phase composite: conducting spheres randomly distributed in an insulating medium.

In this section several models based on classical statistical percolation theory will be presented.

A.3.3.1 Regular network models

As it has been said before, the conduction problem of a continuous medium can be reduced to a lattice network problem. The percolation behaviour of such lattice reduction depends, however, on the nature of the tessellation used to subdivide the volume of the system, which is usually square (2D) or cubic (3D).

Model of Cohen

This model was developed in order to study composite materials. Cohen *et al.* [34] simulated systems with a high V_c using percolation networks of resistors. Examples are thick metal films ('thick' means that the thickness is larger than the length scale over which the random network is macroscopically homogeneous). They are composed of a crystalline metal and a non-metallic phase that is amorphous. They are often called *granular metal films* because studies of their structure show that very thin amorphous layers often surround the metal grains, so that these remain separated. Therefore it is not easy to find clusters of metallic grains in such materials making it difficult to interpret the structures in terms of percolation properties. There are also strong correlations in their structures, so that the random percolation models discussed so far may not be suitable. Examples of these materials are Ni-SiO₂, Al-Si, and Al-Ge.

The model of Cohen *et al.* starts with an initial network already containing a certain fraction, p_0 , of conducting bonds arranged in a configuration of connecting regions that do not contact one another. It replaces at random the non-conducting bonds with conducting ones and calculates the conductivity and the percolation threshold of the system. In this manner correlations are introduced into the model creating a tendency to develop isolated conducting regions. This phenomenon was observed by Abeles [35] in thick films consisting of W or Mo in the insulators Al_2O_3 or SiO_2 . In this case the percolation threshold of the system depends on p_0 , and Cohen *et al.* showed that their model predicts the conductivity data of Abeles *et al.* Due to correlations, V_c is 0.47 for this system, which is considerably higher than the prediction made by Scher and Zaller [28] of $V_c = 0.16$ for a 3D continuum percolation system.

Site-bond percolation model

Many 3D composite systems show a critical volume fraction V_c which is larger than 0.16, the approximate value predicted by site percolation. For example, palladium particles dispersed in yttria-stabilised cubic zirconia matrix (YSZ) have a V_c as high as 0.35-0.40 [5], Ag particles dispersed in YSZ and Ni particles dispersed in YSZ show a V_c of 0.33 [22] (see Figure A.6). The site-bond percolation model can describe this phenomenon.

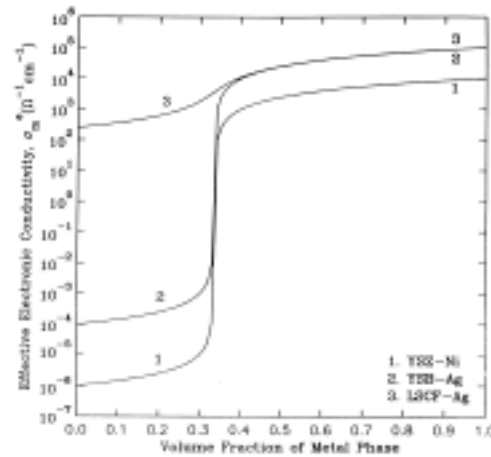


Figure A.6: Conductivity of dense metal-ceramic composites.

It is already known that if all particles occupy a regular lattice and the neighbouring ones are electrically well connected ($P_b = 1$) then $V_c = 0.16$. But in the case that the neighbouring particles are not well connected ($P_b < 1$) the required volume fraction is larger than 0.16. Therefore, compressing conductive mixtures can improve the contacts between the conductive particles, resulting in a relatively low and reproducible value of V_c [4]. In all these cases the conductivity of one phase is much

larger than the other one. Otherwise, there is no percolation phenomenon. Figure A.6 (curve 3) shows that LSCF-Ag does not show a percolation transition because LSCF has an appreciable electronic conductivity compared to Ag.

In regular random network models sites are just points. Therefore, important parameters as size and geometry of the conductive particles are disregarded, although it is known that they have a large influence, for instance, on the critical volume fraction V_c . Continuum models include these parameters and others, like the amount and distribution of the conductive particles in the insulating matrix and interactions between the conductive and insulating components to model the percolative behaviour of the conductivity in composite materials. They will be presented and discussed in the next section.

A.3.4 Applications of statistical continuum models

Many composites possess an irregular structure that cannot be simulated in a very accurate manner by a regular arrangement of sites and bonds, but by a random or regular distribution of inclusions embedded in a matrix. Some examples are powder mixtures of metal and insulator, conducting fibres or ellipsoidal particles in an insulating matrix, etc. Several models have been proposed to study how the conductivity changes with the content of the conductive filler in such composite materials.

A.3.4.1 Geometrical percolation models

Geometric percolation models were proposed to explain the percolation phenomenon in several dry-premixed and subsequently sintered mixtures of conductive and insulating powders. They assume that during the sintering process the insulating particles are deformed into regular cubic particles and the conductive particles are arranged in a regular manner on the surface of these cubic particles (see Figure A.7 further on). The main parameters considered in the geometric models are:

- The non-sintered conducting and insulating particle diameters, if assumptions are made at the stage of the particles in which they are not yet sintered.

- The edge, D , of the sintered insulating cubes formed during sintering and the diameter, d , of the conducting particles, if assumptions are made at the stage of the particles in which they are already sintered (see Figure A.7).

These geometric models are used to study conducting properties of two-phase composite materials showing a very low percolation volume fraction compared with the values predicted by Scher and Zallen [28] for two and three-dimensional systems. This effect is caused by the difference in sizes between the insulator and conducting particles. We have already seen (see Section A.3.3.1) that V_c is of the order of 0.1-0.3 for composite conductors, when metal and insulator particles are comparable in size. But when the metal particles are much smaller, they are forced into regions between the insulating particles and into contact with one another, which results in a lower V_c of the order of 0.01-0.03.

Model of Rajagopal and Satyam

The assumptions of Rajagopal and Satyam [36] are made at the stage of the particles in which they are already sintered and they are valid for a wax/graphite system. For the derivation of their conductivity equation they replace the real material structure by a hypothetical one. In this model the wax particles consist of cubic grains of edge length D , which are formed during sintering. The graphite particles, which are slightly deformed, cover the surfaces of the wax particles and have a diameter d . Figure A.7 shows the elemental cell of this structure.

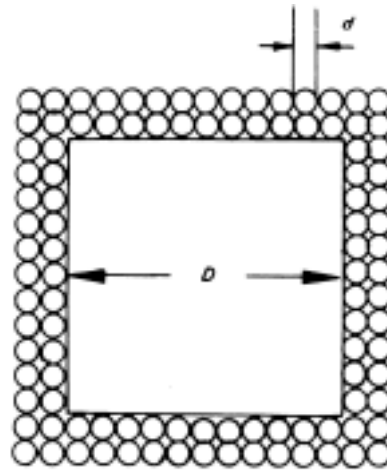


Figure A.7: Cross section of the elemental cell of a composite material according to Rajagopal and Satyam.

The final equation is:

$$\sigma = \sigma_f \frac{2r(V3D - 4d)(3D - 2d)}{D^2 d} \quad (\text{A.15})$$

in which σ is the conductivity of the mixture, σ_f the conductivity of the filler particles (graphite), V the volume fraction of the conductive material, and r is the radius of the contact area between neighbouring conductive particles. This area arises from the fact that the conductive particles are slightly deformed.

Coating model of Malliaris and Turner

The work of Malliaris and Turner [37] was one of the firsts in which the electrical conductivity of a compacted powder of spherical particles was measured, and a clear reference was made to percolation. This model describes a growth mechanism in which it is assumed that both components are initially granular.

The authors prepared powder samples of polyethylene particles of diameter $D = 300 \mu\text{m}$ and nickel particles of diameter $d = 8\text{-}14 \mu\text{m}$. The model assumes that the surfaces of polyethylene particles are coated by nickel particles. The polyethylene particles are assumed to occupy a simple cubic lattice, while the nickel particles occupy a 2D lattice on the spherical surfaces. The critical volume fraction V_c of the nickel phase was found to depend on D/d and it can be calculated from the following expression:

$$V_c = \frac{50p_c}{1 + \frac{\phi D}{4d}} \quad (\text{A.16})$$

in which ϕ is a factor whose value depends on the mode of packing of the Ni spheres, and p_c is the percolation threshold for the nickel particles.

Experimentally it was found that when the radii of the conducting particles is 16 times smaller than those of the isolating ones, the value of V_c begins to drop, and reaches a value of 0.06 when the ratio D/d is 30.

The values of V_c calculated for these mixtures of polymeric and metallic powders using this model are somewhat lower than those observed experimentally [37]. This implies that the assumptions made in this model were not sufficient to predict the percolation concentrations in this type of conductive binary mixtures.

A.3.4.2 Models based on random distribution of elongated particles

Models based on a random distribution of elongated particles were developed to account for the extremely low values found for V_c in some materials, which could not be explained by the models described so far. These models stress the importance of the shape, size and orientation of the filler particles in the percolation phenomena. The main feature of these new models is that they do not use the volume fraction V of material as the critical parameter, providing that it is not a dimensional invariant. In systems in which the filler is composed by elongated overlapping particles, such as rods, ellipsoids, etc., the corresponding V_c value depends on the shape and size of the particles [23, 31-33, 38]. This implies that V is not a good quantity for the prediction of percolation thresholds of such systems.

Excluded volume model

In the case that the filler particles have an elongated geometry, very low values for the critical volume fraction V_c are achieved. The excluded volume model was developed by Carmona *et al.* [39,40] using the original idea about the excluded volume of Balberg *et al.* [41] to describe this effect. They studied the difference in the V_c obtained for carbon particles and for carbon fibres with various length-to-cross-section ratios, dispersed inside a polymeric matrix. The carbon particles have values of V_c of the order of 0.15-0.17, whereas the carbon fibres (r/L of $\approx 1/200$, where r and L are radius and length, respectively) could have a V_c as low as 0.0055. The low V_c associated with the elongated geometry of the particles led to the concept of excluded volume. The excluded volume, V_{ex} , of an object is defined as that volume surrounding and including the given object, which is excluded to another object [31]. This parameter is always defined for a pair of objects. If the excluded volumes of the two conducting fibres overlap, there is a certain probability that they will form a conducting path. A sphere minimises the excluded volume of all convex bodies of finite volume [41] and obeys the expression $V_{ex} = 8v$, in which v is the volume of a sphere. On the other hand a fibre ($L \gg r$) has an excluded volume V_{ex} of $\pi r L^2$ which may be a large value depending on L [6]. For example, the excluded volume formula

gives a V_c of 0.0126 for $r/L = 0.009$ [4]. This value is only slightly higher than the one observed by Carmona *et al.* for graphite fibres with the same r/L value.

Scaled percolation threshold model

When elongated conducting particles in a matrix (or holes in a conducting material) are orientated at random, the excluded volume V_{ex} is not a dimensional invariant anymore although it is found to determine the critical behaviour of the system [41]. For that reason the scaled percolation threshold model was developed. It is based on a new parameter X_c which is a dimensional invariant and, therefore, it depends neither on the shape nor on the orientation of the particles (or holes).

This model was developed by Garboczi *et al.* [23] to explain the conductivity of a 2D-sheet of conducting material in which randomly centred insulating holes were made. Kirkpatrick [9] and Last and Thouless [42] had already studied this problem, when the holes were circles or squares. But in the model of the scaled percolation threshold the holes can be of any shape and orientation. For this V_c strongly depends on the aspect ratio of the particles [31], thus it is not an invariant with respect to the particle shape.

The critical parameter used in this model is X , which is defined as:

$$X = nL_{eff}^2 \quad (A.17)$$

in which n is the number of holes per unit area and L_{eff} is the effective length of the hole, which is electrically determined. For ellipses L_{eff} is $2(a+b)$ and for needles $L+0.68$ [23].

The reason for using this new parameter X is that its correspondent X_c value (see below for definition) was found to be invariant over a quite broad range for the aspect ratio of the holes a/b (see Table A.2). Here a and b are the semi-major and semi-minor axes of the elliptical hole.

a/b	V_c	X_c
1	0.2854	5.6
2	0.2618	5.6
3	0.2244	5.6
4	0.1901	5.5
5	0.1627	5.7
10	0.0870	5.5
20	0.0415	5.4
30	0.0264	5.5
200	0.0032	5.5

Table A.2: Values of V_c , invariant X_c and geometrical data for randomly oriented overlapping ellipsoids of revolution

The invariant which results from the model is X_c , the *scaled percolation threshold*, and it obeys the following expression:

$$X_c = n_c L_{eff}^2 \quad (\text{A.18})$$

in which n_c is the number of holes at percolation threshold.

Conductivity experiments were performed on 2D-conducting sheets with random circular, square and slit-shaped holes on them.

Figures A.8 and A.9 show the results of these experiments, plotting the relative conductivity σ/σ_0 of these 2D-conducting sheets against the new parameter X . σ_0 is the conductivity of the

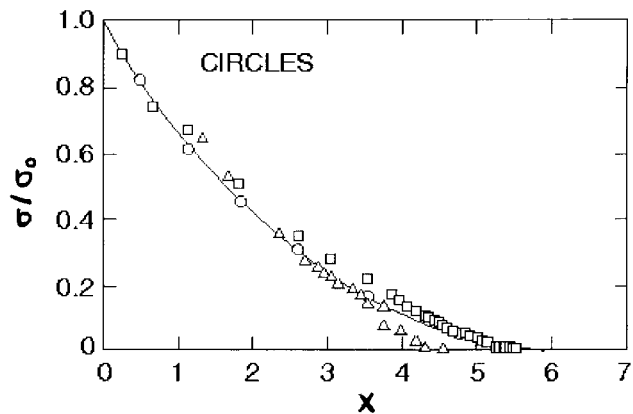


Figure A.8: Relative conductivity vs. $X=nL_{eff}^2$ for circles (or discs). The circles were obtained by computer simulation, the squares and triangles are experimental data.

sheet before any holes are introduced. Solid lines in the graphs represent the universal conductivity curve [23] for holes in 2D, which is calculated from formula (A.19). This formula is a scaling expression, appearing the corresponding scaling exponent $t = 1.3$, which is the typical value for 2D-systems, i.e.,

$$\sigma / \sigma_0 = \left[\left(1 - \frac{X}{5.9} \right) \left(1 + \frac{X}{5.9} - \frac{X^2}{24.97} \right) / \left(1 + \frac{X}{3.31} \right) \right]^{1.3} \quad (\text{A.19})$$

In general, results [4, 39, 40] reveal that, for conducting composites, the critical volume fraction of the conductive filler decreases considerably if it consists of fibres instead of spherical particles. This result is very important because it is always the researcher's goal to use the smallest amount of filler to obtain a percolative (conducting) system. Therefore, if the conducting phase in a composite material can be composed of fibres instead of spheres, fibres would be chosen in order to get the best yield of the material.

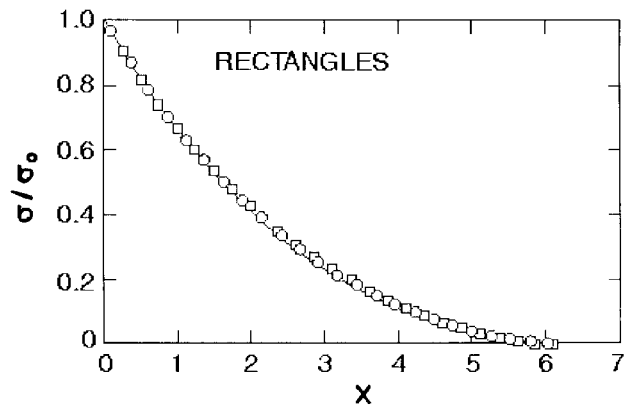


Figure A.9: Experimental relative conductivity vs. $X=nL_{eff}^2$ for squares (represented by squares in the graph) and slits (represented by circles in the graph).

A.4 Conclusions

The main purpose of this work was to summarize the possibilities of percolation theory to describe and interpret transport properties in disordered composite media. From the results of the various models described here, it can be stated that this theory is a powerful tool accounting for the drastic and sudden changes occurring in 'percolative systems'.

The success in modelling disordered media by means of random networks provides a quite simple manner in which complex systems can be studied. Nevertheless, it has to be taken into account that percolation models require a large computational effort to calculate the critical parameters describing the percolation phenomena in these materials. Although the percolation models presented here can describe in each case the particular property under study, it has to be admitted that none of them is able to explain all the different results of experimental studies. Furthermore, none of the

models is able to account for the total influence of different parameters on the percolation phenomena. A good correlation between experimental results and a special percolation model does not necessarily imply the validity of the model, but on the other hand experimental results should be examined with care.

From this study, it can be stated that it is very important to make the right assumptions leading to a not too complicated model, which describes the percolative behaviour of the system. In the case of ceramic composite materials, the assumption of a random distribution of phases occurring within the material, and modelling such a system by means of a regular network give a very accurate description of the conductivity of such materials. For granular metallic films a model, simply based on a regular network in which some correlations are included, provides also an accurate value for the critical volume fraction of the conducting material.

Nevertheless, many questions are still open in this field, and efforts are currently focussed on the investigation of the microstructure of the materials. This implies the necessity of a quantitative analysis of the micro-level structure, which is always difficult and demands sophisticated methods. But it seems to be the most promising way to account for the transport properties of composite materials.

References

- [1] M. Sahimi, G.R. Gavalas and T.T. Tsotsis, 'Statistical and continuum models of fluid-solid reactions in porous media', *Chem. Engin. Sci.* 45 (6), 1443-1502, 1990.
- [2] M. Sahimi, 'Applications of percolation theory', Taylor&Francis, London and Philadelphia, 1994.
- [3] H.L. Scott, 'Percolation processes and co-operative phenomena', *Am. J. Phys.* 40, 1134-1139, 1972.
- [4] C. Chen, 'Fine grained zirconia-metal dual phase composites', PhD Thesis, Royal Library Cataloguing in Publication Data, Den Haag, 1994.
- [5] D. Stauffer, 'Introduction to percolation theory', Taylor&Francis, London and Philadelphia, 1994.
- [6] D.S. McLachlan, M. Blaszkiewicz and R.E. Newnham, 'Electrical resistivity of composites', *J. Am. Ceram. Soc.* 73 (8), 2187-2203, 1990.
- [7] H. Stanley, 'Phase transitions and critical phenomena', Clarendon Press Oxford, 1971.
- [8] C. Domb and M.S. Green, 'Phase transitions and critical phenomena', Academic Press, London New York, 1972.

- [9] S. Kirkpatrick, 'Classical transport in disordered media: scaling and effective-medium theories', *Phys. Rev. Lett.* 27, 1722-1725, 1971.
- [10] V.K.S. Shante and S. Kirkpatrick, 'An introduction to percolation theory', *Advances in Physics*, 20, Ed. by B.R. Coles, Taylor&Francis, London and Philadelphia.
- [11] M. Sahimi, B.D. Hughes, L.E. Scriven and H.T. Davis, 'Critical exponent of percolation conductivity by finite-size scaling', *J. Phys. C: Solid State Phys.* 16, L521-527, 1983.
- [12] D.G. Ast, 'Evidence for percolation-controlled conductivity in amorphous As_xTe_{1-x} films', *Phys. Rev. Lett.* 33 (17), 1042-1045, 1974.
- [13] S. Kirkpatrick, 'Percolation and conduction', *Rev. Mod. Phys.* 45, 574-588, 1973.
- [14] R. Mehr, T. Grossman and N. Kristianpoller, 'Simple percolation experiment in two dimensions', *Am. J. Phys.* 54 (3), 271-273, 1986.
- [15] R.B. Stinchcombe and B.P. Watson, 'Renormalisation group approach for percolation conductivity', *J. Phys. C: Solid State Phys.* 9, 3221-3247, 1976
- [16] H. Ottavi, *J. Phys. C* 11, 1311, 1978.
- [17] P.S. Clarke, J.W. Orton and J. Guest, *Phys. Rev. B* 18, 1813, 1978.
- [18] X. Quan, *J. Polym. Sci. B Polym. Phys.* 25, 1557, 1978.
- [19] S. Etemand, X. Quan and N.A. Sanders, *Appl. Phys. Lett.* 48, 607, 1986.
- [20] T.A. Ezquerro, *Adv. Mater.* 2, 597, 1990.
- [21] L. Benguigui, J. Yacubowicz and M. Narkis, *J. Polym. Sci. B Polym. Sci.* 25, 127, 1987.
- [22] Z. Wu and M. Liu, 'Modelling of ambipolar transport properties of composite mixed ionic-electronic conductors', *Solid State Ionics* 93, 65-84, 1997.
- [23] E.J. Garboczi, M.F. Thorpe, M.S. deVries and A.R. Day, 'Universal conductivity curve for a plane containing random holes', *Phys. Rev. A* 43 (12), 6473-6482, 1991.
- [24] D.A.G. Bruggeman, *Annl. Phys.* 24, 636, 1935.
- [25] R. Landauer, *J. Appl. Phys.* 23, 779, 1952.
- [26] F. Lux, 'Review: models proposed to explain the electrical conductivity of mixtures made of conductive and insulating materials', *J. Mater. Sci.* 28, 285-301, 1993.
- [27] G. Ondracek, 'The quantitative microstructure-field property correlation of multiphase and porous materials', *Rev. Power Metall. Phys. Ceram.* 3, 3&4, 205, 1987.
- [28] H. Scher and R. Zallen, *J. Chem. Phys.* 53, 3759, 1970.
- [29] J.P. Fitzpatrick, R.B. Malt and F. Spaepen, 'Percolation theory and the conductivity of random close packed mixtures of hard spheres', *Phys. Lett. A*, 47 (3), 207-208, 1974.
- [30] E.T. Gawlinski and H.E. Stanley, *J. Phys. A: Marth. Gen* 14, L291, 1981.
- [31] E.J. Garboczi, K.A. Snyder, J.F. Douglas and M.F. Thorpe, 'Geometrical percolation threshold of overlapping ellipsoids', *Physical Review E* 52, 819-828, 1995.
- [32] U. Ahlon, I. Balberg and A. Drory, 'New, heuristic, percolation criterion for continuum systems', *Phys. Rev. Lett.* 66 (22), 2879-2882, 1991.
- [33] A. Drory, U. Ahlon, I. Balberg and B. Berkowitz, 'Analytic derivation of percolation thresholds in anisotropic systems of permeable objects', *Phys. Rev. A* 43 (12), 6604, 1991.
- [34] M.H. Cohen, J. Jortner and I. Webman, *Phys. Rev. B* 17, 4555, 1978.
- [35] B. Abeles, H.L. Pinch and J.I. Gittleman, *Phys. Rev. Lett.* 35, 247, 1975.
- [36] C. Rajagopal and M. Satyam, *J. Appl. Phys.* 49, 5536, 1978.

- [37] A. Maillaris and D.T. Turner, 'Influence of particle size on the electrical resistivity of compacted mixtures of polymeric and metallic powders', *J. Appl. Phys.* 42, 614, 1971.
- [38] Z. Fan, 'A microstructural approach to the effective transport properties of multiphase components', *Phil. Mag A*, 73, No. 6, 1663-1684, 1996.
- [39] F. Carmona, R. Conet and P. Delhaes, 'Piezoresistivity of heterogeneous solids', *J. Appl. Phys.* 61, 2550, 1987.
- [40] F. Carmona, F. Barreau, P. Delhaes and R. Cornet, *J. Phys. Lett.* 41, L531, 1980.
- [41] B. Balberg, C.H. Anderson, S. Aleander and N. Wagner, *Phys. Rev. B: Condensed Matter* B 30, 3933, 1984.
- [42] B.J. Last and D.J. Thouless, 'Percolation theory and electrical conductivity', *Phys. Rev. Lett.* 27, 1719-1721, 1971.

Appendix B

Modelling constant voltage electrophoretic deposition from a stirred suspension

In electrophoretic deposition, a voltage difference is applied across a suspension, and a layer ('cast' or coating) is formed on one of the electrodes. Based on first principles, cast growth is described in this work for a well-stirred suspension, a constant voltage difference across the deposition cell, and a nonionic solution. The influence of cast formation on cast growth is implemented, which is a refinement of the model described in 1999 by Biesheuvel and Verweij. Simulation results are compared with experimental data. From the derivation it follows that a smooth cast layer is formed when the particle permittivity is lower than that of the liquid. Catastrophic cast growth occurs when the particle permittivity is higher than that of the liquid.*

* This chapter has been published in: *AIChE Journal*, **46**, No. 3, 626-631 (2000)

B.1 Introduction

In electrophoretic deposition (EPD) a layer of particles is formed on a conducting substrate under the action of an electric field. EPD has the advantages of a high homogeneity of the final cast, short deposition times and a low surface roughness [1].

EPD is used industrially to apply ceramic, glass or polymer materials as a coating or paint on a substrate of arbitrary shape. Especially important is the application of ceramic layers as paint on metal components in the automotive industry [2]. EPD is used as well to dehydrate suspensions and emulsions [3] and to remove colloidal contaminants from aqueous suspensions (such as removal of coal or clay in water clarification [4]).

Despite its importance, not many articles can be found in the open literature that consider the processing aspects of EPD. Therefore, many aspects of the process are still to be investigated. The aim of this work is to describe the growth velocity of the particle layer ('cast') based on the theory of an earlier article [1] in which a model for EPD was developed for an unstirred suspension while neglecting the influence of the growing cast on the formation rate. An expression for the cast formation rate was obtained that describes the more-than-linear cast growth with increasing suspension concentration, but that does not describe the change of cast growth with time.

In the present article, one-dimensional cast growth at constant voltage EPD from a stirred suspension is considered, including the influence of the growing cast. Both cast and suspension are regarded as dielectric media which is a reasonable assumption for a suspension with a very low concentration of ions (such as organic solvent). On the one hand, the potential drop over the electrostatic double layers that form at the electrodes decreases with decreasing ion concentration (being zero for a dielectricum), while, on the other hand, the formation time of these double layers will increase when the ion concentration in the suspension decreases, because the ionic flux toward the double layer decreases.

When the formation time of the double layers becomes much longer than the time required for cast formation, particle deposition can be considered to take place in a dielectricum. Furthermore, when the ion concentration is decreased, stirring of the suspension will increasingly inhibit net ionic movement to the electrodes, and therefore double layer formation, by the same mechanism as just discussed. These phenomena can be quantified more thoroughly by solving the Nernst-Planck equations together with the Poisson equation and continuity equations for each species [5] while considering macroscale mixing due to stirring using empirical expressions such as those in Refs. [6, 7]. However, this endeavour is not part of the present work.

Reactions at the electrodes (electrolysis) are not considered either, which is reasonable for a sufficiently low voltage difference; at higher voltage differences, electrode reactions can be implemented using the Butler-Volmer equation [5].

Results are presented for a planar and a cylindrical geometry of the deposition cell. From the integrated equation for the field strength, a new criterion arises that predicts under which conditions a smooth cast layer is formed or when catastrophic cast growth occurs.

B.2 Theoretical background

B.2.1 Introduction

In the present paper, *EPD* from a well-stirred suspension consisting of one particle type is described in a two-phase system with a planar geometry (see Figure B.1). The two phases that are present in the deposition cell are cast and suspension. The field between the two electrodes is considered uni-directional (straight field lines, perpendicular to the electrode surfaces); curved flow lines at the edges of the electrodes are not considered. Though a well-stirred suspension is considered, resuspension of particles that have moved into the cast is neglected.

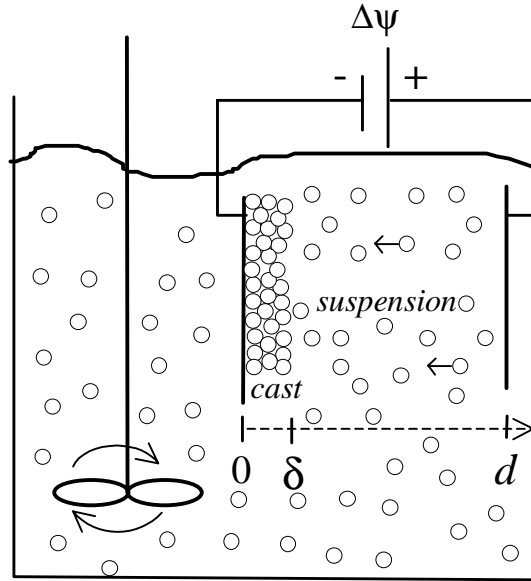


Figure B.1: EPD from a stirred suspension.

B.2.2 Cast-suspension boundary

The cast growth rate u_c is given by a mass balance over the moving cast [1]:

$$u_c = \frac{d\delta}{dt} = -v_s \frac{\phi_s}{\phi_c - \phi_s} \quad (\text{B.1})$$

with δ the cast thickness, t time, v_s the velocity of particles in the suspension at the suspension-cast boundary, ϕ_s the volumetric particle concentration in the suspension and ϕ_c the cast packing factor (unity minus porosity). Here, it is assumed that the cast does not densify in time, which is a reasonable assumption if a dispersed suspension is used [8].

B.2.3 Particle Mass Balance

For a stirred suspension, concentration gradients $\nabla\phi_s$ will not form and ϕ_s is given by an overall mass balance for the particles in the suspension:

$$\frac{d(\phi_s V)}{dt} = \phi_s \frac{dV}{dt} + V \frac{d\phi_s}{dt} = -S u_c \phi_c \quad (\text{B.2})$$

Here, V is the volume of the suspension and S is the electrode surface area. We have assumed that the mass density of the liquid and the particles is constant. To solve equation (B.2) an overall mass balance for the entire suspension phase must be set up:

$$\frac{dV}{dt} = -S u_c \quad (\text{B.3})$$

Incorporation of equation (B.3) in equation (B.2) results in:

$$\frac{d\phi_s}{dt} = -\frac{S}{V} u_c (\phi_c - \phi_s) \quad (\text{B.4})$$

B.2.4 Particle Velocity

The velocity v_s of a suspended particle in an electric field E is given by [9]:

$$v_s = \mu E \quad (\text{B.5})$$

Ordinary diffusion as a means of particle transport in the suspension phase has been left out of equation (B.5) because gradients $\nabla\phi_s$ will not form in the suspension. Note that the convective motion due to the stirring of the suspension becomes parallel to the cast surface when it is approached. Therefore, stirring does not change the component of v_s that is perpendicular to the cast as considered in equation (B.5), which is the component that adds to the cast growth. By choice a positive mobility μ and a negative electric field E are chosen to comply with the system represented schematically in Figure B.1. This results in a negative particle velocity in the suspension v_s and a positive cast growth u_c .

B.2.5 Mobility

The mobility μ of a charged colloidal particle follows from the simultaneous solution of the Poisson equation with the Navier-Stokes equations and conservation of ions [10]. For a single particle immersed in an infinitely extended pure liquid, the analytical solution is the Henry equation [9,11]:

$$\mu = \frac{2\varepsilon_r\varepsilon_0\zeta f_1(\kappa r_p)}{3\eta} \quad (\text{B.6})$$

Here, ε_r is the relative permittivity, ε_0 the permittivity of vacuum ($\varepsilon_0=8.854\times 10^{-12}$ F/m), ζ the zeta-potential (V), κ is the inverse of the Debye screening length (m^{-1}), r_p the particle radius (m) and η the (Newtonian) viscosity (Pa.s). The function f_1 varies between 1.0 at $\kappa r_p = 0$, (Debye-Hückel equation) and 1.50 at $\kappa r_p = \infty$ (Helmholtz-Smoluchowski equation). For a concentrated suspension, an analytical solution exists [12] in which the mobility does not depend on the permittivity of the particles. As this expression is not verified experimentally yet, we will use a more simple approach based on qualitative arguments: if the Debye screening length is low compared to the average distance between particles x ($x\cdot\kappa \gg 1$), the potential drops to zero before a ‘new’ particle is encountered, so the pure liquid permittivity ε_L can be used. However, for $x\cdot\kappa \ll 1$, many particles are present within the Debye length of the particle under study so it is reasonable to use the effective permittivity of the suspension as a whole ε_s . The average interparticle distance x follows from the particle radius r_p and the volumetric suspension concentration ϕ_s assuming a certain particle structure in the suspension. The closed-packed structure (either cubic or hexagonal [13]) is most appropriate as in this case x is the largest of the possible packing structures and charged particles (of the same charge, as in *EPD*) naturally tend to maximize the interparticle distance. Now, the interparticle distance x (along the line connecting the centers of the particles) is given by:

$$x = 2r_p \left(\left(\frac{\pi\sqrt{2}}{6\phi_s} \right)^{1/3} - 1 \right) \quad (\text{B.7})$$

The Debye screening length for a fully dissociated symmetrical salt is given by [11]:

$$\kappa^{-1} = \left(\frac{\varepsilon_r\varepsilon_0RT}{2F^2z^2c} \right)^{1/2} \quad (\text{B.8})$$

Here, R is the gas constant (8.3144 J/molK), F Faraday's constant (9.65×10^4 C/mol), z the charge number and c the concentration of either the negative or the positive charged particles (mol/m^3).

B.2.6 Effective Permittivity

The effective permittivity of a particle-liquid (two-phase) medium depends on the volume fraction of particles and is different for the cast and the suspension. Here, the Clausius-Mossoti approach [14] is used:

$$\varepsilon = \varepsilon_h \frac{\varepsilon_f + 2\varepsilon_h + 2\phi_f(\varepsilon_f - \varepsilon_h)}{\varepsilon_f + 2\varepsilon_h - \phi_f(\varepsilon_f - \varepsilon_h)} \quad \phi_f < 0.45 \quad (\text{B.9})$$

Host h and filler f must be chosen to comply with $\phi_f < 0.45$ (according to the figures in Sareni et al. [14]). For the suspension (e.g., $\phi_s = 0.20$) this implies that the liquid is the host ($\varepsilon_h = \varepsilon_L$), the particles are the filler ($\varepsilon_f = \varepsilon_p$) and $\phi_f = \phi_s$. For the cast (e.g., $\phi_c = 0.6$), this changes to $\varepsilon_h = \varepsilon_p$, $\varepsilon_f = \varepsilon_L$ and $\phi_f = 1 - \phi_c$.

B.2.7 Field strength

Electrostatics starts with the Maxwell equations and for the subject under study we confine ourselves to Coulomb's law [15]:

$$\nabla \cdot \mathbf{D} = \rho \quad (\text{B.10})$$

Here \mathbf{D} is the displacement vector, given by $\mathbf{D} = \varepsilon \cdot \mathbf{E}$ and ρ the charge density [C/m^3]. Because SI-units (rationalized or MKSA system) are used here, the factor 4π is left out of equation (B.10). Together with the definition equation:

$$\nabla \psi = -\mathbf{E} \quad (\text{B.11})$$

the electrostatics of *EPD* are described. Here ψ is the electrical potential. From this point forward, a one-dimensional planar system with parallel electrodes and particles moving along only one axis is considered (see Figure B.1). Therefore, vectors \mathbf{D} and \mathbf{E} can be simplified to the scalars D and E . To solve the electric field throughout the

deposition cell, equation (B.10) is used first to determine the change in field strength E over the cast-suspension boundary. It is assumed that no charge is present in the boundary and therefore D becomes independent of location, which results in:

$$\epsilon_c E_c = \epsilon_s E_s \quad (\text{B.12})$$

Second, both the permittivity of the cast ϵ_c and of the suspension ϵ_s are considered independent of place, which reduces equation (B.10) to:

$$\nabla E = \frac{\rho}{\epsilon} \quad (\text{B.13})$$

Together with equation (B.11) the well-known Poisson equation is obtained:

$$\nabla^2 \psi = -\frac{\rho}{\epsilon} \quad (\text{B.14})$$

A simplification of the Poisson equation can be made if the (net) charge density ρ is zero in the entire system. This is true at the start of the process when suspended particles as well as all ions are homogeneously distributed over the entire suspension and is valid as well for a pure non-electrolyte (dielectric medium or non-ionic solution). Possibly, as a first approximation, oxidic particles in an organic solvent can be modelled as a pure non-electrolyte during the entire *EPD* process. The charges at the particle surface and in the surrounding cloud are then neglected in the calculation of the field E . In this case, both cast and suspension are regarded as dielectric media, and the Poisson equation simplifies to the Laplace equation:

$$\nabla^2 \psi = 0 \quad (\text{B.15})$$

Assuming that equation (B.15) is valid within each phase and taking into account equation (B.12) at the cast-suspension boundary, solution for the field strength E_s in the suspension at the cast-suspension boundary results in:

$$E_s = \frac{-\Delta\psi}{\left(\frac{\epsilon_s}{\epsilon_c} - 1\right)\delta + d} \quad (\text{B.16})$$

Here $\Delta\psi$ denotes the voltage difference $\psi_d - \psi_0$ over the electrode distance d and ϵ_s and ϵ_c represent the effective permittivities of suspension and cast respectively, which are calculated with the Clausius-Mossoti equation (B.9).

B.2.8 Cylindrical substrate

To describe cast formation on cylindrical substrates (such as on wires), the preceding set of equations is still valid, but equation (B.16) changes to:

$$E_s = -\Delta\psi \left\{ (a + \delta) \left(\frac{\epsilon_s}{\epsilon_c} \ln \left(\frac{a + \delta}{a} \right) + \ln \left(\frac{b}{a + \delta} \right) \right) \right\}^{-1}$$

Here, a is the radius of the substrate and b the radial coordinate of the counter electrode ($b > a$). Furthermore, the surface area at which deposition takes place depends on the cast thickness by $S = \ell 2\pi(a + \delta)$ with ℓ the length of the substrate.

B.3 Results and Discussion

B.3.1 Analytical expressions

The set of equations (B.1), (B.3)-(B.6), (B.9) and (B.16) describes *EPD* on a flat substrate. The initial conditions for the three differential equations are:

$$\psi|_{t=0} = \psi_0 \quad \phi_s|_{t=0} = \phi_{s,0} \quad \delta|_{t=0} = 0$$

For $\kappa r_p \ll 1$ and $x \cdot \kappa \ll 1$ (see below), the Debye-Hückel equation for particle mobility μ can be used as well as the effective suspension permittivity ϵ_s :

$$\mu = \frac{2\epsilon_s \zeta}{3\eta} \tag{B.17}$$

Only numerical solutions can be found for this coupled set of differential equations but an explicit solution is obtained if the suspension volume V is large enough that the suspension concentration remains constant, i.e. $\phi_s = \phi_{s,0}$. In that case, combination of equations (B.1), (B.5), (B.16) and (B.17) results in:

$$\delta = \frac{\epsilon_c}{\epsilon_s - \epsilon_c} \left(\sqrt{d^2 + \frac{4(\epsilon_s - \epsilon_c)\epsilon_s \zeta \phi_s \Delta \psi t}{3\epsilon_c \eta (\phi_c - \phi_s)}} - d \right) \quad (\text{B.18})$$

A further simplification of equation (B.18) can be made if the second group in the square root is small compared to d^2 which results in:

$$\delta = \frac{2\epsilon_s \zeta \phi_s \Delta \psi t}{3\eta (\phi_c - \phi_s) d} \quad (\text{B.19})$$

For a dilute suspension ($\phi_s \ll \phi_c$; $\epsilon_s = \epsilon_L$), equation (B.19) becomes:

$$\delta = \frac{2\epsilon_L \zeta \phi_s \Delta \psi t}{3\eta \phi_c d} \quad (\text{B.20})$$

This equation is equivalent to Hamaker's law [1,16]. An explicit expression incorporating dilution can be obtained for low enough suspension concentrations ϕ_s . In that case, cast growth neither influences the field strength in the suspension E_s nor the volume of suspension V while the permittivity of the suspension ϵ_s equals ϵ_L . The field strength in the suspension E_s now simplifies to $E_s = -\Delta\psi/d$ and the mobility μ becomes independent of time: $\mu = 2\epsilon_L \zeta / (3\eta)$. Combination of equations (B.1) and (B.4) results in:

$$\frac{d\phi_s}{dt} = \frac{S}{V_0} v_s \phi_s \quad (\text{B.21})$$

Equation (B.21) is integrated and the result implemented in equation (B.1). If the assumption $\phi_s \ll \phi_c$ is made, the following expression is obtained:

$$\delta = \frac{V_0}{S} \frac{\phi_{s,0}}{\phi_c} \left\{ 1 - \exp \left\{ -\frac{S}{V_0} \frac{\mu \Delta \psi t}{d} \right\} \right\} \quad (\text{B.22})$$

For $\frac{S}{V_0} \frac{\mu \Delta \psi t}{d} \ll 1$, equation (B.22) will result in equation (B.20).

B.3.2 Comparison with experiments

Several authors measured the decreasing cast growth in time for constant-voltage EPD ([3, 17-25]) but only Zhang *et al.* [22] give enough information to test our equations.

$\phi_{s,0}$	0.00276
ϕ_c	0.60
ρ_p	3624 kg/m ³ *
S/V_0	300 m ⁻¹
ϵ_L	27.71· ϵ_0
ϵ_p	10.14· ϵ_0 *
ζ	4.45 mV
η	9.24×10 ⁻⁴ Pa.s
$\Delta\psi$	50 V
d	0.025 m

Table B.1: Data used by Zang *et al.* [22]. * Volume averages for the components ZrO₂ and SiC, based on data from Lide [26].

To evaluate the data in Zhang's figure 4 (Table B.1, third row), we first evaluated the value of $x\cdot\kappa$ and $\kappa\cdot r_p$, see equations (B.7) and (B.8). To this end, the autoprotolysis constants from Coetzee and Ritchie [27] for methanol and 2-propanol are used (pK = 16.7 and 20.8, respectively) which results in a volume-averaged concentration c of 3.44×10^{-6} mol/m³ ($c = 10^{3-pK/2}$) and a value of $\kappa^{-1} = 3081$ nm. With $x = 436$ nm, $x\cdot\kappa = 0.14$ and $\kappa\cdot r_p = 0.013$ follow, so equation (B.17) is used.

Calculations based on the numerical model (or on equation (B.22) as ϕ_s is very low) using the data from Table B.1 and $Weight = S\phi_c\rho_p\delta$ are best fitted to the experimental data using $S = 520$ cm², see Figure B.2. However, the quality of the fit is moderate and this value for the surface area seems large when considering the set-up as drawn in figure 1 of Zhang *et al.* [22].

If we multiply the value for the ζ -potential by 4π (corresponding to the conversion of the esu/emu/Gaussian/cgs-system to the SI/MKSA/rationalised system [28]), measurements can be fitted much better and with a more reasonable electrode surface

area of S of 84 cm^2 . Note that the resulting ζ -potential (56 mV) is more in accordance with typical ζ -potentials measured by other authors ($\sim 30 - 200 \text{ mV}$ [24, 29]). That Zhang *et al.* [22] work in a Gaussian unit system is further emphasized by the fact that they also use a factor 4π in their expression for the cast growth.

The numerical model and the explicit equation B.22 give the same results because the suspension concentration and final cast thickness are extremely low (see Figure B.2). The explicit expressions (B.18)-(B.20) do not consider the dilution of the suspension and therefore violate the overall mass balance for times over $\sim 200 \text{ s}$.

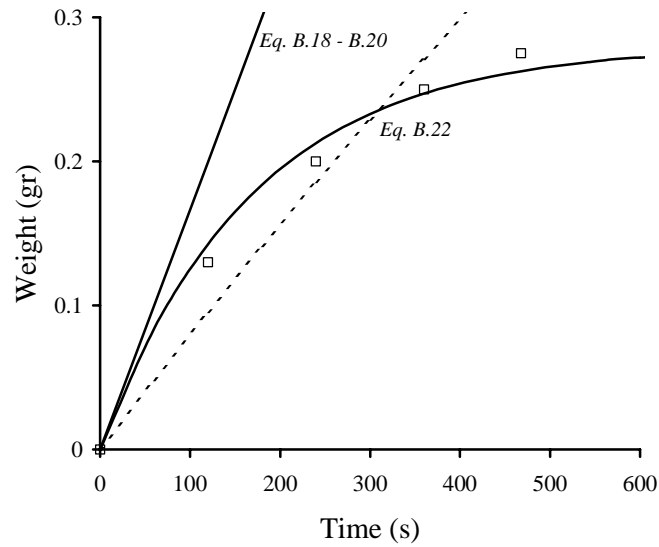


Figure B.2: Weight increase of cast formed by *EPD*. Dots are measurements by Zhang *et al.* (1994), dashed line the best fit based on $\zeta=4.45 \text{ mV}$ and $S=520 \text{ cm}^2$ (eq. B.22) and solid lines based on $\zeta = 55.9 \text{ mV}$ and $S = 84 \text{ cm}^2$. Other data from Table B.1.

To show the differences between the numerical model and the explicit expressions more clearly, simulations were made with an initial suspension concentration that was increased 100 times ($\phi_{s,0} = 0.276$), (see Figure B.3). Now the explicit solutions significantly deviate from the numerical model: the initial cast growth rate is significantly lower for equations (B.20) and (B.22) than for the numerical model as the equations do not properly implement the mass balance over the growing cast. For $t > 100 \text{ s}$, equations (B.18)-(B.20) overestimate the cast thickness because they neglect the dilution of the suspension.

Other authors also modelled the decrease in cast growth rate in time and attributed this to the ‘resistance’ of the cast [29], to depletion of the suspension [22, 30], or to both [24]. These models make an error with respect to Kynch theory (that is, implicitly assume that $\phi_s \ll \phi_c$ in equation (B.1)) and assume that neither the particle mobility μ nor the suspension volume V change in time. Furthermore, it is unclear how the concept ‘resistance’ relates to the more fundamental properties as particle and liquid permittivity and system geometry (such as planar vs. cylindrical).

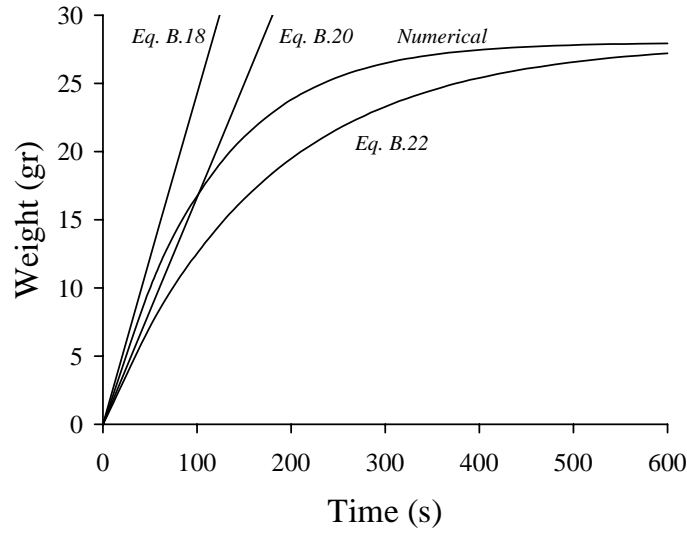


Figure B.3: Simulation results using data from Table B.1, $S = 84\text{cm}^2$, but $\phi_{s,0} = 0.276$ and $\zeta = 55.9\text{ mV}$.

B.3.3 Uniformity of cast thickness

EPD is often used because a cast with a uniform thickness can be obtained (that is, a smooth surface). Still, finding recipes that result in smooth cast surfaces is often more art than science and a clear explanation based on first principles is lacking. However, this phenomenon is explained by equation (B.16). If we assume $\{\epsilon_c < \epsilon_s\}$, clearly a locally larger δ results in a decreasing magnitude of E and therefore less deposition. This results in smoothing of the cast surface. The inequality $\{\epsilon_c < \epsilon_s\}$ holds for $\{\{\epsilon_p < \epsilon_L\}$ and $\{\phi_c > \phi_s\}\}$, see equation (B.9), and is equivalent to $\{\epsilon_p < \epsilon_L\}$, because $\{\phi_c > \phi_s\}$ holds by definition. However, equation (B.16) also predicts that for

$\{\epsilon_c > \epsilon_s\}$, any (naturally occurring) slight variation in cast thickness will be increased to result in an extremely rough surface with particles only depositing on the highest cast 'peaks'. The resulting structure may easily collapse with particle clumps 'dripping' [31] from the electrode due to gravity, without forming a cast layer.

The criterion for uniform deposition is therefore $\{\epsilon_p < \epsilon_L\}$, which can be validated by the following measurements:

- Krishna Rao and Subbarao [31] note that deposition of β -alumina occurs in media with permittivities ϵ_L in the range of only 12 - 25 (implying that 25 is not an upper limit). The permittivity of alumina is, according to Lide [26], $9.34 < \epsilon_p < 11.54$ which is indeed just below the lower limit for the range of appropriate ϵ_L values.
- In their table 1, Krishna Rao and Subbarao [31] show that magnesia ($\epsilon_p = 9.65$ [26]) is not deposited in dichloromethane ($\epsilon_L = 9.08$) but is in benzyl alcohol ($\epsilon_L = 13$) and liquids with higher ϵ_L .
- Ishihara *et al.* [23] report anomalous deposition of yttria-stabilised zirconia films from 3-pentanone ($\epsilon_L = 15.4$) but uniform deposition in cyclohexanone ($\epsilon_L = 18.3$) and other liquids with higher ϵ_L , which is in agreement with the above criterion if ϵ_{YSZ} is in between 15.4 and 18.3. Accurate values for ϵ_{YSZ} do not exist, also because they depend on the crystallinity of the powder [32], but for (calcium-stabilised) zirconia values between 13.5 and 26 are reported by Thompson *et al.* [32]. At least, this range of values does not contradict the criterion.

B.4 Conclusions

Based on the assumption of zero charge in the entire system (as for suspensions in non-ionic liquids), equations are derived from first principles to describe cast formation during constant voltage electrophoretic deposition on flat and cylindrical substrates. The equations describe experiments from literature on the decrease of cast formation rate with time and indicate that only if the particle permittivity ϵ_p is lower

than the liquid permittivity ϵ_L ($\epsilon_p < \epsilon_L$) smooth layers are obtained. For $\epsilon_p > \epsilon_L$, anomalous cast growth occurs without uniform deposition.

References

- [1] P.M. Biesheuvel and H. Verweij, 'Theory of cast formation in electrophoretic deposition', *J. Am. Ceram. Soc.* 82, 1451-1455, 1999.
- [2] J. Holland and R. Berger, 'Electrophoretic deposition: a new answer to old questions', *Plat. Surf. Finish.* 8, 1993.
- [3] S.N. Heavens, 'Electrophoretic deposition as a processing route for ceramics', *Advanced Ceramic Processing and Technology*, J.G.P. Binner Ed., Noyes, Park Ridge, NJ, 255-283, 1990.
- [4] T.J. Johnson and E.J. Davis, 'An analysis of electrophoresis of concentrated suspensions of colloidal particles', *J. Colloid Interface Sci.* 215, 397-408, 1999.
- [5] W.D. Murphy, J.A. Manzanares, S. Mafé and H. Reiss, 'A numerical study of the equilibrium and nonequilibrium diffuse double layer in electrochemical cells', *J. Phys. Chem.* 96, 9983, 1992.
- [6] M. Kaminoyama, K. Ariai and M. Kamiwano, 'Numerical analysis of power consumption and mixing time for a pseudoplastic liquid in geometrically similar stirred vessels with several kinds of plate-type impellers', *J. Chem. Eng. Jap.* 27, 17, 1994.
- [7] M. Zoklarnik and H. Judat, 'Stirring', *Ullmann's Encyclopedia of Industrial Chemistry B2*, 5th Ed., Chap. 25, VCH Verlag, Weinheim, Germany, 1988.
- [8] L. Bergström, C.H. Schilling and I.A. Aksay, 'Consolidation behaviour of flocculated alumina suspensions', *J. Am. Ceram. Soc.* 75, 3305-3314, 1992.
- [9] R.J. Hunter, 'Foundations of colloid science', Vol. 1, 1st Ed., Clarendon Press, Oxford, 1987.
- [10] W.B. Russel, D.A. Saville and W.R. Schowalter, 'Colloidal dispersions', Cambridge University Press, Cambridge, 1989.
- [11] R.F. Probstein, 'Physicochemical hydrodynamics, an introduction', Butterworths, Boston, 1989.
- [12] H. Ohshima, 'Electrophoretic mobility of spherical colloidal particles in concentrated suspensions', *J. Colloid Interface Sci.* 188, 481-485, 1997.
- [13] D.F. Shriver, P.W. Atkins and C.H. Langford, 'Inorganic chemistry', Oxford University Press, Oxford, UK, 1994.
- [14] B. Sareni, L. Krähenbühl, A. Beroual and C. Brosseau, 'Effective dielectric constant of periodic composite materials', *J. Appl. Phys.* 80, 1688-1696, 1996.
- [15] A.T. Fromhold, 'Theory of metal oxidation', Vol. 1, Fundamentals, North-Holland Publishing Company, Amsterdam, 1976.
- [16] H.C. Hamaker, 'Formation of a deposit by electrophoresis', *Trans. Faraday Soc.* 36, 279-287, 1940.
- [17] A.I. Avgustinik, V.S. Vigdergauz and G.I. Zhuravlev, 'Electrophoretic deposition of ceramic masses from suspensions and calculation of deposit yields', *J. Appl. Chem. USSR (Engl. Transl.)*, 35, 2090-2093, 1962.

- [18] V.A. Malov, I.A. Kalminskaya, V.I. Bezruk, A.N. Lazarev and I.S. Lavros, 'Effect of electric-field nonuniformity on the laws of electrophoretic deposition', *Colloid J. (USSR) (Engl. Transl.)*, 36, 348-351, 1974.
- [19] R.K. Das, H.S. Ray and S. Chander, 'Electrophoretic deposition of titanium dioxide from aqueous suspensions', *Trans. Indian Inst. Metals* 32, 364-368, 1979.
- [20] R. Nass, W. Storch, H. Schmidt, F. Harbach, R. Neeff and H. Nienburg, 'Electrophoretic deposition of alumina from non-aqueous dispersion', *Ceramic Powder Processing Science*, H. Hausner, G. L. Messing and S. Hirano Eds., Deutsche Keramische Gesellschaft, 625-632, 1989.
- [21] Y. Hirata, A. Nishimoto and Y. Ishihara, 'Forming of alumina powder by electrophoretic deposition', *J. Ceram. Soc. Jpn., Int. Ed.*, 99, 105-109, 1991.
- [22] Z. Zhang, Y. Huang and Z. Jiang, 'Electrophoretic deposition forming of SiC-TZP composites in a nonaqueous sol media', *J. Am. Ceram. Soc.* 77, 1946-1949, 1994.
- [23] T. Ishihara, K. Sato and Y. Takita, 'Electrophoretic deposition of Y₂O₃-stabilised ZrO₂ electrolyte films in SOFC', *J. Am. Ceram. Soc.* 79, 913-919, 1996.
- [24] P. Sarkar and P.S. Nicholson, 'Electrophoretic deposition (EPD): mechanisms, kinetics and application to ceramics', *J. Am. Ceram. Soc.* 79, 1987-2002, 1996.
- [25] I. Hector and R. Clasen, 'Electrophoretic deposition of compacts from clay suspensions', *Ceram. Eng. Sci. Proc.* 18, 173-186, 1997.
- [26] D.R. Lide, *CRC Handbook of Chemistry and Physics*, CRC Press, Boca Raton, Florida, 1994.
- [27] J.F. Coetzee and C.D. Ritchie, 'Solute-solvent interactions', 1st Ed., Marcel Dekker, NY, 1969.
- [28] J.D. Jackson, 'Classical electrodynamics', 2nd Ed., Wiley, New York, 1975.
- [29] A. Sussman and T.J. Ward, 'Electrophoretic deposition of coatings from glass-isopropanol slurries', *RCA Review* 42, 178-197, 1981.
- [30] J. Laubersheimer, H.J. Ritzhaupt-Kleissl, J. Hausselt and G. Emig, 'Electrophoretic deposition of sol-gel ceramic microcomponents using UV-curable alkoxide precursors', *J. Eur. Ceram. Soc.* 18, 255-260, 1998.
- [31] D.U. Krishna Rao and E.C. Subbarao, 'Electrophoretic deposition of magnesia', *Ceram. Bull.* 58, 467-469, 1979.
- [32] D.P. Thompson, A.M. Dickens and J.S. Thorp, 'The dielectric properties of zirconia', *J. Materials Sci.* 27, 2267-2271, 1992.

Summary

This thesis deals with the solid oxide fuel cell (SOFC), which is currently at the forefront of environmental-friendly energy systems for this century. SOFCs directly convert chemical energy into electrical energy with high efficiency and low emission of pollutants. The emphasis in this work is on the SOFC anode, in particular its chemistry and development aspects. The hydrogen oxidation reaction at the state-of-the-art nickel/yttria-stabilised zirconia cermet anode was studied. Alternative anode materials – specifically perovskite and fluorite-type of materials - were tested in a hydrogen/water-vapour ambient. The overall aim was to obtain more insight into the properties of different anode systems, thus facilitating further improvement.

The electrodes were characterised electrochemically by polarisation measurements (I - η) and by electrochemical impedance spectroscopy as function of T , p_{H_2} and $p_{\text{H}_2\text{O}}$. In certain cases the electrode impedance was also measured as function of bias (polarisation). The microstructure of the electrodes was investigated by scanning electron microscopy (SEM).

A general introduction on SOFC is presented in **Chapter 1**. The principles and materials employed are described. An overview is given on alternative anode materials that are currently being investigated.

Chapter 2 is a model study in which a porous nickel layer electrode is compared with a modified nickel layer electrode. The modification consists of the deposition of fine yttria-stabilised zirconia (YSZ) particles on the nickel surface. The marked similarity in the electrode properties of nickel and modified nickel in the hydrogen oxidation strongly suggests that essential steps in the electrode mechanism on both types of electrodes are similar. The total electrode conductivity increases with increasing triple phase boundary (TPB) length. However, at similar TPB length the electrode conductivity of the modified porous nickel electrode is about 50% higher compared with that of the bare nickel electrode. This result indicates that the presence of fine YSZ particles on the nickel electrode surface creates additional active sites at which the electrode reaction can occur.

The kinetics of the hydrogen oxidation reaction at the Ni/YSZ anode is investigated in **Chapter 3** using the approach originally used by Epelboin in 1970 to obtain an expression for the impedance. On the basis of the work reported, it is reasonable to conclude that charge transfer processes dominate the hydrogen oxidation kinetics occurring at the Ni/YSZ anode. The characteristic inductive loop at low frequencies in the experimental impedance spectra can be reproduced by assuming that two consecutive reaction steps govern the surface coverage of intermediate OH⁻ groups. More advanced reaction schemes must be invoked to fully explain the experimental observations.

Alternative anode materials have been tested in **Chapters 4** and **5** for use as porous anodes in SOFC applications. In particular two types of lanthanum based chromite-titanates have been studied. They were stable under reducing conditions and measurements were reproducible with different samples of the same composition. The calcium- or strontium- substituted chromium-rich materials, with composition $\text{La}_{0.7}\text{A}_{0.3}\text{Cr}_{0.8}\text{Ti}_{0.2}\text{O}_{3-\delta}$ (A = Ca, Sr), showed p-type conductivity under reducing conditions. The titanium-rich composition, $\text{La}_{0.7}\text{Ca}_{0.3}\text{Cr}_{0.2}\text{Ti}_{0.8}\text{O}_{3-\delta}$, showed n-type conductivity. Both type of materials were active electrodes in a H₂/H₂O gas mixture at 850°C. The electronic conductivity becomes an important limiting factor when the electrode thickness is reduced from 100 μm to 20 μm. The high frequency ‘cut-off’ resistance showed a significant dependence on $p\text{O}_2$, similar to that found for the electronic conductivity. This effect could be ascribed to a limiting sheet resistance of the electrodes. The total electrode resistance of the electrodes was about a factor 10 higher than that of the state-of-the-art Ni/YSZ anode.

Hydrogen oxidation was studied for screen-printed cermet anodes composed of nickel metal and yttria-stabilised zirconia, with additions of 5 and 10 mol% titania. The impedance spectra at open circuit potential indicated the presence of three different processes at applied H₂/H₂O ratios and temperatures. The measurements revealed a similar behaviour as functions of H₂ and H₂O partial pressures for the cermets with 5 and 10 mol% titania. The total electrode resistance increases with increasing the sintering temperature of the cermets from 1300°C to 1400°C. Contrary to earlier

observations made for Ni/YSZ, the results showed that for the Ti-containing cermets the electrode resistance decreases with time. A remarkable result of this study is that these Ti-containing cermets, which have not been optimised yet, show a very good performance at 850°C.

Appendix A summarises the possibilities of percolation theory to describe and interpret transport properties in disordered composite media. Percolation properties play a key role in SOFC cermet electrodes. In these electrodes, ceramic and metal phases and pores have to form a completely percolative system.

And last, a model for electrophoretic deposition is presented in **Appendix B**, for a well-stirred suspension under a constant voltage difference. Based on first principles, the cast growth is described. The influence of the cast formation on the cast growth is implemented. Electrophoretic deposition is an interesting technique for depositing advanced ceramic materials for SOFC applications.

Concluding remarks:

New mixed conducting anode materials studied in this thesis, by no means optimised, showed a good stability and were found to be reproducible. They were active in H₂/H₂O mixtures at 850°C. Nevertheless the electronic conductivity of these perovskites is too low, resulting in electrode conductivities a factor 10 lower than that of the state-of-the-art Ni/YSZ cermets. The Ti-doped YSZ / Ni composites show excellent anode performance in H₂/H₂O mixtures at 850°C, comparable to that of the state-of-the-art Ni/YSZ cermets, and an improved performance with time. There are strong indications that the ceramic phase is active in the electrode reaction. It can be concluded that composites present the best alternative for improved anodes, when compared to single-phase materials. It is essential to combine the best properties of different materials to achieve high performance.

Another conclusion from this research is that it is difficult to avoid Ni when excellent performance is wanted. When hydrocarbons are used as direct fuel, Ni must be replaced by another electronic conductor because of the severe carbon deposition problems. Hence further research should be focused on composites of mixed

conducting ceramics and highly electronic conductors. Such research will necessarily include a study of the chemistry of layer formation, in order to optimise the microstructure of these composite anodes.

Samenvatting

Dit proefschrift gaat over de vaste-stof-brandstofcel (solid oxide fuel cell, SOFC), die op dit ogenblik een belangrijke positie inneemt tussen de milieuvriendelijke energiesystemen voor deze eeuw. SOFCs zetten chemische energie direct om in elektrische energie met een hoog rendement, in combinatie met een lage uitstoot van broeikasgassen. In dit proefschrift wordt speciale aandacht gericht op de anode van de SOFC, in het bijzonder op de chemie van de elektrodereactie en de verdere ontwikkeling van nieuwe anodes. De oxidatiereactie van waterstof aan 'state-of-the-art' nikkel/yttrium-gestabiliseerd zirkoonoxide (cermet) anode werd bestudeerd. Alternatieve anode materialen, specifiek perovskiet en fluoriet-type materialen, werden getest in een waterstof/waterdamp gasstroom. Hoofddoelstelling was het verkrijgen van meer inzicht in de eigenschappen van verschillende anodesystemen, om daarmee verdere verbeteringen mogelijk te maken.

De elektroden werden elektrochemisch gekarakteriseerd door middel van polarisatiemetingen ($I-\eta$) en impedantiespectroscopie als functie van T , p_{H_2} en $p_{\text{H}_2\text{O}}$. In enkele gevallen werd de elektrodeïmpedantie ook gemeten als functie van de polarisatiespanning. De microstructuur van de elektroden werd onderzocht met behulp van raster-elektronenmicroscopie (SEM).

In **Hoofdstuk 1** wordt een algemene inleiding over de SOFC gegeven. De werkingprincipes en gebruikte materialen worden beschreven. Verder wordt een overzicht gegeven van alternatieve elektrodematerialen die momenteel onderzocht worden.

Hoofdstuk 2 beschrijft een modelstudie waarin een poreuze, vlakke nikkelelektrode wordt vergeleken met een gemodificeerde vlakke nikkelelektrode. De modificatie bestaat uit het aanbrengen van zeer kleine yttria-gestabiliseerd zirkoonoxide (YSZ) deeltjes op het nikkeloppervlak. De opmerkelijke overeenkomst in de eigenschappen van beide elektrodes suggereert dat essentiële stappen in het elektrodeproces aan beide elektrodes identiek zijn. De totale geleiding van de elektrodes neemt toe met de lengte van de drie-fasen grens (Triple Phase Boundary, TPB). Voor eenzelfde lengte

van de TPB wordt echter, in vergelijking met de onbehandelde nikkelelektrode, een 50% hogere geleiding gevonden voor de gemodificeerde poreuze nikkelelektrode. Dit resultaat geeft aan dat de aanwezigheid van kleine YSZ deeltjes op het oppervlak van de nikkelelektrode extra actieve plaatsen creëert waaraan de elektrodereactie kan plaats vinden.

In **Hoofdstuk 3** wordt de kinetiek van de waterstof oxidatiereactie aan de Ni/YSZ anode bestudeerd met gebruikmaking van een in 1970 door Epelboin gepresenteerde methode waarmee een uitdrukking voor de elektrodeïmpedantie kan worden afgeleid. Gebaseerd op de resultaten, is het redelijk om aan te nemen dat ladingsoverdracht processen de waterstof oxidatiereactie aan de Ni/YSZ anode domineren. De karakteristieke inductieve boog bij lage frequenties in de experimentele impedantiespectra kan worden gereproduceerd door aan te nemen dat twee, opeenvolgende reactiestappen de oppervlaktebezetting van intermediaire OH⁻ groepen beheersen. Meer geavanceerde reactieschema's zijn echter nodig om de experimentele impedantiespectra volledig te kunnen verklaren.

In **Hoofdstukken 4** en **5** worden experimenten beschreven aan alternatieve elektrodematerialen voor toepassing als poreuze anodes in SOFC. In het bijzonder zijn twee types lanthaan-gebaseerde chromieten-titanaten bestudeerd. Anodes van deze materialen zijn stabiel onder reducerende omstandigheden. De metingen zijn goed reproduceerbaar voor verschillende elektrodes met dezelfde samenstelling. De calcium- of strontium-gesubstitueerde chroomrijke materialen, met samenstelling $\text{La}_{0.7}\text{A}_{0.3}\text{Cr}_{0.8}\text{Ti}_{0.2}\text{O}_{3-\delta}$ (A = Ca, Sr), vertoonden p-type geleiding. De titaanrijke samenstelling, $\text{La}_{0.7}\text{Ca}_{0.3}\text{Cr}_{0.2}\text{Ti}_{0.8}\text{O}_{3-\delta}$, vertoonde n-type geleiding. Beide typen materialen bleken actieve elektrodes bij 850°C in een H₂/H₂O gas mengsel. De elektronische geleiding wordt een belangrijke limiterende factor wanneer de dikte van de elektrode wordt gereduceerd van 100 µm naar 20 µm. De weerstand van de 'hoge frequentie afsnede' vertoonde een duidelijke $p\text{O}_2$ -afhankelijkheid die overeenkwam met die van de elektronische geleiding. Dit effect kon worden toegeschreven aan een limiterende 'sheet resistance' van de dunne elektroden. De totale elektrodeweerstand

van deze elektroden was ongeveer een factor 10 groter dan die van de ‘state-of-the-art’ Ni/YSZ cermet anode.

De waterstof oxidatie werd ook bestudeerd aan ‘screen-printed’ cermet anodes, bestaande uit nikkelmetaal en yttrium-gestabiliseerd zirkoonoxide met 5 of 10 mol% titaniumoxide (TiO₂). De impedantiespectra bij open celspanning laten drie verschillende elektrochemische processen zien bij de toegepaste H₂/H₂O verhoudingen en temperaturen. De metingen toonden identiek gedrag als functie van p_{H_2} en p_{H_2O} voor de cermets met respectievelijk 5 en 10 mol% titania. De totale elektrodeweerstand neemt toe wanneer de sintertemperatuur van de cermets wordt verhoogd van 1300°C naar 1400°C. In tegenstelling tot eerdere waarnemingen aan standaard Ni/YSZ cermets laten de resultaten van de Ti-gedoteerde cermets een toename van de elektrodegeleiding met de tijd zien. Een opmerkelijk resultaat van het onderzoek is dat de Ti-bevattende cermets, die zeker nog niet geoptimaliseerd zijn, een zeer goede prestatie leveren bij 850°C.

Appendix A geeft een samenvatting van de mogelijkheden om met percolatietheorie de transporteigenschappen van ongeordende composieten te beschrijven en te interpreteren. De eigenschappen van percolatie spelen een sleutelrol in cermetelektroden voor SOFC toepassingen. In deze elektroden moeten de keramische en de metallische fasen én de poriestructuur een volledig percolatief systeem vormen.

In **Appendix B** wordt een model beschreven voor de elektroforetische depositie van een ideaal geroerde suspensie onder invloed van een constante cel spanning over de depositiecel. De laagvorming (‘cast growth’) wordt beschreven vanuit ‘first principles’. De invloed van het laagvormingsproces op de groeisnelheid is hierbij eveneens in rekening gebracht. Elektroforetische depositie is een interessante techniek voor het aanbrengen van geavanceerde keramische materialen voor SOFC toepassingen.

Slotopmerkingen:

De nieuwe gemengd-geleidende anode materialen, die in het kader van dit proefschrift bestudeerd zijn, maar geenszins geoptimaliseerd zijn, vertonen een goede stabiliteit en

reproduceerbaar gedrag. Ze vertonen een duidelijke elektrodeactiviteit in H_2/H_2O gasmengsels bij $850^\circ C$. De elektronische geleiding van deze perovskiet materialen is echter te laag, hetgeen resulteert in een elektrodegeleiding die een factor 10 lager is dan die van de 'state-of-the-art' Ni/YSZ cermets. De Ti-gedoteerde YSZ/Ni composieten vertonen een zeer goed anodegedrag in H_2/H_2O gasmengsels, vergelijkbaar met die van de 'state-of-the-art' Ni/YSZ cermets, en bovendien neemt de prestatie toe met de tijd. Er zijn sterke aanwijzingen dat de keramische fase een actieve rol speelt in de elektrode-reactie. Geconcludeerd kan worden dat composieten, in vergelijking met éénfasige materialen, het beste alternatief zijn voor verbeterde anodes. Het is essentieel om de beste eigenschappen van verschillende materialen te combineren om daarmee een optimale prestatie voor de anode te bereiken. Een tweede conclusie dat uit dit onderzoek naar voren komt is dat het moeilijk is om het gebruik van Ni te vermijden, wanneer uitstekende elektrode-eigenschappen zijn vereist. Wanneer koolwaterstoffen direct als brandstof worden gebruikt moet het nikkel vervangen worden in verband met het ernstige probleem van koolstofdepositie. Daarom zal verder onderzoek gericht moeten zijn op composieten van gemengd-geleidende keramiek en materialen met een hoge elektronische geleidbaarheid. Noodzakelijkerwijs zal het onderzoek ook uitgebreid moeten worden met een studie van de chemie van de laagvorming, om daarmee de microstructuur van deze composietelektrodes te optimaliseren.

Muchas gracias...

... a todos los que han hecho posible este trabajo:

- prof. D.N. Reinhoudt por aceptar amablemente ser mi promotor junto con prof. J. Schoonman. Ha sido un honor para mí.
- Henny, por tantas charlas sobre ánodos, por la ayuda enorme durante estos últimos años, y por leer detenidamente y con entusiasmo mi tesis. Te estoy muy agradecida.
- Baukje, por introducirme en el mundo de las SOFCs con tanto entusiasmo y empeño.
- Maarten y Henk, por su contribución al Apéndice B de esta tesis y tantas charlas interesantes. A Henk le agradezco especialmente que me ofreciera la posibilidad de hacer el PhD en este grupo y tanto tiempo dedicado a mi formación.
- Wolfgang, tengo muy buenos recuerdos del tiempo que trabajamos juntos en el proyecto, fue verdaderamente enriquecedor para mí.
- Nieck, por el bonito modelo del Capítulo 3 y tantas horas de simulaciones a contrarreloj.
- Bernard, por haberme guiado en el intrincado mundo de las impedancias, contribuyendo valiosamente a muchos capítulos de esta tesis.
- Cis, por las conversaciones, las postales en verano, en fin por todo, José, por tu disponibilidad a cualquier hora, Attila y Herman, hubiera sido difícil sin vosotros.
- el grupo de Inorgánica de la Universidad de Twente, y **todos** sus sucesivos miembros desde el 97 hasta ahora. He aprendido mucho con vosotros.
- los del taller: Joop y compañía, por resolverme muchos pequeños y grandes problemas.
- Günter Pudmich y Caroline Pirovano, por la preparación de las muestras investigadas en los Capítulos 4 y 5.

- Frank Tietz, por estos años de estupenda colaboración e intercambio de ideas dentro del marco del TMR, y por leer minuciosamente mi tesis, mejorándola en muchos aspectos.
- Charlotte, querida amiga, gracias por recordarme una y otra vez que es 'lo realmente importante'. Visitarte durante mis años en Holanda fue siempre un regalo para mí, y una auténtica renovación.
- Alain, por estar ahí animándome siempre con mil detalles, buena música francesa, mensajes, sugerencias ... Decirte gracias es poco.
- Loui y Gigi, la familia García-Hernán y su pequeña Andrea, Peter Oude Groen y su madre, también Sherry, Sheila y Víctor, por tantos buenos ratos y tanta hospitalidad.
- Miriam Keena, por venir a visitarme varias veces desde tan lejos, Manon por aquellas conversaciones que tanto me ayudaron, prof. Saturnino Marcos, Javier Crespo por tantos mensajes de ánimo.
- Nela, hay mucho que debo agradecerte: tu apoyo en los momentos difíciles, tu fortaleza, también sonrisas y alegría, por supuesto. Wim, por enseñarme un montón de palabras en holandés, sobre todo al principio.
- la gran familia del P. Alba, por tantos cuidados en la distancia.
- Laura, por algo realmente importante: ¡enseñarme a andar en bici!, y por Saskia y Lucas, que me han alegrado muchas tardes.
- Laura y Marta, Susana Loredó: por demostrarme de mil maneras que la amistad verdadera dura para siempre. Que suerte tan enorme haberos conocido.
- mis padres, Javier y mis hermanos Conchita, Fátima y Serafín-Manuel: esta tesis con todas las dificultades, pequeñas conquistas, y alegrías que encierra, va especialmente por vosotros, con agradecimiento y con amor, el que me habéis sabido dar siempre.

Mercedes

Agosto 2002

Curriculum Vitae

Mercedes González Cuenca was born on February 24, 1972 in Santander, Spain. She finished her primary education at El Pinar School in Barcelona. Secondary education was at Torreanaz School in Cantabria. From 1990 to 1996 she studied Physics at the Faculty of Sciences, at Cantabria University. In 1996 she spent 6 months in Grenoble, France, as holder of a Materials Science Erasmus Grant at the Institute Laue-Langevin where she dealt with new detectors for Laue diffraction with neutrons. In 1997 she started her working experience in The Netherlands as research fellow at Twente University, within the Inorganic Materials Science group working on hydrogen oxidation at porous nickel electrodes for solid oxide fuel cells.

On January 1998 she started her PhD on novel anode materials for solid oxide fuel cells in the same group under the supervision of dr. B.A. Boukamp, dr. H.J.M. Bouwmeester and prof. dr. ir. H. Verweij. The results of this research are described in this thesis and have been published in several scientific journals.